DESIGN AND CHARACTERIZATION OF AN ALTITUDE CHAMBER FOR CHEMICAL ROCKET ENGINES

by

Jacob M. McCormick

A Thesis

Submitted to the Faculty of Purdue University

In Partial Fulfillment of the Requirements for the degree of

Master of Science in Aeronautics and Astronautics

School of Aeronautics & Astronautics

West Lafayette, Indiana

August 2019

THE PURDUE UNIVERSITY GRADUATE SCHOOL
STATEMENT OF COMMITTEE APPROVAL

Dr. Timothée Pourpoint, Chair
Department of Aeronautics and Astronautics
Dr. Stephen Heister
Department of Aeronautics and Astronautics
Dr. William Anderson
Department of Aeronautics and Astronautics

Approved by:

Dr. Wayne Chen
Head of the Graduate Program

Dedicated to my friends and loved ones. You've stood by me, even in the hardest of times. It is now my turn to do the same for you.

ACKNOWLEDGMENTS

I owe my success in graduate school to a great multitude of people. Dr. Pourpoint has played an essential role in my development as an aerospace engineer. He is the ideal representation of a mentor and advisor, and he has laid the foundation for my success both in academia and industry. I want to thank Scott Meyer for the constructive criticism provided for various project designs implemented over the last two years. I'd also like to thank Rob and Toby for providing input regarding various designs. Through your design suggestions and critiques, the path from theoretical model to physical component has become slightly smoother.

I also want to thank Ben Whitehead for acting as a sounding board for different thesis ideas and always being willing to answer, "even the silly questions." While not necessarily directly influential on my thesis, each member of Dr. Pourpoint's lab has made a lasting impact. Thank you everyone for making the last two years memorable in the form of different projects: developing the altitude chamber, preparing the atmospheric JPL tests, creating the MON synthesis stand, etc. Each of these experiences has helped to shape me into the aerospace engineer that I am today.

TABLE OF CONTENTS

LIST OF TABLES

LIST OF FIGURES

NOMENCLATURE

A	-	Area (m^2)
A_t	-	Bolt cross sectional area (m^2)
C_d	-	Discharge coefficient
C_p	-	Specific heat (J/kg-K)
D	-	Diameter (m)
ER	-	Expansion ratio
γ	-	Heat capacity ratio
$\dot{m}$	-	Mass flow rate (kg/s)
M	-	Mach number
MW	-	Molecular weight (kg/mol)
N	-	Number of items
η_m	-	Momentum coefficient
η_p	-	Motive nozzle efficiency
η_s	-	Suction efficiency
Nu_D	-	Nusselt number
O/F	-	Mixture Ratio
P	-	Pressure (Pa)
ϕ_p	-	Motive plume efficiency
ϕ_m	-	Mixing efficiency
Pr	-	Prandtl number
R	-	Specific Gas Constant (J/kg-K)
Re	-	Reynold's number
R_u	-	Universal gas constant (J/mol-K)
ρ	-	Density (kg/m^3)
σ	-	Stress (Pa)
T	-	Temperature (K)
V	-	Velocity (m/s)
$\sim_t$	-	Motive nozzle throat value

$\sim_0$ - Stagnation Value

$\sim_{mix}$ - Mixed flow value

$\sim_{N_2}$ - Equivalent nitrogen value

$\sim_{opt}$ - Optimum value

$\sim_p$ - General motive value

$\sim_{p0}$ - Motive Stagnation Value

$\sim_{p1}$ - Motive nozzle exit value

$\sim_{p2}$ - Motive pre-contraction value

$\sim_{p3}$ - Motive value after normal shock

$\sim_{py}$ - Motive value at hypothetical throat

$\sim_s$ - General suction value

$\sim_{s0}$ - Suction Stagnation Value

$\sim_{s2}$ - Suction pre-contraction value

$\sim_{sy}$ - Suction value at hypothetical throat

$\sim_3$ - Value after normal shock in constant area section

ABSTRACT

Author: McCormick, Jacob, M. MS
Institution: Purdue University
Degree Received: August 2019
Title: Design and Characterization of an Altitude Chamber for Chemical Rocket Engines.
Committee Chair: Dr. Timothée Pourpoint

Over the course of a launch, a rocket experiences a broad range of atmospheric pressures, influencing the performance of the rocket nozzle. Aside from implementing a complex system to modulate the geometry of the rocket nozzle, it is nearly impossible to optimize the overall performance of the rocket engine for the entirety of the burn. It is therefore necessary for engineers to optimize the performance for a specific atmospheric pressure range. For this reason, facilities exist which are capable of testing propulsion systems at relevant operational conditions. This is accomplished by simulating the atmospheric pressure relevant to the altitude of interest in a closed volume, also known as an altitude chamber.

This thesis focuses on the development of reduced pressure testing capabilities at Zucrow Laboratories. A two-stage ejector on loan from NASA Marshall is used in series with a supersonic diffuser to allow for the testing of up to100 lb_f rocket engines at equivalent altitudes of up to 100,000 ft. The objective of this research is to implement a one-dimensional (1-D) model which accurately predicts the performance of the two-stage ejector in real time, informing the maximum thrust and simulated altitude capabilities within the altitude chamber located in room 134A of ZL3 during experimental testing.

A new 1-D model was created which efficiently balances computational performance with prediction accuracy. The new model was validated using experimental data collected for a smaller single-stage ejector utilizing facility nitrogen as the suction fluid and facility air as the motive fluid. The validated model was then shown to accurately predict the performance of the single-stage ejector system during the testing of a small solid rocket motor (SRM) within the altitude chamber. The new 1-D model was then calibrated using experimental data from the two-stage ejector on loan from NASA Marshall. It was shown that the new model is capable of predicting the performance of the two-stage ejector for varying rocket engine configurations. As

a result, this new model was proven to be a viable predictive tool to inform the testing capabilities of the altitude facility at Zucrow Labs.

In addition, a new rocket engine is designed for the characterization of a hybrid grain configuration within the altitude chamber at reduced pressure, which serves as a continuation of the atmospheric testing campaign performed in collaboration with the Jet Propulsion Laboratory (JPL).

1 INTRODUCTION

Prior to a space launch, it is often necessary to characterize the performance of the vehicle's engines at relevant atmospheric pressure conditions. For example, the performance of a high expansion ratio rocket nozzle designed to operate in the vacuum of space cannot be validated at sea level conditions. It is therefore necessary to simulate the ambient pressure conditions relevant to the altitude of interest for the mission. This is commonly accomplished using a closed vessel (often called an altitude chamber), in addition to a device capable of maintaining the reduced pressure environment within the chamber. There are a few different methods to achieve this steady reduced pressure, including vacuum pumps, ejectors, and supersonic diffusers. While each of these three devices is discussed below, only the ejector system will be discussed in sections to follow.

As the leak rate associated with pumps is dictated primarily by how well the dynamic seals can prevent entrained gases from escaping, these devices are capable of reaching extremely low pressures. This makes pumps ideal for testing rocket engines in extremely low pressure environments. However, pumps are constant volumetric flow devices, removing a set volume of gases per revolution. For this reason, testing higher thrust motors requires a proportionate or even exponential increase in the scale of the pump employed. This is because all of the internal components of the pump must scale to meet the increased demand on the overall system. For this reason, testing rocket engines with high thrust levels is often difficult using a pump alone.

Supersonic diffusers avoid this limitation by converting the kinetic energy of exhausted gases back into pressure. The recovery of pressure within a supersonic diffuser is accomplished through a complex system of shocks that occur within the second throat. Supersonic diffusers are capable of a maximum theoretical compression ratio, which limits the minimum pressure that can be maintained within the altitude chamber, assuming that the supersonic diffuser is exhausting to ambient pressure (14.7 psia). While it has been shown in the literature that supersonic diffusers are capable of performing reduced pressure testing unassisted [1], achieving extremely low pressures within the altitude chamber requires the use of subsequent vacuum systems to reduce the back pressure immediately downstream of the supersonic diffuser exit.

Ejectors and supersonic diffusers are commonly used concurrently to achieve reduced pressure conditions relevant to the testing of high-expansion ratio rocket engines for space

applications. The ejector system acts to reduce the back pressure experienced by the supersonic diffuser, allowing for the combined system to maintain a pressure much lower than the supersonic diffuser alone. Similar to supersonic diffusers, ejectors convert the kinetic energy of a motive fluid (air in our case) into pressure using a complex system of shocks within the constant area section of the ejector. Both ejectors and supersonic diffusers are capable of handling exhaust flow rates much higher than a pump of comparable scale.

In the same way that a single-stage ejector coupled with a supersonic diffuser increases the overall compression ratio of the system, multiple ejectors can be placed in series to achieve a comparable increase in pressure recovery capabilities. Employing a multi-stage ejector configuration has been shown to yield a significant improvement in overall system performance and efficiency when compared with a single-stage ejector of similar size [2]. The altitude facility in ZL3 at Zucrow Laboratories employs a two-stage ejector coupled with a supersonic diffuser to maintain a simulated altitude of up to 100,000 ft during the testing of rocket engines up to 100 lb_f.

As each engine characterized using the altitude facility applies different loads to the vacuum system, it is beneficial to predict the motive flow conditions necessary to support a given testing campaign. This expedites the process of testing while simultaneously conserving facility air. This a-priori determination of necessary testing conditions is accomplished through modeling. While there are multiple modeling schemes which can be implemented to accomplish this performance prediction, one-dimensional models are by far the most computationally efficient. This modeling class can predict the performance of the vacuum system in real time, making it a viable tool to be used in an experimental testing environment. A comprehensive literature review was performed to determine the viability of existing models, and it was determined that a new 1-D model was necessary to meet the needs of the altitude facility at ZL3. In this thesis, a new quasi one-dimensional model was developed to accurately predict the performance of the two-stage ejector system over the full operational range of pressures and thrust values achievable by the new altitude facility in ZL3 at Zucrow Laboratories. This thesis also summarizes the design of a new hybrid rocket engine, which will rely on the predictive capabilities of the new model to determine the maximum achievable simulated altitude for experimental testing within the altitude chamber.

2 EJECTOR BACKGROUND

Ejectors have been employed since 1901 [3], with applications ranging from refrigeration systems and powder transportation to jet thrust augmentation and the characterization of rocket motors for space operation [4]. This wide-spread application of ejectors is largely due to the robust nature of ejector operation. Ejectors are simple in design and have no moving parts, thus minimizing operational cost and maintenance frequency [5]. A simple schematic of a single-stage ejector is provided below in Figure 1, for reference.

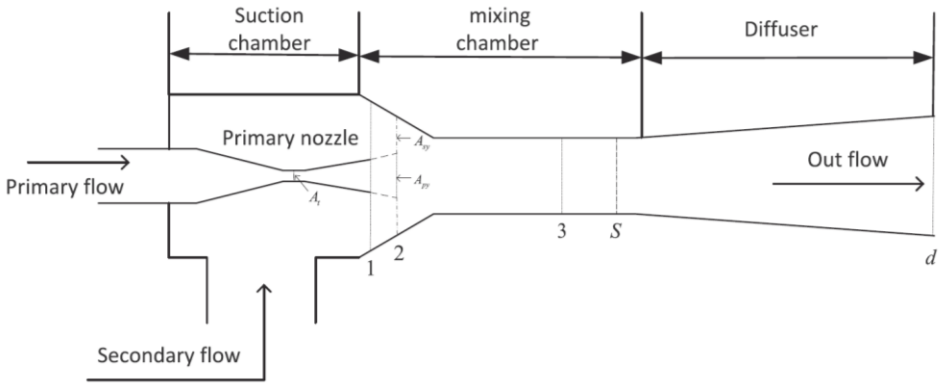

Figure 1: Representation of major components of a single-stage ejector [6].

There are four primary components present in most ejector systems; these are the motive nozzle, the mixing chamber, the constant-area section, and the diffuser. There is a class of ejectors which does not include the mixing chamber in the ejector geometry. This ejector class will be discussed later in the thesis, and it is called a constant-area ejector.

An ejector is a device which converts the pressure energy of a working fluid, typically called the motive fluid, into velocity [7]. This is typically accomplished using a converging-diverging nozzle. The high stagnation pressure motive fluid passes through the converging diverging (CD) motive nozzle. At the throat of the CD nozzle, the motive gas is traveling at the speed of sound, i.e. has a Mach number of one. Equation (1) can be used to calculate the mass flow of a compressible gas through a converging diverging nozzle.

$$\dot{m}_p = \frac{P_{p,0} A_t}{\sqrt{T_{p,0}}} \sqrt{\frac{\gamma_p}{R_p} \left(\frac{2}{\gamma_p + 1} \right)^{(\gamma_p + 1)/(\gamma_p - 1)}} \quad (1)$$

The motive flow then expands isentropically to a Mach number above one in the diverging section of the motive nozzle. Equation (2) can be used to determine the isentropic relationship between the Mach number and the static pressure of a flow.

$$\frac{P}{P_0} = \left(1 + \frac{\gamma - 1}{2} M^2 \right)^{\frac{-\gamma}{\gamma - 1}} \quad (2)$$

As the motive gas exits the converging-diverging nozzle, it continues to accelerate isentropically in the mixing chamber until a pressure is reached which is at, or below, the static pressure of the suction fluid. The suction fluid is the gas that is to be evacuated from the altitude chamber in the case of motor performance characterization at reduced pressures. For the majority of operating cases, the Mach number of the suction flow at the ejector inlet is sufficiently low to assume stagnation conditions. This produces a favorable pressure gradient between the motive and suction fluids, causing the suction fluid to be entrained into the mixing chamber [8]. It is a combination of this pressure gradient, and momentum transfer from the motive flow to the suction flow through shear, which induces mixing between the supersonic motive flow and subsonic suction flow within the mixing chamber.

The two fluids continue mixing through the converging section between the mixing chamber and the constant-area section of the ejector. Momentum is transferred from the motive flow to the suction flow, resulting in a supersonic mixed flow. The constant-area section length is chosen to ensure that the two fluids are properly mixed well before the entrance to the diffuser section of the ejector [9]. At some point within the constant-area section of the ejector, a normal shock occurs which irreversibly converts the kinetic energy of the mixed flow into pressure. The static pressure of the subsonic mixed flow following the normal shock can be determined using gas dynamic relations. The subsonic mixed flow then expands in the diffuser section of the ejector, reaching approximately stagnation conditions. This is the final stage of pressure

recovery within the ejector, and the subsonic mixed flow is then either exhausted to the atmosphere or fed into the next ejector stage in the system.

In order to ensure optimal ejector operation, the ejector must recover the static pressure of the suction fluid to the ambient pressure conditions present at the exit plane of the ejector-diffuser. The ambient pressure at the exit plane of the diffuser section is known as back pressure. If the static pressure of the mixed flow at the exit plane of the diffuser is less than the back pressure, there exists an adverse pressure gradient back into the diffuser [10]. This adverse pressure gradient acts to move the shock wave present in the constant-area section of the ejector further upstream. As the normal shock moves further upstream, the effective mixing length for the motive and suction flow is reduced. This decrease in mixing length reduces mixing efficiency, negatively impacting overall ejector performance. Once the back pressure rises to a critical level, the shock structure moves out of the constant-area section and into the mixing chamber of the ejector [11]. At this back pressure level, the effective compression ratio of the ejector is drastically reduced [12]. This results in a steep rise in altitude chamber pressure, given constant motive/suction flow conditions. The back pressure at which ejector performance begins to deteriorate is called the critical back pressure. A graph showing the relationship between ejector performance and back pressure is given in Figure 2 below.

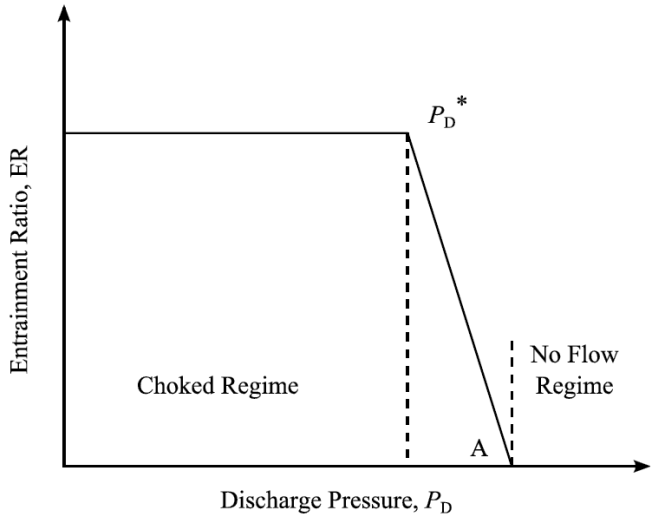

Figure 2: Relationship between ejector performance and back pressure (discharge pressure) [8].

For a single-stage ejector exhausting to the atmosphere, the back pressure is held constant at 14.7 psia. However, for a multiple-stage ejector, the back pressure that an ejector stage experiences can vary. For a multiple-stage ejector system configured in series, the exit of the upstream ejector is connected to the suction inlet of the downstream ejector. An example of this configuration is given in Figure 3 for reference, which shows a typical static pressure and mass flow rate distribution for two ejectors connected in a series configuration.

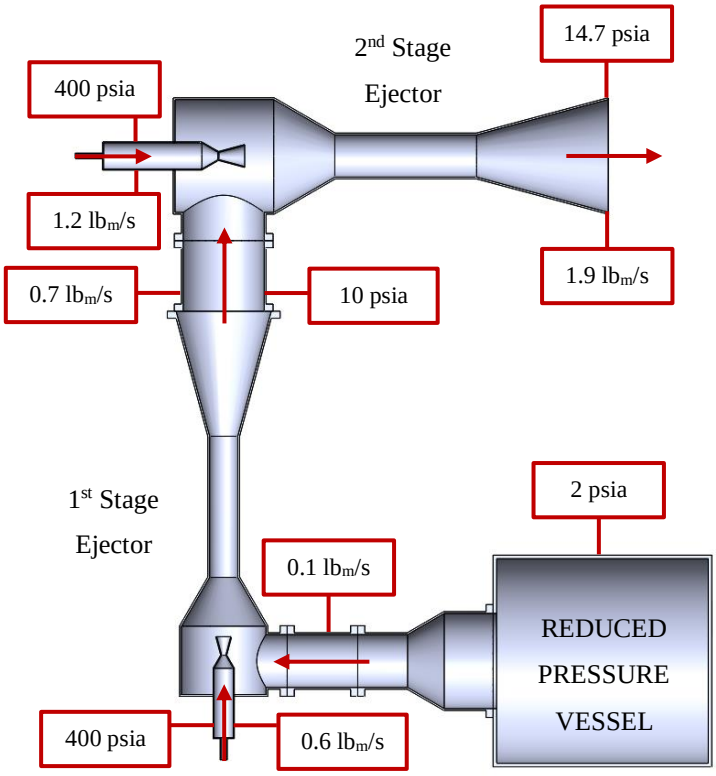

Figure 3: Two-stage ejector system configured in series with example static pressure and mass flow rate distribution.

Figure 3 shows that the back pressure experienced by the first stage ejector is dependent on the compression ratio of the second stage. For this discussion, it is important to understand that the back pressure for the second-stage ejector is a constant value of 14.7 psia. If the compression ratio of the second stage ejector is compromised, the suction inlet pressure of the second-stage ejector (back pressure of the first-stage ejector) increases accordingly. As the

compression ratio across the first-stage ejector remains constant, the static pressure within the altitude chamber must increase.

In the same way, if the compression ratio of the first-stage ejector is compromised, the exit pressure of the first-stage (suction inlet of the second-stage) decreases. As the second-stage compression ratio remains constant, the exit pressure of the second-stage ejector also decreases. The back pressure for the second-stage ejector has not changed (still 14.7 psia), and thus there exists an adverse pressure gradient back into the second-stage ejector-diffuser. The normal shock in the constant-area section of the second-stage ejector then moves upstream into the mixing chamber. This breaks the performance of the second-stage ejector, as discussed earlier, further decreasing the overall compression ratio of the two-stage ejector system. Ultimately, this interaction again leads to a sharp rise in altitude chamber static pressure. In this way, it can be seen that the performance of each ejector in a two-stage ejector system configured in series is highly dependent on the other.

Another characteristic of a series configuration ejector system is that, for a constant geometry and motive conditions, the downstream ejector has a lower compression ratio capability than that of the upstream ejector. Figure 3 shows that the mixed flow exiting the first-stage ejector is handled as the suction flow of the second-stage ejector. The downstream ejector stage must be designed to handle both the original suction flow being evacuated from the altitude chamber and the motive flow of the upstream ejector stage. This results in a lower compression ratio capability, as the compression efficiency of ejectors decreases with increased suction load. It is common to use a slightly larger downstream ejector stage to handle the increased suction load [13]. This example illustrates the general behavior of a multiple-stage ejector configured in series. Multiple-stage ejector systems can also be configured in parallel with one another. An example of this configuration is given in Figure 4, which shows a typical pressure and mass flow rate distribution for a two-stage ejector configured in parallel.

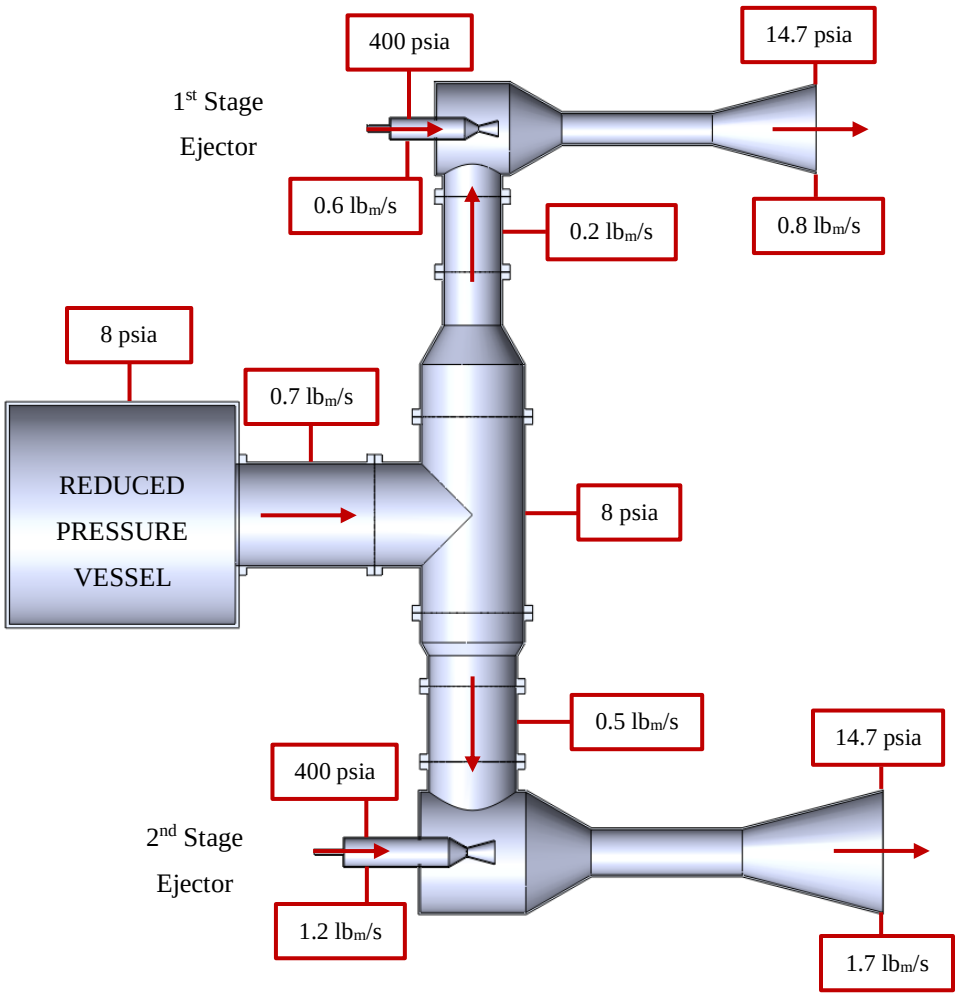

Figure 4: Two-stage ejector system configured in parallel with example static pressure and mass flow rate distribution.

The same two ejectors are used in this example as in the series configuration to isolate only the effect of changing the configuration of the ejector system. In Figure 4, the static pressure within the altitude chamber is much higher than for the series configuration. However, the suction mass flow rate is much higher for the parallel configuration when compared with the series configuration.

There are a few conclusions that can be made based on these results. Multiple-stage ejector systems configured in series are typically capable of higher overall compression ratios. However, the series configuration is generally more sensitive to changes in operating conditions for all stages of the ejector system. Multiple-stage ejector systems configured in parallel benefit from a higher relative suction mass flow rate capability, but do not have the benefit of a multiple-stage combined compression ratio. For this reason, multiple-stage ejectors configured in series

are generally more practical when high vacuum levels are desired. A multiple-stage ejector system configured in parallel is more appropriate when the system must handle relatively large suction mass flow rates. For example, a multiple-stage ejector system configured in series would be appropriate for the testing of a low thrust rocket motor at high vacuum levels, while a multiple-stage ejector system configured in parallel would be more appropriate for the testing of a high thrust rocket motor at pressures closer to sea level conditions (14.7 psia).

While there are significant performance benefits to be had employing ejector systems, they do suffer from relatively low energy efficiencies when compared to alternative compression devices [5]. This is due to the normal and oblique shocks occurring at the exit of the ejector nozzle and within the constant area section of the ejector, as well as high frictional and shear losses. The inherent inefficiency associated with ejectors is compensated by the fact that ejectors rely on a high stagnation pressure motive gas as their energy source. As many facilities in industry produce steam as a result of relevant production processes [14], it is common for ejectors supporting these processes to utilize steam as their motive source. Zucrow Laboratories has a large volume of high pressure air that is used to support a multitude of experimental tests, and thus it is more practical to use high pressure air as the motive source for the two-stage ejector system in the altitude facility.

While ejectors can vary in scale from millimeters to feet, they can generally be divided into two main groups based on their geometry. There are two main types of ejectors – constant-area ejectors and constant-pressure ejectors - each of which induce mixing between the motive and suction fluids in different ways. A constant area ejector is the simpler of the two ejector geometries and can be seen in Figure 5 below.

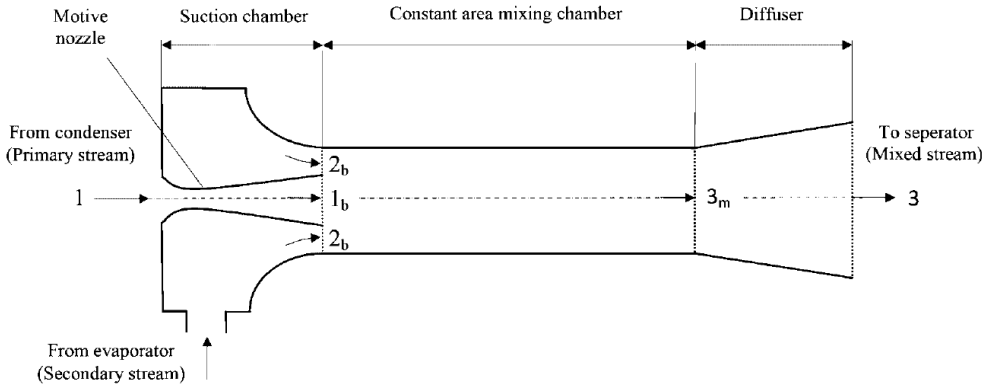

Figure 5: Geometry of a constant-area ejector [15].

The motive nozzle of a constant-area ejector is slightly extended, with the motive gas leaving the exit plane of the converging diverging nozzle in the constant area section of the ejector. In this way, the "mixing chamber" only serves to hold the stagnant suction gas before it is entrained by the motive fluid in the constant area section of the ejector. The mixing of the motive and suction fluids occurs only in the constant-area section of a constant-area ejector. The mixing process associated with a constant-area ejector is greatly simplified, as there is no change in area over the mixing length; this can again be seen in Figure 5. This geometric simplification can make the process of modeling significantly easier, as there is no area change to account for. However, it has been shown in literature that a constant-area ejector is less efficient than a constant-pressure ejector of comparable size [16]. The main difference between a constant-area and constant-pressure ejector is the location of the motive nozzle exit plane. The motive nozzle exit plane is located near the middle of the mixing chamber for a constant-pressure ejector. The altitude facility at Zucrow Laboratories uses a two-stage constant-pressure ejector system. For this reason, the remainder of this thesis will focus only on modeling the performance of a constant-pressure ejector.

Constant-pressure ejectors allow for constant-pressure mixing between the motive and suction flows. The overall geometry of a constant-pressure ejector can be seen in Figure 1. As stated earlier, the exit plane of the motive nozzle is located approximately in the middle of the mixing chamber for a constant-pressure ejector. While there have been multiple experimental and theoretical studies which have focused on determining the optimum location for the exit plane of the motive nozzle in a constant-pressure ejector, this is an adequate generalization for the discussion. Entrainment begins close to the exit of the CD nozzle, with the two flows interacting through the contraction region of the mixing chamber and into the constant-area section of the ejector. The mixing processes occurring in the constant-area section and diffuser are unchanged between the two types of ejectors. These two types only influence the mixing of the two fluids leading into the constant-area section.

Ejectors can also be classified based on the motive and suction fluids that are being used in the ejector system. There are three main classes of ejectors: liquid-liquid, liquid-gas, and gas-gas ejectors [17]. Liquid-liquid ejectors depend on the incompressible interaction of the two fluid flows to perform the compression within the ejector. Liquid-gas ejectors are the most complex of the three ejector classes from a modeling perspective. This ejector class requires the

model to handle two-phase flow interactions at supersonic velocities. The gas-gas ejector class is most applicable to this thesis and requires the modeling of compressible flow interactions between the suction and motive fluids. As gas-gas ejector modeling is most applicable to the two-stage ejector system at Zucrow Laboratories, this thesis will focus on this ejector class and exclude the other two classes.

An ejector is designed from the factory to operate most efficiently at a single point on its operating curve [18]. The majority of the initial experimental validation for this model was performed using a small-single stage ejector, which was optimized from the factory to perform most efficiently at a motive pressure of 215 psia. Decreasing the motive pressure below 215 psia decreases the performance of the ejector. This makes sense intuitively, as one would expect that decreasing the energy throughput of the device would decrease the performance of the ejector system. It was found during the experimental characterization of the single-stage ejector that increasing the motive pressure beyond 215 psia also decreases the performance of the ejector. This may be a surprising result, as the theoretical energy available to the ejector system increases with higher motive pressures. However, this is an accepted result in industrial ejector design, and the CFD results in literature help to explain this phenomenon. The theoretical results of a paper written in 2009 by Kumaran et al. are given in Figure 6 below.

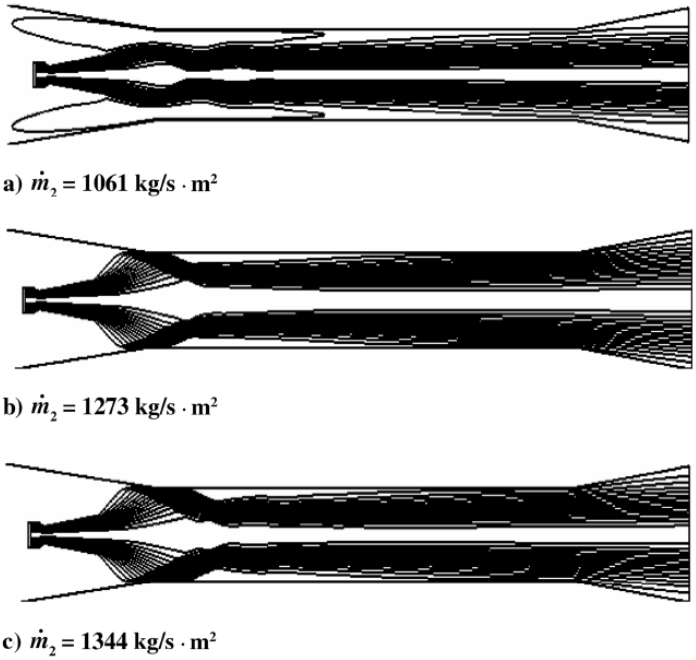

Figure 6: Motive plume flow lines for different motive nozzle exit pressures [10].

These theoretical results from CFD modeling can help us better understand the interaction mechanisms occurring within the ejector during nominal and off-design operation. The discussion below is informed by the results of Kumaran et al. [10]. As can be seen from the equation for mass flow across a converging-diverging nozzle, as well as the isentropic relation between stagnation and static pressure, the static pressure at the exit plane of the converging-diverging nozzle increases with increasing upstream stagnation pressure. It can also be seen from the equation for mass flow across a converging-diverging nozzle that increasing mass flow requires a proportionate increase in upstream stagnation pressure. Section b) of Figure 6 shows the operation of the ejector at its optimized motive stagnation pressure value. In this section, the motive plume expands just to the wall of the constant-area section of the ejector. The momentum losses within the ejector are minimized, and there is no reversed flow of gases back into the mixing chamber of the ejector.

The mass flow specified in section a) of Figure 6 requires a lower motive stagnation pressure than section b), and thus yields a lower static pressure at the exit plane of the motive nozzle. Because the static pressure at the exit plane of the nozzle is lower for section a) than for section b), the motive plume doesn't fully expand to fill the constant-area section of the ejector. It can be seen in section a) of Figure 6 that there are recirculation regions between the motive plume and the wall of the ejector. These recirculation regions further reduce the momentum of the motive jet plume and allow for leak paths from the atmosphere back into the mixing chamber of the ejector. These factors ultimately result in an altitude chamber static pressure that is higher than optimal.

The mass flow in section c) of Figure 6 requires a higher stagnation pressure than section b), resulting in a higher motive static pressure at the exit plane of the motive nozzle. The motive gas at the exit plane of the nozzle is under-expanded for section c) when compare to that of section b), and thus results in greater expansion of the motive plume downstream. The motive plume then impacts the converging section of the ejector, dissipating large amounts of momentum and energy [10]. This loss of momentum and energy reduces the efficiency of the ejector at the operation conditions given in section c), again decreasing the performance of the ejector. In this discussion, it can be seen that there are multiple factors which lead to sub-optimal performance for off-design motive stagnation pressures within an ejector.

It is important to understand the fundamental interactions that determine the performance of an ejector. By understanding each of the driving interactions within an ejector, it is possible for the designer to create a model which more accurately predicts the overall performance of the ejector system. Failing to understand these interactions can lead to incorrect assumptions which do not accurately capture ejector system performance. Often, within a model, it is more beneficial not to make assumptions until the physical behavior of the system is fully understood. Having provided a brief description of the operation of a single and multiple-stage ejector system, it is now appropriate to discuss the various models that have been presented in literature over the years.

3 EJECTOR MODELING BACKGROUND

The interaction between the two fluids within the mixing chamber of the ejector is perhaps the least understood aspect of ejector operation. This interaction region within the ejector is a driving motivator for the wide array of models that exist in the literature. There are a few different theoretical methods which can be used to predict the performance of an ejector system; each of these methods varies in computational time, complexity, and accuracy.

Computational Fluid Dynamics (CFD) is by far the most accurate method for modeling ejector performance. However, CFD is computationally expensive and sensitive to input conditions. It is often necessary to perform an initial validation for a given mesh before extending that simulation structure to unsolved problems. CFD is generally more appropriate when a deep understanding of the flow interactions is necessary, and it has become a popular modeling approach within academia as the computational power of computers has increased. CFD can also be used to inform more simplistic one dimensional models, allowing the developer to understand the overarching flow processes that are otherwise difficult to determine experimentally.

The next class of methods are one-dimensional (1-D) models. One-dimensional models often adopt a control volume approach, where relevant flow values are calculated at discrete points within the ejector. An example of a control volume calculation methodology is given in Figure 7.

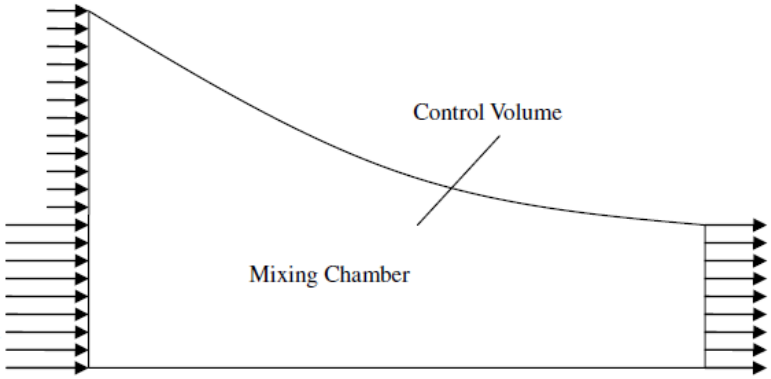

Figure 7: Control volume approach with consideration for area change and mixing [19].

There are three main classes of 1-D modeling methods: empirical, semi-empirical (hybrid), and purely theoretical methods. Empirical models are the simplest type of model, with no underlying equations being developed to define the performance of the ejector system. Instead, this model type is fully informed by experiment, with regression analysis being performed to develop fits for the experimental data. While empirical models are useful for quickly interpolating between data points over the ejector's operating range, this model class cannot be used to make predictions for different ejector geometries or even fluid types [20]. For this reason, empirical models are only useful for characterizing the performance of an ejector system with non-variable geometry and flow conditions. Empirical models are useful in traditional industrial processes, where an ejector system may have essentially constant operating conditions, with only small changes in suction load or motive supply pressure.

Semi-empirical models, or hybrid models, contribute a set of flow equations which define the general processes occurring within an ejector. Many of the more complex fluid interactions – turbulent mixing, shock structures, wall friction – are absorbed into a hybrid model using corrective coefficients which are introduced throughout the model's calculation architecture. These types of models benefit from a greater potential for extension when compared with purely empirical models, but still cannot accurately define all fluid interactions that occur during nominal ejector operation. With this model class, it is possible to predict the performance of an ejector with slight variations in ejector geometry and flow conditions. These performance prediction capabilities make this model class popular in industries that handle varying fluid types and operating temperatures/pressures. This model is also not computationally expensive, with flow solutions being determined in a short amount of time relative to purely theoretical models.

The most complex one-dimensional model class is that of the purely theoretical model. Purely theoretical models do not rely on experimental data to inform the modeling process. Similar to CFD, purely theoretical models only rely on experimental data for initial validation. Once validated, purely theoretical models can be extended to a vast array of ejector geometries and operating conditions. This large prediction benefit of purely theoretical models over the two previously mentioned modeling classes is balanced by a large increase in both computational time and model complexity. In this sense, purely theoretical models are similar to CFD in implementation. Purely theoretical models are therefore inappropriate for real-time predictions

of ejector performance [21]. This model class is instead more commonly used in academia, or when the performance of an ejector cannot be determined based on prior experimental results.

Each of the three model classes stated above has certain benefits and drawbacks. It is the job of the developer to determine which of these classes best suits the modeling needs of his/her project. A short overview of the various relevant models introduced in literature is given below. For this historical summary, only semi-empirical models are discussed. It was determined that the semi-empirical modeling class achieved a good balance between computational efficiency and model accuracy.

There have been many different models introduced in the literature over a nearly century-long period of sustained research effort. Each of these models makes slightly different assumptions and introduces novel calculation methodologies for the prediction of ejector performance. The first known mathematical model for predicting the performance of ejectors was introduced in 1942 by Keenan and Neumann [22]. This model calculated the performance of a single-stage constant area-ejector using ideal gas dynamics, as well as conservation of mass, energy, and momentum. Compressible gas dynamics, as well as the fundamental conservation laws, has been used in a majority of subsequent models. In 1950, the concept of constant-pressure mixing was introduced by Keenan et al. [23], stating that the static pressures of the motive and suction flows were equal downstream of the exit plane of the motive nozzle. The motive and suction flows then mixed at equal/constant pressure through the converging section and into the constant-area section of the ejector.

While much theoretical work was being performed to better understand the function of ejectors, there were parallel experimental studies which sought to visually determine the interaction of the motive and suction fluids as they travel through the ejector. In the late 1950's and early 1960's, this visualization was commonly achieved using a method called vapor screening, where vapors are introduced into the motive flow upstream of the nozzle. These vapors then condense in the mixing section, and act as tracer particles for visualization of the flow [24]. The results of these visual studies better informed theoretical models, further improving their physical accuracy. Variants of these early visualization techniques are used today, and they continue to provide valuable insights regarding the complex processes occurring in the ejector during mixing.

The results of experimental visualization by Fabri and Siestrunck [25] helped to inform a new model which defined a fictive suction throat located upstream of the constant-area section of the ejector [12]. At some point upstream of the constant-area section of the ejector, it is assumed that the suction flow reaches sonic velocity. It is also assumed that mixing between the two flows only occurred downstream of this fictive suction throat. It is important to mention this assumption present in this model, as many models proposed in subsequent publications make similar assumptions with slight variations.

One of the more popular models, which is cited throughout the literature recently, is the one-dimensional model proposed by Huang et al. in 1999 [26]. This model is developed to predict the performance of a constant-pressure mixing ejector, and makes the assumption of a fictive suction throat originally presented by Munday and Bagster [12]. While there are many simplifying assumptions made in this model, perhaps the most significant is the assumption that the suction throat is located at the entrance to the constant-area section of the ejector. This assumption can be seen graphically in Figure 8.

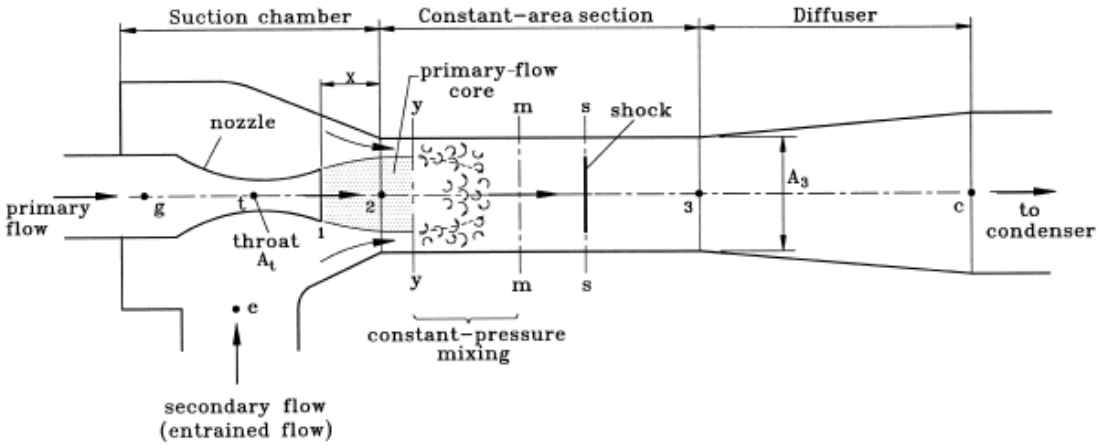

Figure 8: Graphical representation of the calculation architecture for the 1-D model proposed by Huang et al. [26].

The cross section *y-y* is denoted as the location of the suction throat; it is assumed that the two flows only mix downstream of the suction throat. This assumption simplifies the calculations necessary to simulate the mixing of the two fluids, as there is no area change that occurs during this mixing process. However, it does not accommodate mixing between the exit plane of the motive nozzle and the constant-area section of the ejector. This semi-empirical

model also relies on four corrective coefficients which must be informed using experimental results. These four corrective coefficients are introduced to account for motive nozzle, motive plume, suction acceleration, and mixing losses. When fitting more than one corrective coefficient to experimental data, it is essential that there exist orthogonal results. This means that a given experimental operating condition for an ejector cannot be satisfied by two different combinations of corrective coefficients. If there is more than one combination of corrective coefficient values which satisfies a given operating point, then any of the successful combinations can be chosen when fitting the model to the experimental data. When fitting the model to experimental data, it is necessary to have smooth curves which relate the value of the corrective coefficient to the data. Smooth corrective coefficient curve fits allow for interpolation between points on the operating curve of the ejector. As the number of corrective coefficients increases, the number of potential inter-relations between corrective coefficients also increases.

The 1-D model proposed by Huang et al. was experimentally validated using small ejectors with different nozzle geometries and constant-area section diameters. The geometrical dimensions for the ejector configurations used in the experimental validation process are given in Table 1 and Table 2.

Table 1: Geometrical dimensions of the motive nozzles used for experimental performance characterization [26].

Nozzle	**Throat Diameter (mm)**	**Exit Diameter (mm)**	**Expansion Ratio**
A	2.64	4.5	2.905
E	2.82	5.1	3.27

Table 2: Geometrical dimensions of the constant-area sections for experimental performance characterization [26].

Constant-area Section	Diameter (mm)	Inlet Converging Angle (°)
A	6.7	68
B	6.98	60
C	7.6	67
D	8.1	68
E	8.54	67
F	8.84	67
G	7.34	60
H	9.2	62

Experimental data was collected by Huang et al. for different combinations of these nozzle and constant-area section geometries. Using the experimental data collected, the author made conclusions regarding the four corrective coefficients defined within the model.

Many publications are presented in literature which either build upon the model architecture of Huang et al., or use the experimental results to validate their own model. One of the more recent one-dimensional models presented in literature is the shock circle model, published in 2007 [27]. This model introduces a velocity distribution for the two fluid flows. In prior models, a uniform velocity was assigned to each of the two fluids, with no consideration for radial variation in fluid velocity. Figure 9 shows the shock circle model velocity distribution compared to the traditional discrete velocity treatment of prior one-dimensional models.

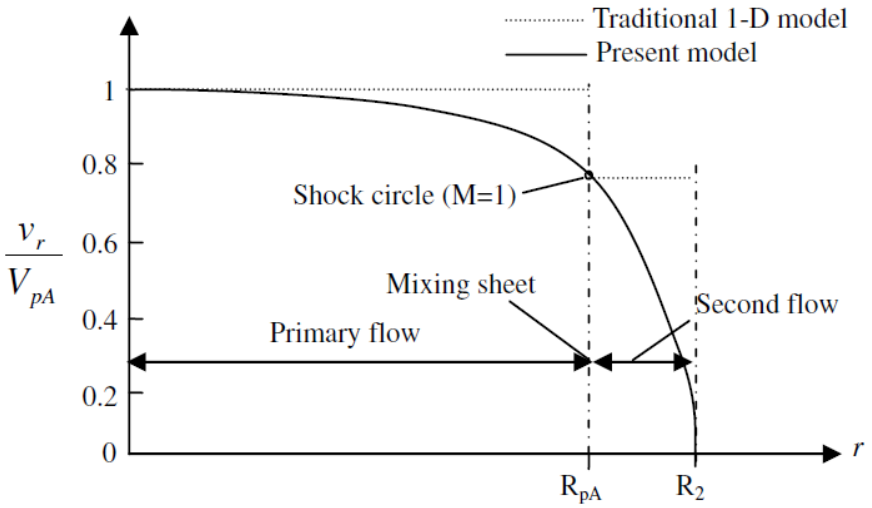

Figure 9: Velocity distribution of shock circle model compared to traditional 1-D model [27].

The shock circle model provides a slightly more realistic treatment of the two fluids by satisfying the no-slip boundary condition on the walls of the ejector [27]. It is once again assumed that the suction throat is located at the entrance to the constant-area section of the ejector. The developed model is then validated using the experimental data present in the publication by Huang et al.

In 2010, the comprehensive ejector model was introduced in literature by Liao and Best [19]. The comprehensive ejector model is a purely theoretical model which uses a multiple control volume approach, along with the conservation laws, to simulate the mixing of the motive and suction fluids from the exit plane of the motive nozzle to the exit of the diffuser [19]. There are no corrective coefficients present in this model, and thus the model relies on experimental data only for validation rather than model fitting. While the comprehensive ejector model benefits from an extension in predictive capabilities due to the purely theoretical treatment of ejector performance, the model also suffers from increased complexity and computational cost.

Other popular theoretical models in literature include the finite difference model [28], delayed equilibrium model [29], homogeneous equilibrium model [30], and method of characteristics [31]. Each of these models has powerful predictive capabilities. However, the discussion of these models is outside the scope of this thesis. Purely theoretical models, as well as purely empirical models, will be excluded from discussion for the remainder of the thesis. The early stages of this thesis focus on adapting the model proposed by Huang et al. for use in predicting the performance of the 2-stage ejector located in the altitude facility in ZL3 of Zucrow

Laboratories. It is determined that a simplified 1-D model is necessary to accurately predict the performance of this two-stage ejector system at relevant test conditions. The model development section of this thesis highlights the primary motivations surrounding the creation of a revised one-dimensional model and describes the calculation architecture for this new model.

4 MODELING DEVELOPMENT AND RESULTS

It was necessary to quickly develop an effective model which could accurately predict the performance of the large-scale two-stage ejector system at the altitude facility of Zucrow Labs. If possible, a simple model existing in literature would be implemented. Using an existing model would save on development time while still allowing for the accurate prediction of the two-stage ejector system. The primary model used in the preliminary stages of this thesis was contributed by Huang et al. [26]. For clarity, it is called the Huang Model within this thesis, as it was primarily implemented in the first semester of this thesis. This model has been widely cited in literature and is shown to produce good agreement with experimental results. This one-dimensional model falls into the semi-empirical modeling class and achieves near real-time ejector performance prediction capabilities while simultaneously maintaining sufficient prediction accuracy. While this model was originally created to define the performance of a single-stage ejector within a refrigeration system, we hoped that this model could be used with similar success for a two-stage vacuum ejector system.

As work on this thesis continued to progress, it became clear that the one-dimensional model proposed by Huang et al. was insufficient to properly predict the performance of the two-ejector system at Zucrow Laboratories. The theoretical results which informed this conclusion are given later in the thesis, along with a promising model which is potentially capable of extending the prediction capabilities of existing semi-empirical models.

4.1 Huang Model: Overview

From the literature review on existing ejector models, it was initially determined that the one-dimensional semi-empirical model proposed by Huang et al. was most appropriate for our applications. This model relies only on input values defining flow characteristics at the motive and suction inlets to the ejector system. This is a major benefit, as it is difficult to collect experimental data regarding flow conditions within the mixing and constant area sections of the ejector system without extensive design modifications. This input-based modeling architecture simplifies the testing procedure for collecting data necessary to properly inform the one-dimensional model. Furthermore, the calculation architecture for Huang et al.'s model is simple

relative to purely theoretical methodologies. Another advantage of a simple calculation architecture is that the model is less sensitive to changes in relevant parameters. In theory, this increased robustness requires less fine adjustment by the end user, making the model easier to use and troubleshoot.

As the final results of this thesis are not based upon the semi-empirical model proposed by Huang et al., the model's architecture is not discussed in complete detail. However, the assumptions in the model are given within this thesis, along with the equations relevant to the conclusions drawn during model development. Many of the assumptions made by Huang et al. are also used in the new model proposed within this thesis. The inclusion of the supporting assumptions and equations will help to form a more complete understanding regarding the motivations for creating a new model which is computationally more simplistic than that proposed by Huang et al.

The list given below is taken directly from the publication by Huang et al. [26], and summarizes all of the major assumptions that are made within the one-dimensional model.

1. The working (motive) fluid is an ideal gas with constant properties C_p and γ.
2. The flow inside the ejector is steady and one-dimensional.
3. The kinetic energy at the inlets of the motive and suction ports and the exit of diffuser are negligible.
4. For simplicity in deriving the 1-D model, the isentropic relations are used as an approximation. But to account for non-ideal processes, the effects of frictional and mixing losses are considered by using coefficients introduced in the isentropic relations. These coefficients are related to the isentropic efficiency and need to be determined experimentally.
5. After exhausting from the nozzle, the primary flow fans out without mixing with the entrained flow until some cross section *y–y* (hypothetical throat) which is inside the constant-area section.
6. The two streams start to mix at the cross section *y–y* (hypothetical throat) at uniform pressure, i.e. $P_{py} = P_{sy}$, before the shock which is at the cross section *s–s*.
7. The entrained flow is choked at the cross section *y–y* (hypothetical throat).
8. The inner wall of the ejector is adiabatic.

Based on assumption 4 given in the list above, there are four corrective coefficients which are introduced into the model's calculation architecture. The first corrective coefficient, η_p, is introduced into Equation (3) to account for non-isentropic losses in the motive converging-diverging nozzle when calculating the mass flow of motive gases.

$$\dot{m}_p = \frac{P_{p,0} A_t}{\sqrt{T_{p,0}}} \sqrt{\frac{\gamma_p}{R_p} \left(\frac{2}{\gamma_p + 1} \right)^{(\gamma_p+1)/(\gamma_p-1)}} \sqrt{\eta_p} \tag{3}$$

The second corrective coefficient in the model is introduced to account for losses in the suction flow. The model proposed by Huang et al. assumes that the suction fluid reaches sonic velocity at an annular throat in the entrance to the constant-area section of the ejector. As a result, the mass flow of suction gases can be calculated in the same way that mass flow is calculated through a converging-diverging nozzle. Equation (4) defines the mass flow of suction gases for the ejector and is identical to the equation for mass flow through a converging-diverging nozzle.

$$\dot{m}_s = \frac{P_{s,0} A_{sy}}{\sqrt{T_{s,0}}} \sqrt{\frac{\gamma_s}{R_s} \left(\frac{2}{\gamma_s + 1} \right)^{(\gamma_s+1)/(\gamma_s-1)}} \sqrt{\eta_s} \tag{4}$$

There is also a corrective coefficient which accounts for losses relevant to the expansion of the motive plume leading into the constant area section of the ejector. As stated in assumptions 5 and 6, the gases exiting the motive nozzle continue to expand isentropically until the static pressure of the motive fluid is equivalent to the static pressure of the suction fluid at sonic velocity. Equation (5) is used to calculate the final expanded area of the motive flow, and it includes a corrective coefficient, $\emptyset_p$, to account for these expansion losses.

$$\frac{A_{py}}{A_{p1}} = \frac{\frac{\emptyset_p}{M_{py}}\left[\frac{2}{\gamma_p+1}\left(1+\frac{\gamma_p-1}{2}{M_{py}}^2\right)\right]^{(\gamma_p+1)/(2(\gamma_p-1))}}{\frac{1}{M_{p1}}\left[\frac{2}{\gamma_p+1}\left(1+\frac{\gamma_p-1}{2}{M_{p1}}^2\right)\right]^{(\gamma_p+1)/(2(\gamma_p-1))}} \quad (5)$$

The final corrective coefficient, $\emptyset_m$, is defined to account for momentum losses within the constant area section of the ejector during mixing between the motive and suction fluids. Equation (6) utilizes conservation of momentum to determine the velocity of the mixed flow.

$$\emptyset_m\left(\dot{m}_p V_{py} + \dot{m}_s V_{sy}\right) = \left(\dot{m}_p + \dot{m}_s\right)V_m \quad (6)$$

There are two constraints which are introduced in the Huang Model architecture. First, the sum of the suction and motive flow areas must be equivalent to the flow area in the constant-area section of the ejector. This is a geometrical constraint, and it is satisfied using the appropriate combination of $\emptyset_p$ and η_s values. Second, the static pressure at the exit plane of the ejector-diffuser must be greater than or equal to the ambient pressure (14.7 psia for a single-stage ejector). This constraint acts to account for the critical back pressure of the system. Different combinations of these four corrective coefficients are inserted into the model. The combination of coefficient values defined for a given experimental data point is that which satisfies the constraints defined within the equation.

4.2 Huang Model: Sensitivity Analysis Results

The model proposed by Huang et al. was first used to determine the impact of different motive and suction flow parameters on the performance of the single-stage ejector system. This characterization step was important, as the two-stage ejector system would eventually handle rocket exhaust products with varying static temperatures, heat capacities, and molecular weights. As Huang et al. had already experimentally validated the one-dimensional model, it was assumed that the modeling results could be used as a preliminary estimate of performance. For this

reason, some early conclusions were drawn from the modeling results before in-house validation was completed.

It was determined experimentally by Huang et al. that the corrective coefficients were relatively insensitive to changes in flow parameters [26]. For this reason, the coefficient values defined experimentally by Huang et al. were used to determine the impact of different flow parameters on the performance of the ejector system. This analysis varied eight input parameters to determine the impact of different motive and suction flow characteristics on the performance of the ejector system. The performance of the ejector system is defined to be the maximum entrainment ratio for a given suction total pressure. The entrainment ratio is defined as the ratio of suction mass flow to motive mass flow, and it helps to describe the overall efficiency of the ejector. The entrainment ratio capability is defined for the full range of motive total pressures that can be supplied to the single-stage ejector. The first flow parameter to be varied is motive stagnation temperature, and the results of this analysis are given in Figure 10.

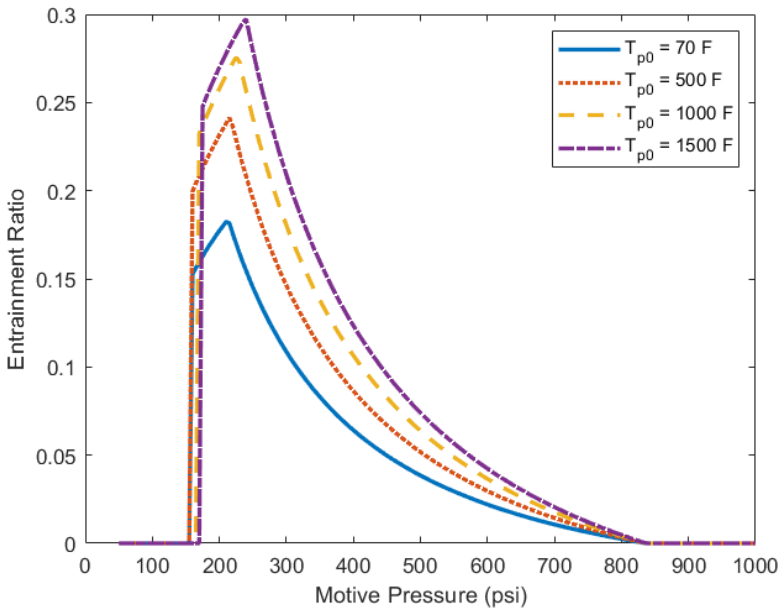

Figure 10: Impact of motive stagnation temperature on single-stage ejector performance.

As can be seen in Figure 10, increasing the stagnation temperature of the motive fluid acts to increase the relative performance of the ejector system. This may seem counter-intuitive initially, as an increase in motive stagnation temperature yields a decrease in motive mass flow

given otherwise constant flow conditions. However, the main mixing for this model is determined using conservation of momentum. The increase in motive stagnation temperature yields a proportional increase in motive mixing temperature. This higher mixing temperature corresponds to a higher speed of sound, and thus higher momentum value for the motive fluid during mixing. It is also important to note that decreasing the motive mass flow improves the entrainment ratio, assuming that the entrainment capacity of the ejector system is otherwise unchanged.

One behavior present in the graphs of Figure 10 through Figure 15 is a cutoff after some minimum motive pressure. This cutoff is an artifact of the model's calculation architecture. The modeling background of this thesis mentions a critical back pressure at which the ejector transitions from critical to sub-critical operation mode. In this model, it is assumed that the suction flow fails to choke in the constant-area section of the ejector during sub-critical operation. As the kinetic energy of the motive stream decreases, the pressure recovery capability of the ejector also decreases. The cutoff point in the graphs signifies the motive pressure at which the energy throughput of the motive flow is insufficient to sustain choking of both the motive and suction flows. The next flow parameter to be analyzed is the suction stagnation temperature, and the results of the analysis are given in Figure 11.

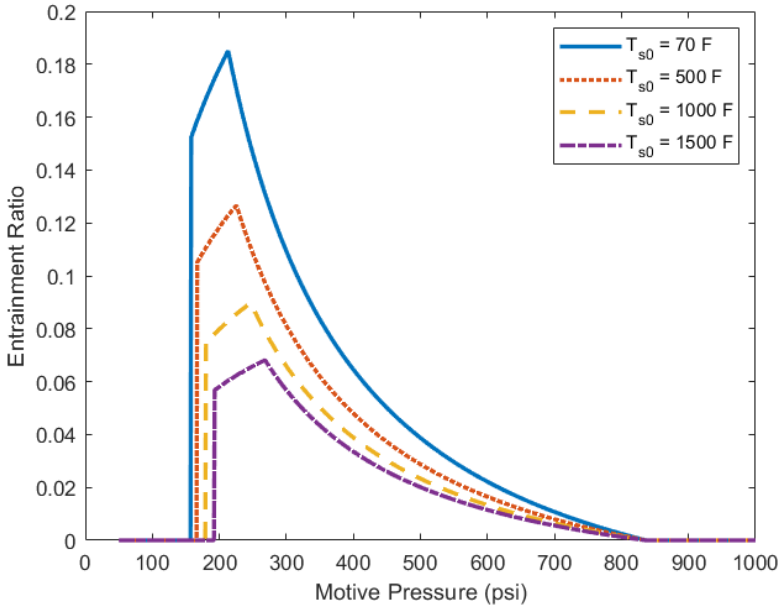

Figure 11: Impact of suction stagnation temperature on single-stage ejector performance.

From the results shown in Figure 11, the relationship between suction stagnation temperature and ejector performance is opposite that of motive stagnation temperature. As the suction stagnation temperature increases, the relative performance of the ejector system decreases. This result can be attributed to a different balance between mass flow restriction and momentum improvement for this parameter. The suction flow makes no contribution of momentum in the mixing process, and therefore does not benefit as greatly from the temperature increase. Decreasing the suction mass flow rate also acts to decrease the entrainment ratio, yielding a reduction in overall ejector performance. For this reason, it is advantageous to use a suction fluid with a low stagnation temperature. The results for the parametric analysis of motive molecular weight are given in Figure 12.

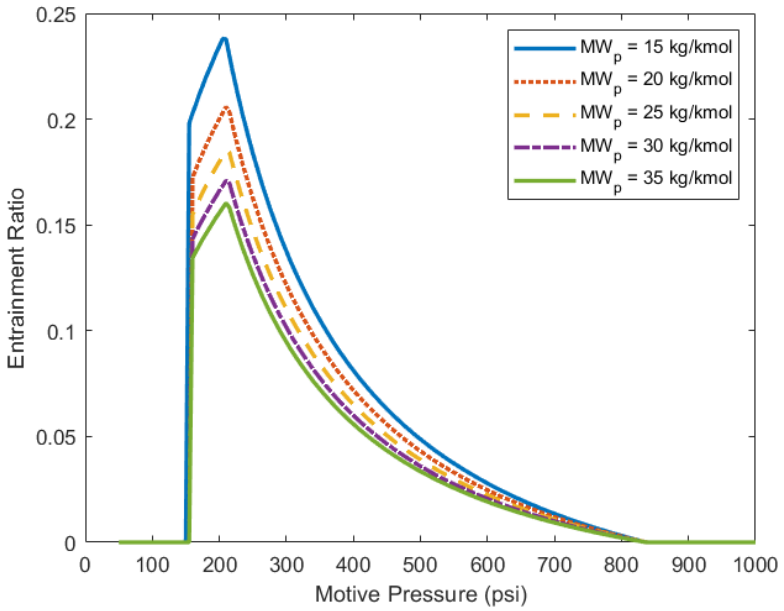

Figure 12: Results showing impact of motive molecular weight on single-stage ejector performance.

From the results displayed in Figure 12, it is shown that increasing the molecular weight of the motive fluid decreases the overall performance of the ejector system. The molecular weight of the motive fluid is introduced into two main equations within the modeling architecture, in the form of the specific gas constant for the fluid of interest. A higher molecular weight yields a higher mass flow at the throat of the motive nozzle. However, this higher molecular weight also yields a lower speed of sound for the motive fluid during mixing. The modeling result implies that the influence of molecular weight on the speed of sound, and thus total energy present in mixing, is more significant than the impact on motive mass flow. This can be seen in the equations, as mass flow varies by $\sqrt{MW}$ while the total energy of the motive flow varies by $^{1}/_{MW}$. The equations support the result of this parametric analysis, implying that a lower molecular weight fluid is preferable for the motive stream due to an increase in kinetic energy. The results for the parametric analysis suction molecular weight are given in Figure 13.

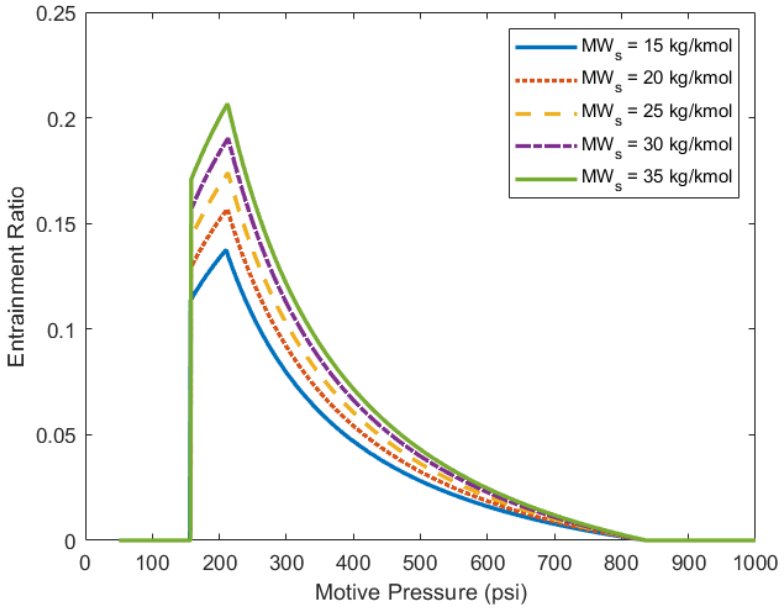

Figure 13: Results showing impact of suction molecular weight on single-stage ejector performance.

As can be seen in Figure 13, increasing the suction molecular weight acts to increase the overall performance of the ejector system. The same two equations are used for this portion of the analysis. The suction mass flow increases with increasing suction molecular weight. This yields a higher entrainment ratio, and it accounts partially for the improvement in ejector performance. The higher molecular weight also yields a lower overall kinetic energy for the system. Though the functional influence of molecular weight on the two equations of interest remains unchanged, the energy of the suction flow is much less significant to performance than that of the motive flow. As the ejector is primarily an energy conversion device, the detriment of a slightly lower suction kinetic energy is outweighed by the dramatic increase in suction mass flow capability. The final parameter of interest is the heat capacity ratio, γ. The results for the parametric analysis of motive heat capacity ratio are provided in Figure 14.

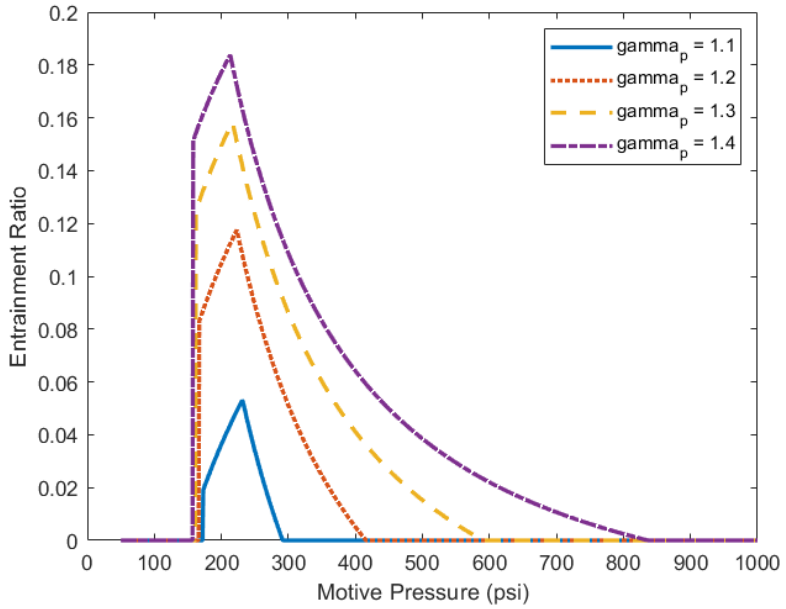

Figure 14: Results showing impact of motive heat capacity ratio on single-stage ejector performance.

As can be seen from the results presented in Figure 14, increasing the motive heat capacity ratio acts to improve overall ejector performance. Air and nitrogen have a heat capacity ratio of approximately 1.4, and thus are good candidates to be used as the motive fluid. The results of the parametric analysis of suction heat capacity ratio are given in Figure 15.

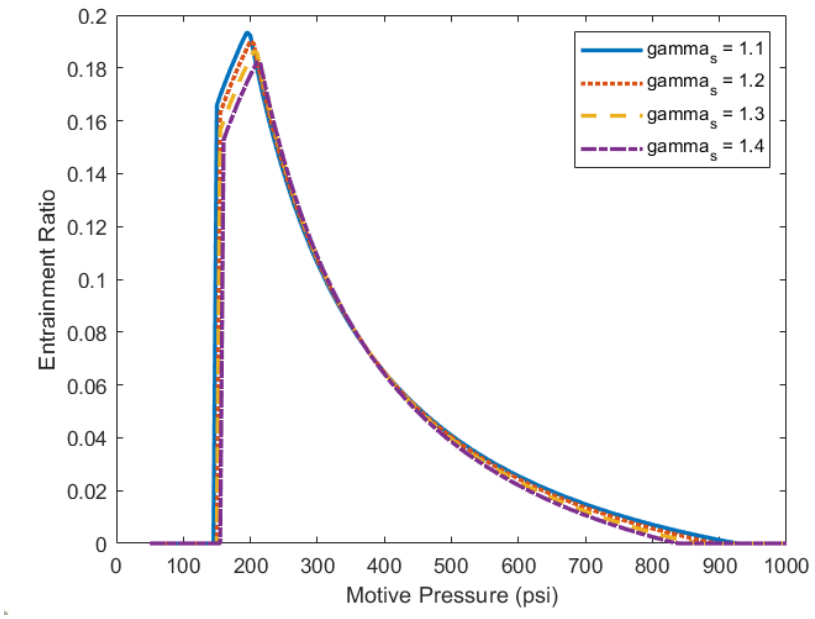

Figure 15: Results showing impact of suction heat capacity ratio on single-stage ejector performance.

Figure 15 suggests that the suction heat capacity ratio has little influence on the overall performance of the ejector system. This parametric analysis set defines the sensitivity of ejector performance to all relevant input conditions, helping to form a more complete functional understanding of ejector systems. By parameterizing the performance of the ejector, it is also possible to determine what combination of motive and suction fluid characteristics would yield an optimum ejector behavior. The results of the individual sensitivity analyses discussed above are summarized in the sensitivity plot given in Figure 16. This sensitivity plot defines the influence of each parameter on the entrainment ratio of the single-stage ejector relative to a nominal reference case. Each of the input parameters is varied by 10%, so that the influence of the six parameters can be compared. Each motive parameter is also given the same range as its suction counterpart to help facilitate this comparison. The low, reference, and high values for each of the six input parameters are also provided in Figure 16.

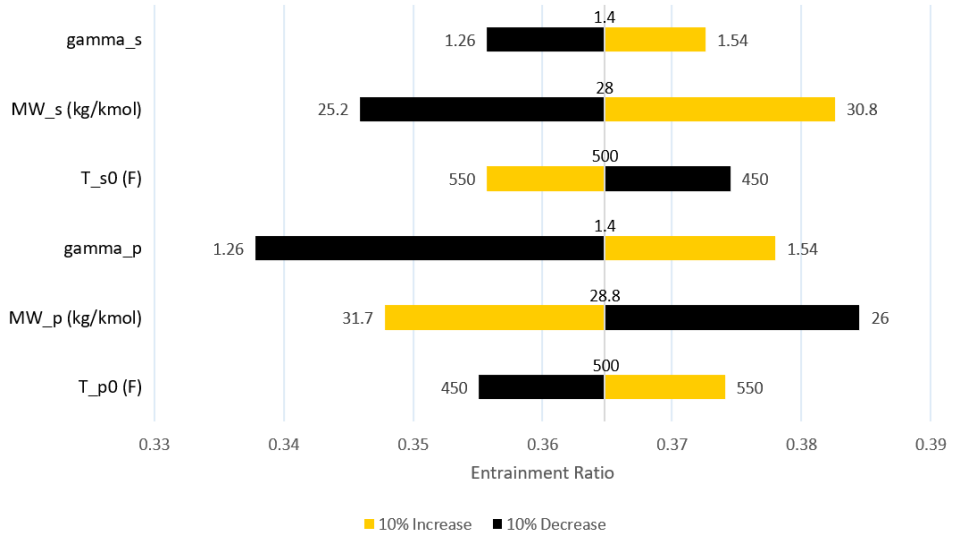

Figure 16: Sensitivity graph showing the influence of 10% changes to the input parameters.

Figure 16 shows the relative influence of each parameter on the entrainment ratio for the single-stage ejector. There are a few conclusions that can be made from this graph. First, it is advantageous to use a high stagnation temperature motive fluid. This can be attributed to the increase in chemical energy with increasing temperature, as the energy contribution of the motive fluid is the primary driver in pressure recovery within the ejector system. On the other hand, the entrainment ratio capability of the single stage ejector decreases with increasing suction stagnation temperature. The density of the suction fluid decreases with increasing temperature, implying a reduction in momentum transfer between the suction and motive fluids during mixing. Increasing the motive molecular weight acts to increase the motive mass flow while simultaneously decreasing the velocity of the motive fluid during mixing. Both of these factors decrease the entrainment ratio capability of the ejector, and this is supported by the results given in Figure 16. In contrast, the entrainment ratio benefits from an increase in suction molecular weight, indicating a preference toward high molecular weight suction fluids during testing. Increases in both the motive and suction heat capacity ratios are shown to yield an increase in entrainment ratio. However, this analysis implies that the performance of the ejector is more responsive to changes in the motive heat capacity ratio when compared with suction heat capacity ratio.

While this preliminary sensitivity analysis is useful for determining the fundamental influence of each parameter on ejector performance, we also wanted to estimate the response of

entrainment ratio to these parameters over ranges which were more indicative of real world testing conditions. The three motive fluids chosen as candidates for this second sensitivity analysis were steam, argon, and air. The physical characteristics for each of these three candidate fluids are summarized in the table below.

Table 3: Fluid characteristics for argon, steam, and air.

Motive Fluid	**Molecular Weight [kg/kmol]**	**Heat Capacity [J/(kg*K)]**	**Heat Capacity Ratio**
Argon	39	520	1.67
Steam	18	2260	1.28
Air	28	1010	1.4

The range of motive stagnation temperatures for this sensitivity analysis were defined based on the current fluid heating capabilities at ZL3 of Zucrow Labs. Ambient temperature was defined as the lower bound for this analysis, while the upper bound of 800°F was defined based on the maximum capability of the air heater at Zucrow Labs.

It was then necessary to determine the appropriate ranges for each suction parameter. This was accomplished by running test cases with common propellant combinations using CEA. For each of the test cases, a chamber pressure of 500 psia and an exit pressure of 5 psia was used. The results for each of the evaluated test cases are given in Table 4. The results of the sensitivity analysis using the bounds defined in Table 3 and Table 4 are given in Figure 17.

Table 4: Test cases evaluated to determine bounds for suction fluid parameters.

Oxidizer	**Fuel**	O/F_{opt}	**Temperature [K]**	**MW [kg/kmol]**	**Heat Capacity [J/(kg*K)]**	**Heat Capacity Ratio**
LOX	RP-1	2.5	2056	24	2108	1.19
LOX	LH_2	4	1178	10	3699	1.29
LOX	Methane	3	1879	21	2316	1.2
N_2O_4	UDMH	0.4	1743	24	1865	1.22

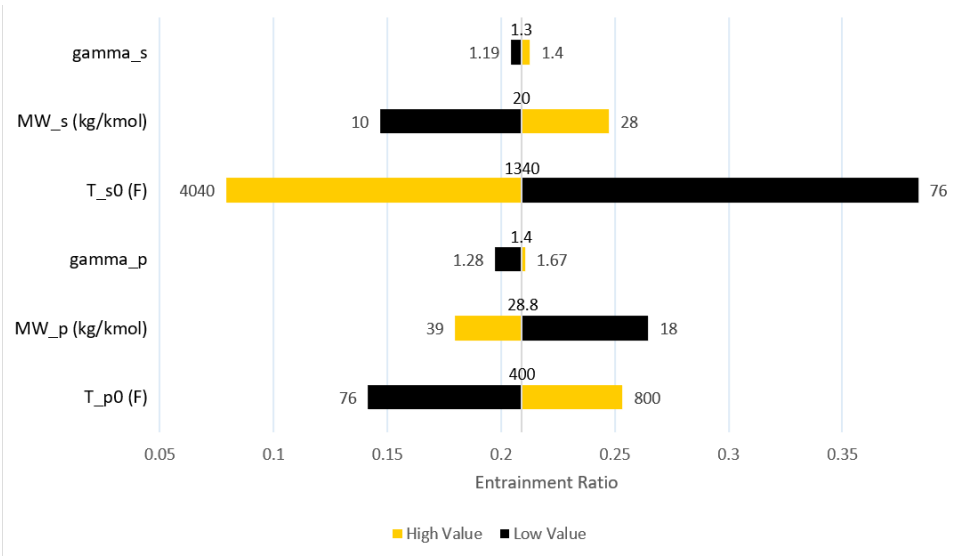

Figure 17: Sensitivity graph showing the influence of input parameters over real-world operating ranges.

The large difference in variation for each of the parameters can be seen in *Figure 17*. The results imply that the heat capacity ratio of the motive and suction fluids has a small impact on ejector performance under real testing conditions. Suction temperature is shown to be the most influential parameter on ejector performance, primarily due to its large operational range. A high stagnation temperature and low molecular weight is shown to be the best combination for the motive fluid. This result helps to explain why steam is frequently used as the motive fluid for ejector systems in industry.

This procedural analysis was then modified to determine the sensitivity of simulated altitude within the altitude chamber to these input parameters. While the previous analysis describes the efficiency of the ejector system under different testing conditions, the treatment of simulated altitude directly informs testing capabilities at various operating conditions. The real-world bounds defined in Table 3 and Table 4 were used again, and the results of this final sensitivity analysis are provided in Figure 18. This sensitivity analysis was performed assuming a suction mass flow of 0.033 kg/s, which corresponds to a 100 Newton rocket with an *Isp* of 300 seconds.

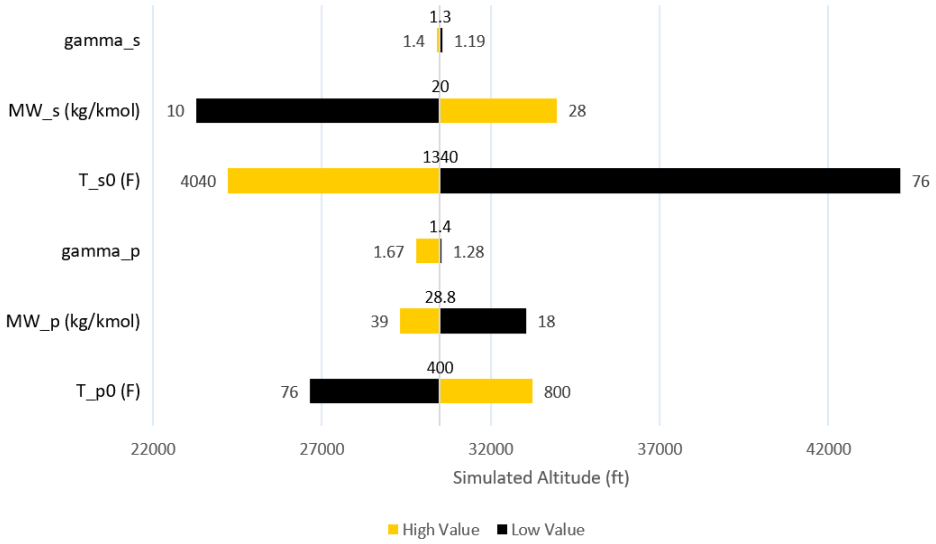

Figure 18: Sensitivity graph showing the response of simulated altitude to each input parameter.

From Figure 18, suction stagnation temperature is shown to be the most influential parameter for simulated altitude capabilities. The results again suggest that a high stagnation temperature, low molecular weight motive fluid yields the highest simulated altitude. The simulated altitude capability of the ejector is relatively insensitive to changes in both the motive and suction heat capacity ratio. Each of these three individual sensitivity graphs helps us develop a full understanding regarding the influence of each parameter on the testing capabilities for the altitude facility.

4.3 Huang Model: Single-Stage Ejector Characterization Results

Following this parametrization of the ejector models, it was then necessary to validate the Huang model using experimental data collected in-house. The results of this experimental model validation were shown to necessitate a new, more simplistic, model which used fewer corrective coefficients. An experimental testing campaign was conducted in the Spring of 2018 as part of a class project for AAE 535, Propulsion Design Build Test. In this testing campaign, the class group characterized the full operational range of the single-stage ejector. A picture of the single-stage ejector is given in Figure 19, along with the relevant dimensions in the table following the figure.

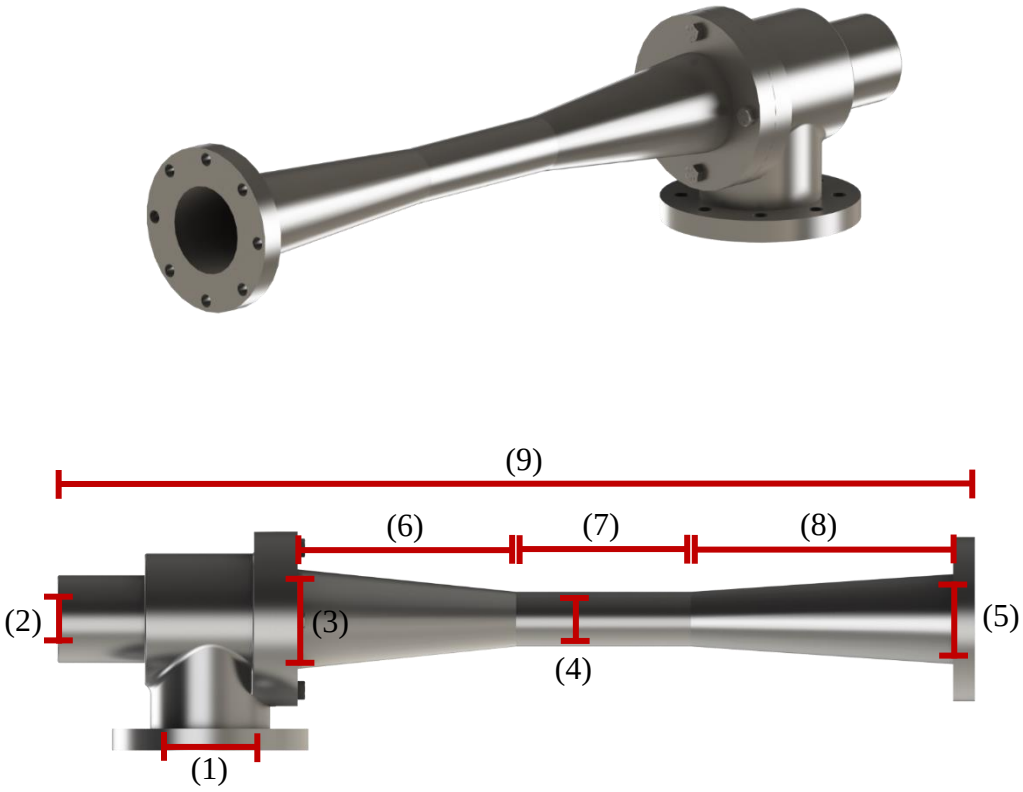

Figure 19: CAD rendering of single-stage ejector.

Table 5: Relevant dimensions of single-stage ejector.

#	**Dimension**	**Value**
(1)	Suction Inlet Diameter (inch)	4
(2)	Motive Inlet Diameter (inch)	2.5
(3)	Pre-contraction Diameter (inch)	4.5
(4)	Constant Section Diameter (inch)	2.25
(5)	Diffuser Exit Diameter (inch)	4
(6)	Contracting Length (inch)	10
(7)	Constant Area Section Length (inch)	8
(8)	Sub-sonic Expansion Length (inch)	12
(9)	Total Length (inch)	42.5

As can be seen from the dimensions provided in Table 5, the single-stage ejector is significantly smaller than the two-stage ejector characterized later in the thesis. However, it was

convenient to use this smaller single-stage ejector system to help validate the model introduced by Huang et al. while the two-stage ejector system was being assembled. By collecting this experimental data using a slightly smaller ejector, we hoped that the model could be validated so as to predict the performance of the two-stage ejector in the future. Another part of the class project was to characterize the performance of the ejector using three motive nozzles with different expansion ratios. The relevant dimensions for the three motive nozzles are provided in Table 6.

Table 6: Table displaying all relevant dimensions for the three nozzles.

	Low ER Nozzle	**Original Nozzle**	**High ER Nozzle**
Throat Diameter (inch)	0.495	0.495	0.495
Exit Diameter (inch)	1.07	1.20	1.44
Total Length (inch)	4.15	4.15	4.15
Expansion Ratio (ER)	4.67	5.88	8.5

Each of the two new motive nozzles were machined from 316 Stainless Steel at the Aerospace Sciences Laboratory (ASL) at Purdue University. This testing campaign made use of facility nitrogen as the suction fluid and facility air as the motive fluid. A Plumbing and Instrumentation Diagram (P&ID) describing the testing arrangement is given in Figure 20.

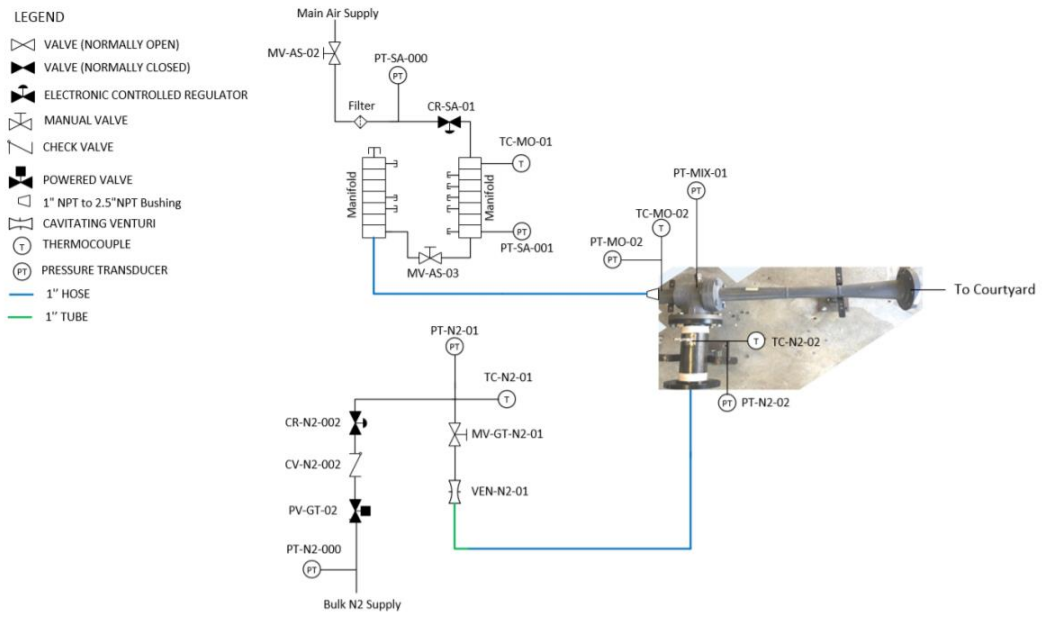

Figure 20: P&ID describing the experimental configuration for the performance characterization of the single-stage ejector.

By varying the facility nitrogen stagnation pressure upstream of the venturi, we were able to produce a full range of suction mass flow rates from 0 to 0.7 lb_m/s of nitrogen. In the first testing campaign, we characterized the performance of the single-stage ejector using the original motive nozzle supplied by the manufacturer. The motive nozzle provided by the factory was designed to achieve peak performance at a motive stagnation pressure of 215 psia. The primary variables of interest for the experimental test were motive stagnation pressure, motive stagnation temperature, suction mass flow rate, suction stagnation pressure, and suction stagnation temperature. A motive nozzle isentropic efficiency of 0.993 was used for all experimental testing campaigns. This was the same non-isentropic coefficient value used to calculate the motive mass flow during experimental testing. The results for the first testing campaign using the original motive nozzle are given in Figure 21.

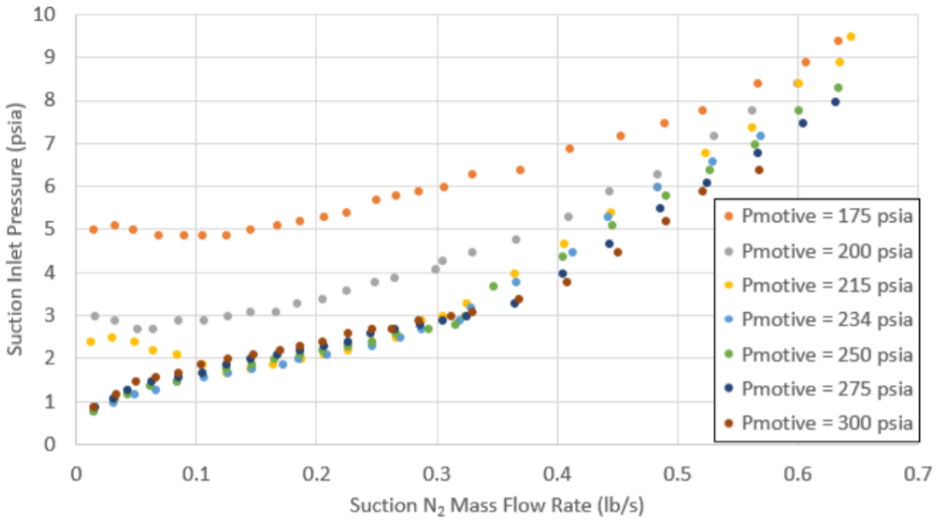

Figure 21: Results from the first experimental testing campaign for single-stage ejector with original motive nozzle.

A simplifying assumption made during analysis is that the motive and suction stagnation temperatures remain unchanged over the course of the experimental test. For this reason, the temperature of the motive/suction flows are not discussed within the context of the subsequent analysis. There are a few conclusions that can be drawn from the experimental results. First, increasing the stagnation pressure of the motive fluid improves ejector performance only to a certain point. Increasing the motive stagnation pressure above the design pressure of 215 psia yields no performance improvement for suction mass flow rates between 0 and 0.3 lb_m/s, and it yields only a minimal performance improvement for suction mass flow rates higher than 0.3 lb_m/s. The experimental results for the two other nozzles are given in Figure 22 and Figure 23.

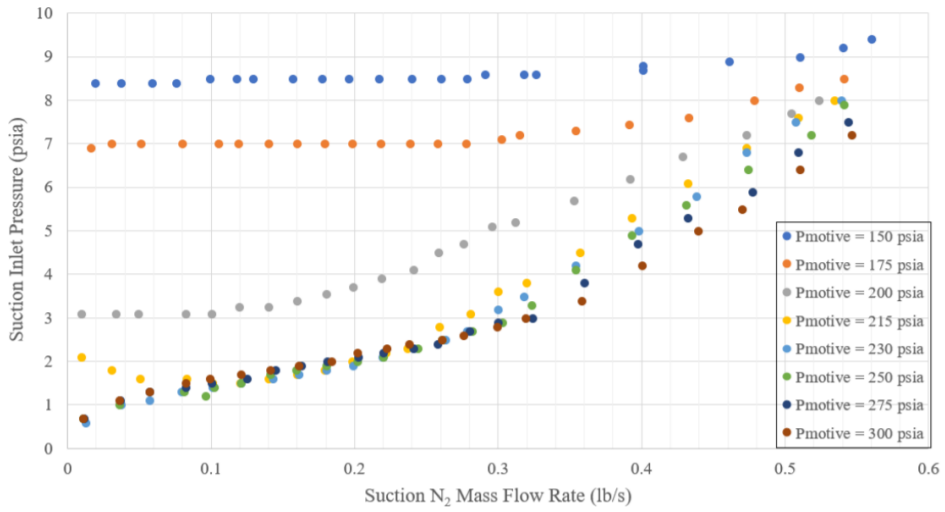

Figure 22: Graph of experimental results for 8.5 expansion ratio nozzle.

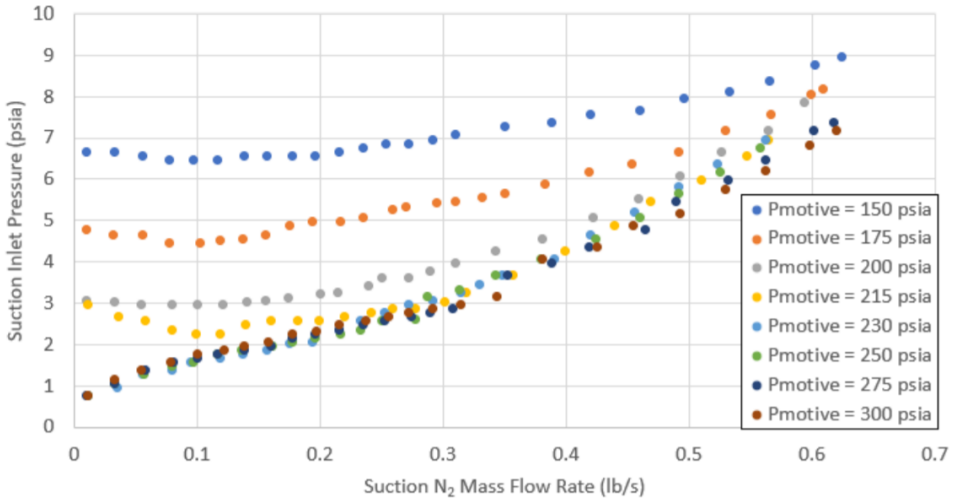

Figure 23: Graph of experimental results for 4.67 expansion ratio nozzle.

From the results shown in Figure 22, the pressure recovery capability of the ejector at motive stagnation pressures below 215 psia suffers when compared with the original nozzle geometry presented in Figure 21. However, the minimum suction pressure reached using the 8.5 expansion ratio nozzle at 215 psia is approximately 1.5 psia, as compared with 1.8 psia for the original nozzle geometry. At the design pressure of 215 psia, the motive fluid expands just enough to impinge with the walls of the constant-area section of the ejector. As the higher expansion ratio nozzle yields a lower nozzle exit pressure, the suction pressure must decrease accordingly to achieve the same optimum level of motive plume expansion. The inverse of this

result can be seen in Figure 23. As the motive gas at the exit plane of the 4.5 expansion ratio nozzle is more under-expanded when compared to the higher expansion ratio nozzles, the suction pressure must increase accordingly to achieve the same optimum level of motive plume expansion.

Using the data collected for the three motive nozzle geometries, the corrective coefficients present in the semi-empirical model proposed by Huang et al are determined. The corrective coefficient determination was accomplished using a simple grid search algorithm in Matlab. In order to simplify the search procedure, the motive nozzle isentropic efficiency introduced in the model is set to a constant value of 0.993. This is the same value used to define the discharge coefficient when experimentally calculating nozzle mass flow. Setting the motive nozzle corrective coefficient to a constant value helped to simplify the search, as only three corrective coefficients had to be determined. The impact of this simplification can be better understood using a simple example. If there is one corrective coefficient with 10 possible values, there are only ten combinations which must be evaluated. If there are two corrective coefficients with 10 possible values each, there are 100 possible combinations. There are 1,000 possible combinations with three corrective coefficients, and 10,000 with four corrective coefficients. If there are 100 possible values for each corrective coefficient, determining four corrective coefficients then requires the evaluation of 100,000,000 combinations. As the number of corrective coefficients increases, increased resolution becomes exponentially more costly. For this reason, it is important to introduce corrective coefficients only when absolutely necessary. The set of corrective coefficient values which satisfied each of the experimental data points is determined and shown graphically in Figure 25, Figure 26, and Figure 27. The analysis procedure is summarized in the flow chart in Figure X, for reference.

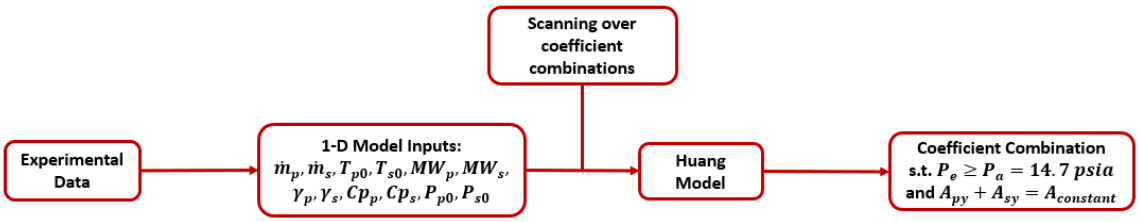

Figure 24: Flow chart describing model analysis architecture for Huang Model.

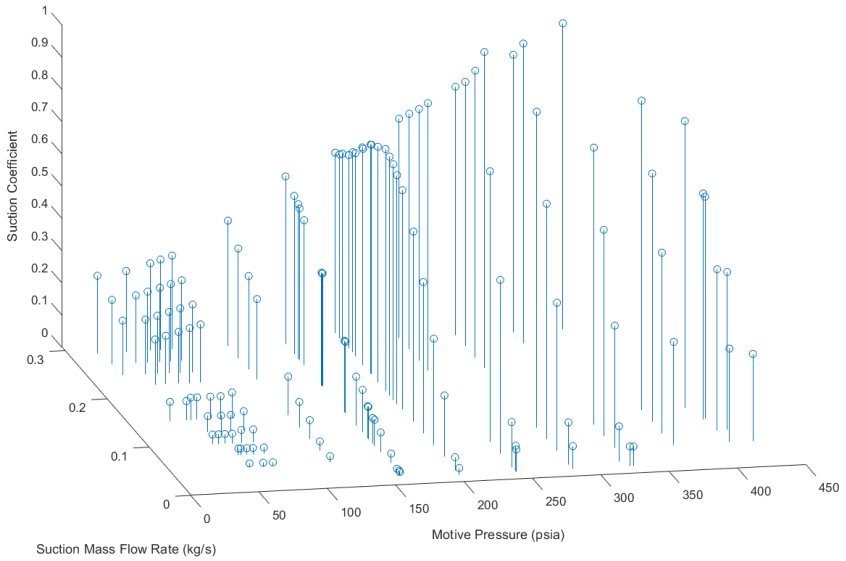

Figure 25: Graph showing satisfactory suction coefficient values for motive pressure and suction mass flow range of single-stage ejector.

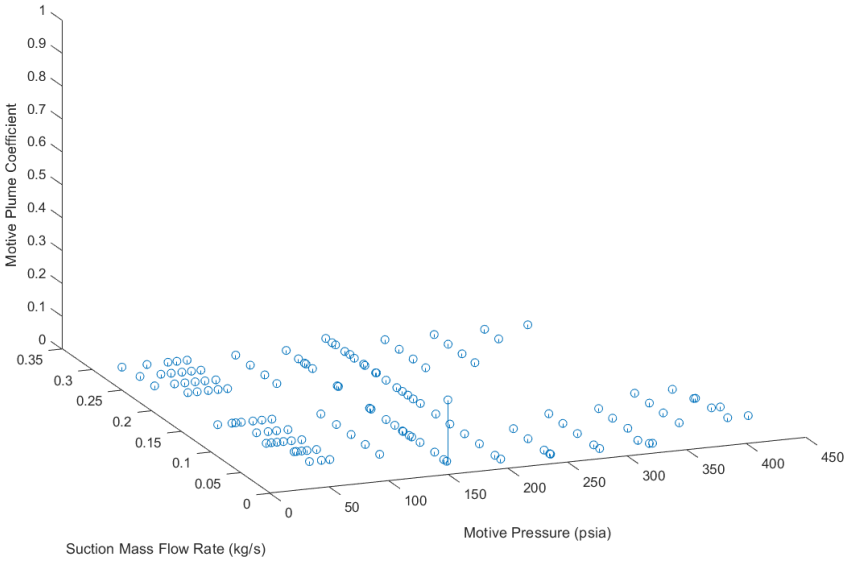

Figure 26: Graph showing satisfactory motive plume coefficient values for motive pressure and suction mass flow range of single-stage ejector.

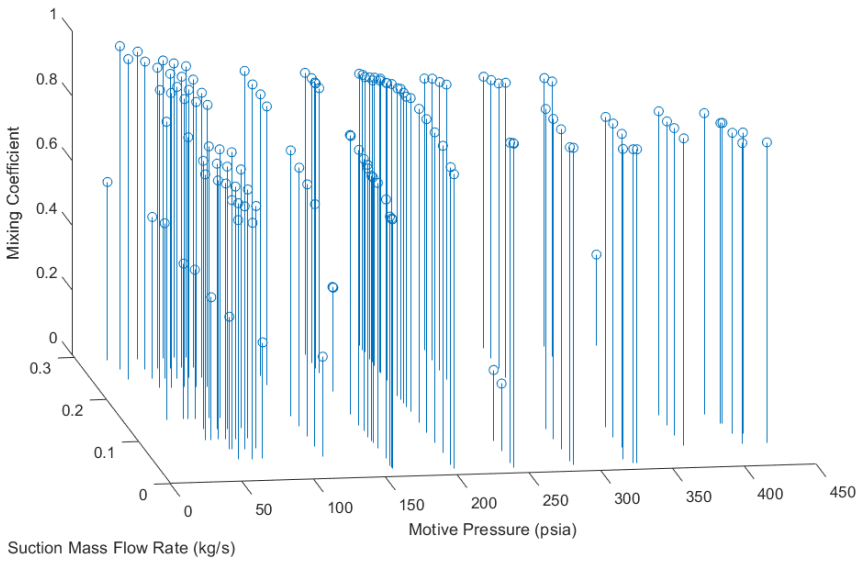

Figure 27: Graph showing satisfactory mixing coefficient values for motive pressure and suction mass flow range of single-stage ejector.

From the results given in Figure 25, there exists a discernable relationship between suction coefficient, motive stagnation pressure, and suction mass flow rate. This relationship allows for the development of a parametric curve fit which defines the value of the suction coefficient over the operational range of the ejector; even between experimental data points. However, there is no discernable trend for the motive plume and mixing coefficients. As a result, it is not possible to reliably create a curve fit to define the value of these two coefficients. This is an issue, as each of the three corrective coefficients must be well-defined over the full operational range of the ejector. A large portion of time was spent trying to determine a methodology to produce smooth, reliable results for these two coefficients, with no success.

Furthermore, evaluating the 165 experimental data points collected for the original motive nozzle configuration took a relatively long time when compared to the final model proposed within this thesis. Using a 1% resolution (100 points between 0 and 1) for each of the three variable coefficients required nearly an hour of computational time. While this computation time does not necessarily seem obstructively high, it is important to remember that this model will eventually be used with a two-stage ejector system. Each of the two stages will have these three corrective coefficients and will require a comparable level of resolution. This means determining the performance of the two-stage ejector system will require roughly

1,000,000,000,000 combination evaluations for each experimental data point, as compared with 1,000,000 for a single-stage ejector system. This increase in evaluations will result in a proportional increase in computational time, making this model infeasible at any reasonable level of resolution. With these modeling results and conclusions in mind, a new model is created which introduces only one corrective coefficient. The new model is successfully validated using the same experimental data, and it produces smooth fittable curves for the included corrective coefficient under a minute.

4.4 New Model: Overview

As many of the equations used in the new model are identical to those in the model proposed by Huang et al., they are only introduced in the context of the new model. However, mention is made of any equations which are derived from the previous model proposed by Huang et al. The calculation procedure begins with the motive gas in the converging-diverging nozzle of the ejector. Equation (7) is taken directly from the Huang Model, and it is used to determine the mass flow of motive gas in the converging-diverging nozzle. The nozzle isentropic efficiency is set to a constant value of 0.993, for reasons previously mentioned.

$$\dot{m}_p = \frac{P_{p,0} A_t}{\sqrt{T_{p,0}}} \sqrt{\frac{\gamma_p}{R_p} \left(\frac{2}{\gamma_p + 1} \right)^{(\gamma_p+1)/(\gamma_p-1)}} \sqrt{\eta_p} \tag{7}$$

The Mach number at the exit plane of the motive converging-diverging nozzle is determined using Newton's method; the code supporting this calculation is given in the appendix for reference. The determined Mach number can be used along with Equation (8) to determine the static pressure at the exit of the motive converging-diverging nozzle. The static temperature at the exit plane of the nozzle is determined using Equation (9). Equation (8) and Equation (9) are shared with the Huang Model.

$$P_{p1} = P_{p0} \left(1 + \frac{\gamma_p - 1}{2} {M_{p1}}^2 \right)^{\frac{-\gamma_p}{\gamma_p - 1}} \tag{8}$$

$$T_{p1} = T_{p0}\left(1 + \frac{\gamma_p - 1}{2} {M_{p1}}^2\right)^{-1} \tag{9}$$

At this point in the model, an assumption is made that mixing between the motive and suction fluids cannot begin until the motive and suction fluids are at equal pressure. If the motive static pressure is higher than the suction static pressure, the motive Mach number is recalculated using Equation (10). This equation is simply a manipulation of the isentropic relation between static pressure and stagnation pressure, and it defines the Mach number necessary for the motive static pressure to match the suction static pressure.

$$M_{p2} = \sqrt{\frac{2}{\gamma_p - 1}\left[\left(\frac{P_{p1}}{P_{s0}}\right)^{\frac{\gamma_p - 1}{\gamma_p}}\left(1 + \frac{\gamma_p - 1}{2} {M_{p1}}^2\right) - 1\right]} \tag{10}$$

The static temperature following this expansion can again be calculated using isentropic relations. If the static pressure of the suction fluid is higher than that of the motive static pressure, the suction Mach number is calculated using Equation (11).

$$M_{s2} = \sqrt{\frac{2}{\gamma_s - 1}\left[\left(\frac{P_{s0}}{P_{p1}}\right)^{\frac{\gamma_s - 1}{\gamma_s}} - 1\right]} \tag{11}$$

The static temperature of the suction fluid is then determined using isentropic relations. After determining the Mach numbers and static temperatures at the inlet of the control volume, it is then necessary to determine the cross-sectional area for each of the two flows. The cross-sectional area of the motive flow is determined using Equation (12); this equation is taken directly from the Huang Model.

$$\frac{A_{p2}}{A_{p1}} = \frac{M_{p1}\left[\frac{2}{\gamma_p+1}\left(1+\frac{\gamma_p-1}{2}{M_{py}}^2\right)\right]^{(\gamma_p+1)/(2(\gamma_p-1))}}{M_{p2}\left[\frac{2}{\gamma_p+1}\left(1+\frac{\gamma_p-1}{2}{M_{p1}}^2\right)\right]^{(\gamma_p+1)/(2(\gamma_p-1))}} \tag{12}$$

It is assumed that mixing between the motive and suction fluids begins at the inlet to the contracting section between the mixing chamber and constant-area section of the ejector; the mixing between the two fluids occurs at equal pressure. As a result, the cross-sectional area of the suction fluid is determined by subtracting the motive flow area from the area at the inlet to the contracting section of the ejector.

$$A_{s2} = A_{contract} - A_{p2} \tag{13}$$

The heat capacity, heat capacity ratio, and molecular weight of the mixed flow are calculated as the weighted average of the motive and suction values. The calculation of these three mixed values is accomplished using Equation (14), Equation (15), and Equation (16), respectively.

$$C_{p,mix} = \frac{\dot{m}_p C_{p,p} + \dot{m}_s C_{p,s}}{\dot{m}_p + \dot{m}_s} \tag{14}$$

$$\gamma_{mix} = \frac{\dot{m}_p \gamma_p + \dot{m}_s \gamma_s}{\dot{m}_p + \dot{m}_s} \tag{15}$$

$$MW_{mix} = \frac{\dot{m}_p MW_p + \dot{m}_s MW_s}{\dot{m}_p + \dot{m}_s} \tag{16}$$

The main control volume calculation present in the new model uses conservation of energy and momentum to calculate the Mach number and static temperature of the mixed flow. Equation (17) utilizes conservation of momentum to determine the resulting Mach number of the mixed flow. A momentum coefficient is introduced into this equation to account for mixing losses not captured in the equations of the new model; this is the only corrective coefficient introduced within the model architecture.

$$P_{mix}A_{mix}\left(1+\gamma_{mix}{M_{mix}}^2\right)=\eta_m\left[P_{p2}A_{p2}\left(1+\gamma_p{M_{p2}}^2\right)+P_{s2}A_{s2}\left(1+\gamma_s{M_{s2}}^2\right)\right] \quad (17)$$

It was assumed previously that mixing between the motive and suction fluids occurs at constant pressure. As a result, all of the pressure terms can be canceled out of the equation. It is also assumed that the mixing process ends in the constant area section of the ejector. Isolating M_{mix} yields Equation (18), given below.

$$M_{mix}=\sqrt{\frac{\eta_m A_{p2}}{\gamma_{mix}A_{mix}}\left(1+\gamma_p{M_{p2}}^2\right)+\frac{\eta_m A_{s2}}{\gamma_{mix}A_{mix}}\left(1+\gamma_s{M_{s2}}^2\right)-\frac{1}{\gamma_{mix}}} \quad (18)$$

Conservation of energy is then used, along with the calculated Mach number for the mixed flow, to determine the mixed static temperature. Equation (19) is adapted from the Huang Model, and it is a manipulation of the equation for conservation of energy.

$$\dot{m}_{mix}\left(C_{p,mix}T_{mix}+\frac{1}{2}{V_{mix}}^2\right)=\dot{m}_p\left(C_{p,p}T_{p2}+\frac{1}{2}{V_{p2}}^2\right)+\dot{m}_s\left(C_{p,s}T_{s2}+\frac{1}{2}{V_{s2}}^2\right)$$

$$T_{mix}=\frac{\dot{m}_p\left(C_{p,p}T_{p2}+\frac{1}{2}{M_{p2}}^2\gamma_p R_p T_{p2}\right)+\dot{m}_s\left(C_{p,s}T_{s2}+\frac{1}{2}{M_{s2}}^2\gamma_s R_s T_{s2}\right)}{\dot{m}_{mix}\left(C_{p,mix}+\frac{1}{2}{M_{mix}}^2\gamma_{mix}R_{mix}\right)} \quad (19)$$

It is assumed that a normal shock occurs in the constant-area section of the ejector after mixing of the motive and suction fluids has concluded. The static pressure and Mach number of the mixed flow following the normal shock can be calculated using Equation (20) and Equation (21), respectively.

$$P_3=P_{p2}\frac{2\gamma_{mix}{M_{mix}}^2-(\gamma_{mix}-1)}{\gamma_{mix}+1} \quad (20)$$

$$M_3=\sqrt{\frac{(\gamma_{mix}-1){M_{mix}}^2+2}{2\gamma_{mix}{M_{mix}}^2-(\gamma_{mix}-1)}} \quad (21)$$

The stagnation pressure at the exit plane of the ejector-diffuser is then calculated using isentropic relations. The analysis procedure for the new model is summarized in the flow chart given in Figure X.

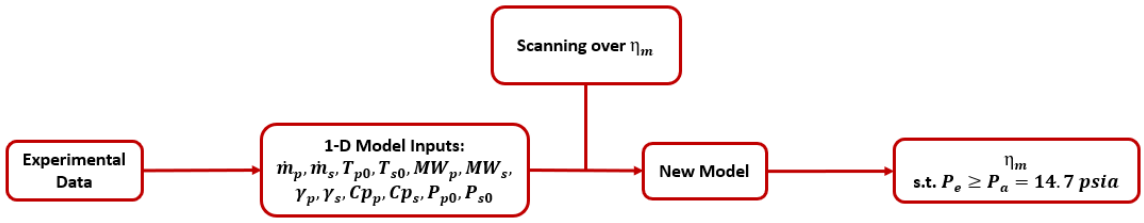

Figure 28: Flow chart describing analysis procedure for new model.

4.5 New Model: Single-Stage Ejector Characterization Results

Once the new model had been developed, the momentum coefficient was experimentally defined using the multi-nozzle test data collected earlier in the thesis. It is important that the successful coefficient curve be smooth and fittable. A three-dimensional graph showing the corrective coefficient value versus motive stagnation pressure and suction mass flow rate is given in Figure 29 for the original nozzle configuration.

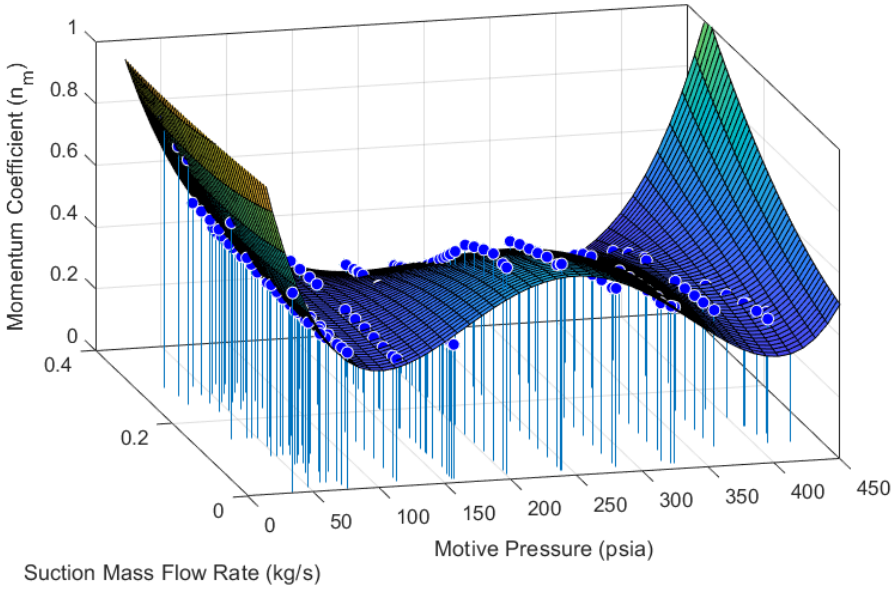

Figure 29: Graph of the momentum coefficient versus motive stagnation pressure and suction mass flow for original nozzle.

The corrective coefficient curve in Figure 29 is smooth and fittable, allowing for the designer to interpolate between experimental data points. This is a significant result, as this means that the model can be used to accurately predict the performance of the single-stage ejector system over its full operational range. Another interesting result present in Figure 29 is the peak in efficiency that occurs around 220 psia. This aligns closely with the motive design pressure for the single-stage ejector of 215 psia, and it implies that the new model accurately absorbs the turbulent mixing behavior into the corrective coefficient. This behavior was unseen in the Huang Model, implying that the model made assumptions which prevented the visualization of this result. The new model was also validated using the experimental data from the other two nozzle expansion ratios. The modeling results for these two experimental data sets are given in Figure 30 and Figure 31.

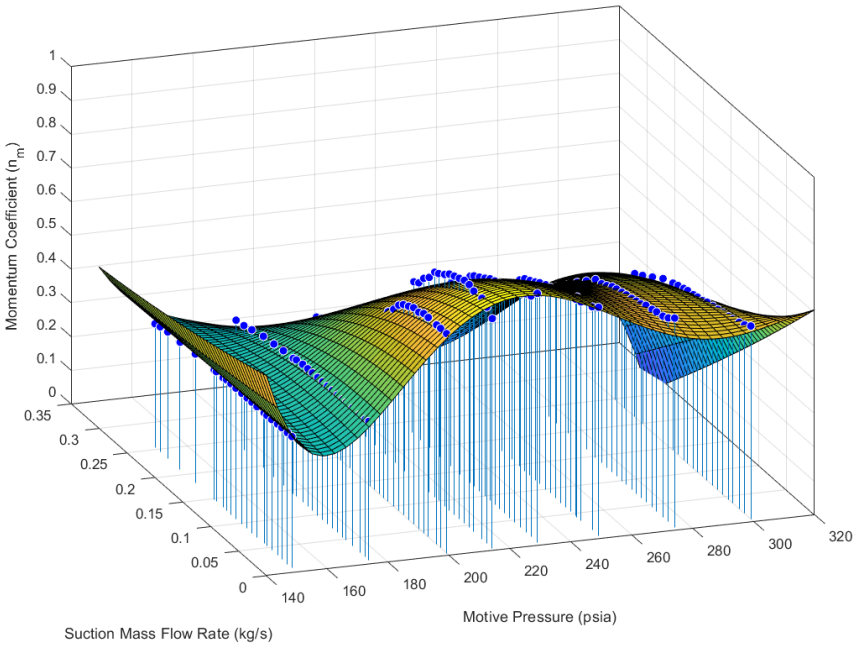

Figure 30: Graph relating the momentum coefficient, motive stagnation pressure, and suction mass flow for the 8.5 expansion ratio nozzle.

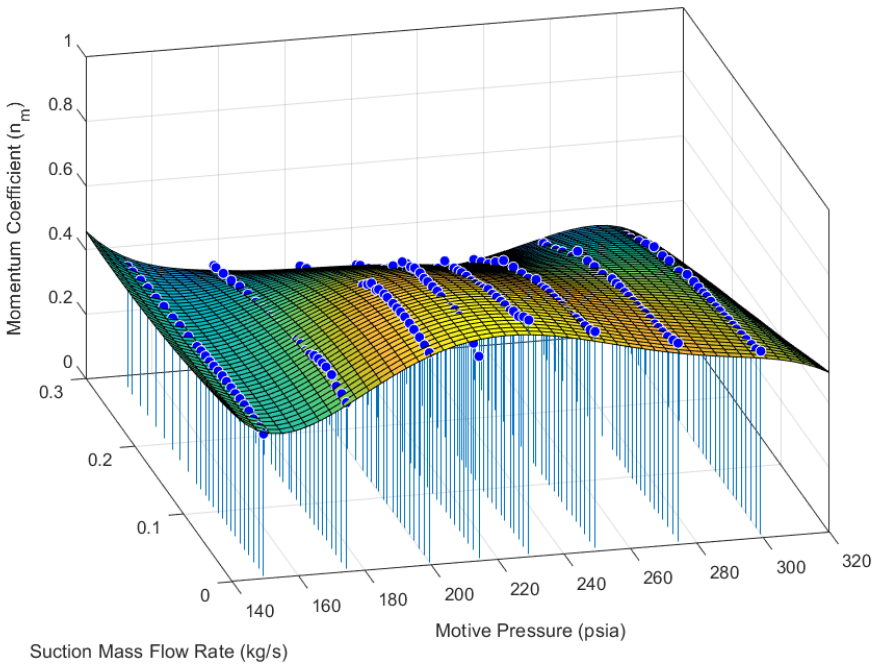

Figure 31: Graph relating the momentum coefficient, motive stagnation pressure, and suction mass flow for the 4.67 expansion ratio nozzle.

Again, the experimental data yields fittable curves for the 4.5 and 8.5 expansion ratio nozzles. It is shown that the model is robust enough to hold for multiple nozzle configurations. Once the new model was validated using facility nitrogen and air as the motive and suction sources, the model was then used to analyze the experimental results of a small solid rocket motor test within the altitude chamber at reduced pressure.

4.6 New Model: Single-Stage Ejector Solid Rocket Motor Test Results

For this experimental test, we used an Aerotech F50 motor. The manufacturer provides a thrust profile for the motor, which can be imported into Matlab to determine the mass flow profile for the motor. The full list of specifications relating to the Aerotech F50-9T motor is given in Table 7 below. The thrust curve for the F50 motor is given in Figure 32, and it is used to determine the average *Isp* for the solid rocket motor.

Table 7: Specifications for Aerotech F-50 solid rocket motor [32].

Parameter	Value
Total Propellant Mass (g)	54
Burn Duration (s)	1.4
Exit Temperature (K)	1500
Molecular Weight (g/mol)	23.04
Specific Heat Ratio	1.28

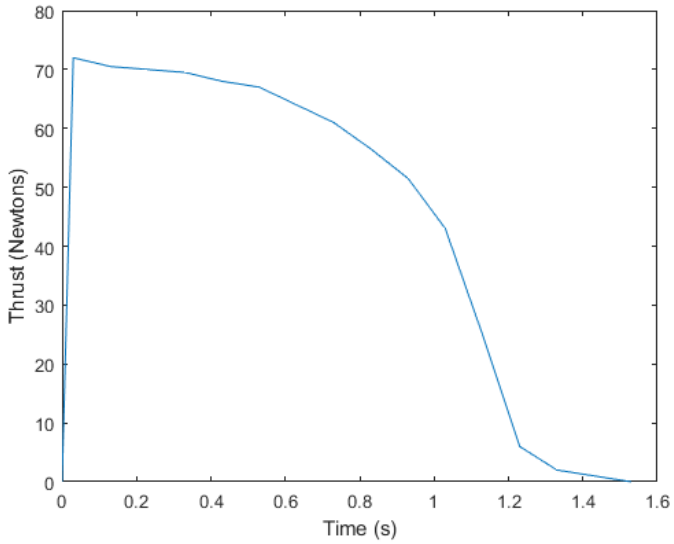

Figure 32: Graph of the thrust profile for the Aerotech F50-9T solid rocket motor [32].

The mass flow for a chosen average *Isp* can be calculated using the fundamental rocket thrust equation. An average *Isp* of 130 seconds was determined for the motor, as this yielded a total propellant mass flow of approximately 54 grams. This exhaust mass flow curve is calculated using the provided thrust curve and average specific impulse, and it is overlaid with the experimental suction stagnation pressure response in Figure 33.

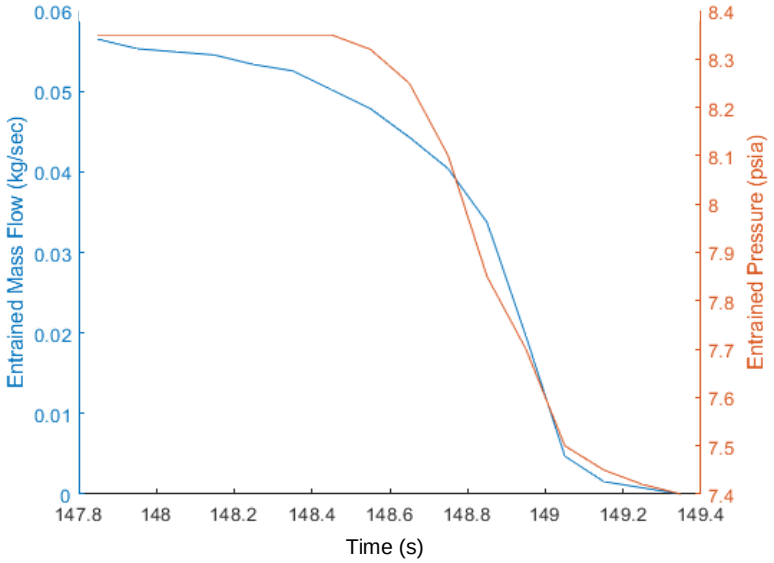

Figure 33: Relationship between exhaust mass flow and suction stagnation pressure.

It can be seen in Figure 33 that the measured suction static pressure corresponds closely with the estimated exhaust mass flow curve. This experimental test used air as the motive gas; the motive gas was maintained at a stagnation pressure of 167 psia for the full duration of testing. As the new model requires the ability to assume that the perfect gas law holds, it was necessary to treat the exhaust mass flow as an equivalent mass flow of nitrogen. Equation (22) is used to convert a given exhaust mass flow to an equivalent mass flow of nitrogen, and the derivation for this equation is given in NASA documentation [33].

$$\dot{m}_{N_2} = \dot{m}_s \frac{T_s}{T_{N_2}} \frac{MW_{N_2}}{MW_s} \tag{22}$$

Equation (22) allows the user to reference the original characterization data for either single-stage or two-stage ejector. Moreover, the equivalent nitrogen mass flow treatment in Equation (22) condenses three input parameters into a single parameter. In the future, this treatment could be used to simplify the process of optimizing an experimental rocket engine test by effectively reducing the number of free variables. Equation (22) is used with the new model to evaluate both rocket engine test series discussed within this thesis.

The new model is used to determine the momentum coefficient curve for the F50 motor test, assuming an equivalent mass flow of nitrogen. The graph shown in Figure 34 compares the calculated momentum coefficient values for the initial ejector performance data and the F50-9T motor data with equivalent nitrogen flow treatment.

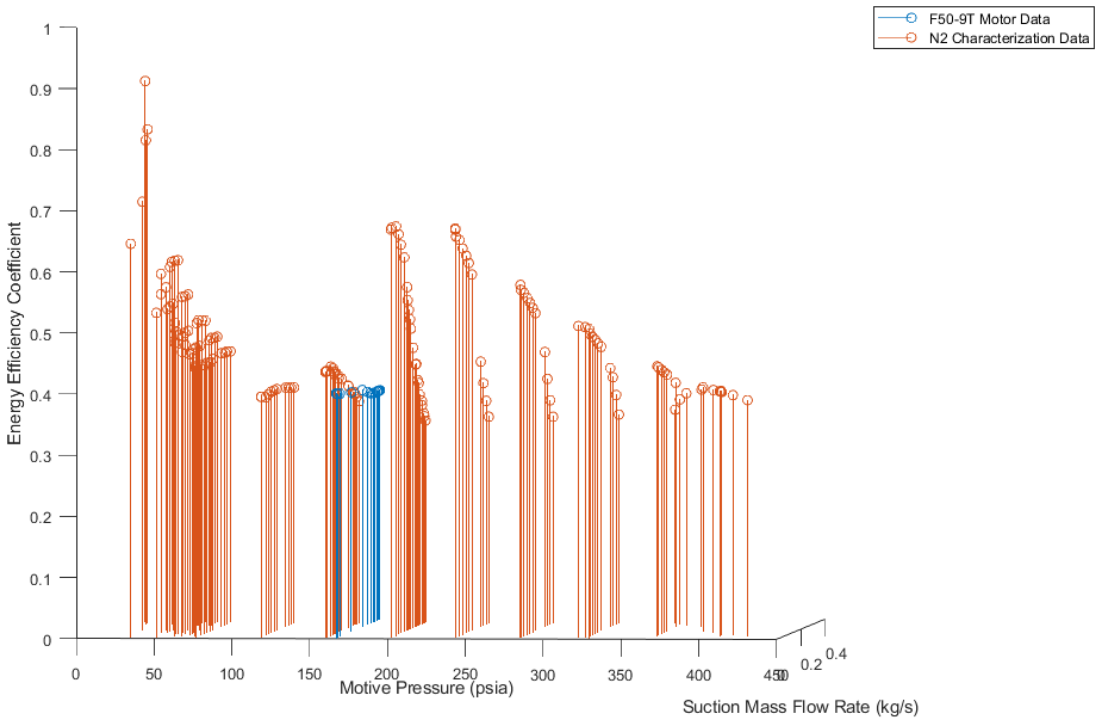

Figure 34: Graph showing overlay of equivalent nitrogen flow for F50-9T motor on performance characterization graph with original nozzle.

The graph in Figure 34 shows that treating the exhaust flow as an equivalent mass flow of nitrogen serves as a good preliminary estimate for ejector performance. It can be seen that the momentum coefficient is less responsive to the changing exhaust mass flow when compared with the characterization data, shown in orange. It is important to note that all of the motor test data was collected over the course of approximately 1.5 seconds. Furthermore, the actual mass flow of exhaust gases had to be estimated using motor performance data available online. Using the experimental data collected for a steady-state motor firing event would likely produce better agreement between the ejector characterization data and equivalent mass flow data. This ability to overlay ejector performance during rocket engine testing onto characterization data allows for prediction of ejector performance at testing conditions not experimentally defined previously. A

flow chart is provided in Figure 35 to show how this equivalent nitrogen treatment could be used to predict the performance of an ejector at new testing conditions.

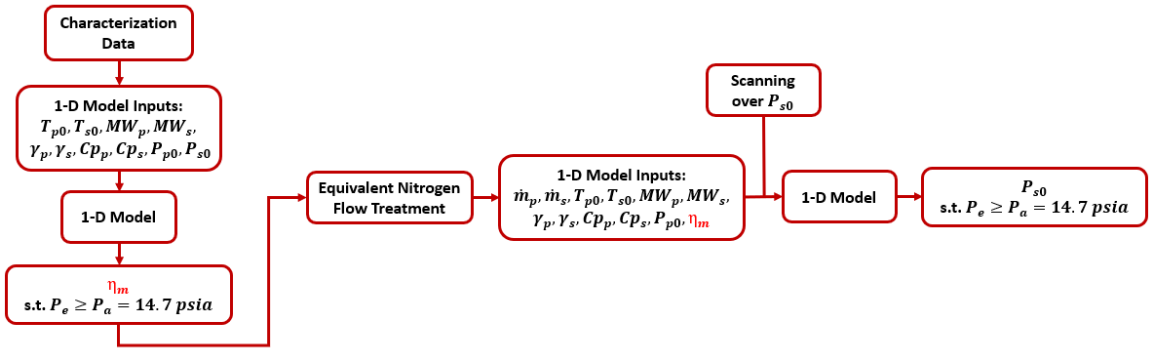

Figure 35: Flow chart displaying procedure for using characterization data and equivalent nitrogen flow treatment to extend model prediction capabilities.

As this result only shows that equivalent nitrogen mass flow treatment is viable at the operating conditions relevant to the F50-9T motor test, subsequent tests were performed using motors with different exhaust products and temperatures. These subsequent tests were also performed using the two-stage ejector system to maintain a reduced pressure environment within the altitude chamber. Modifications had to be made to the modeling script to allow for the characterization of a two-stage ejector system. This modification was relatively easy, as the inlet and exit conditions for each of the two ejector stages are known. As a result, each stage of the ejector system can be characterized separately.

4.7 New Model: Two-Stage Ejector Characterization Results

Before the next motor test could be analyzed using the new model, it was necessary to calibrate the model for the two-stage ejector system. An experimental test similar to that for the single-stage ejector system was performed to characterize the performance of the two-stage ejector over its relevant operational range. A CAD rendering of the two-stage ejector on loan from NASA Marshall is given in Figure 36. The relevant dimensions for the two-stage ejector system are given in Table 8.

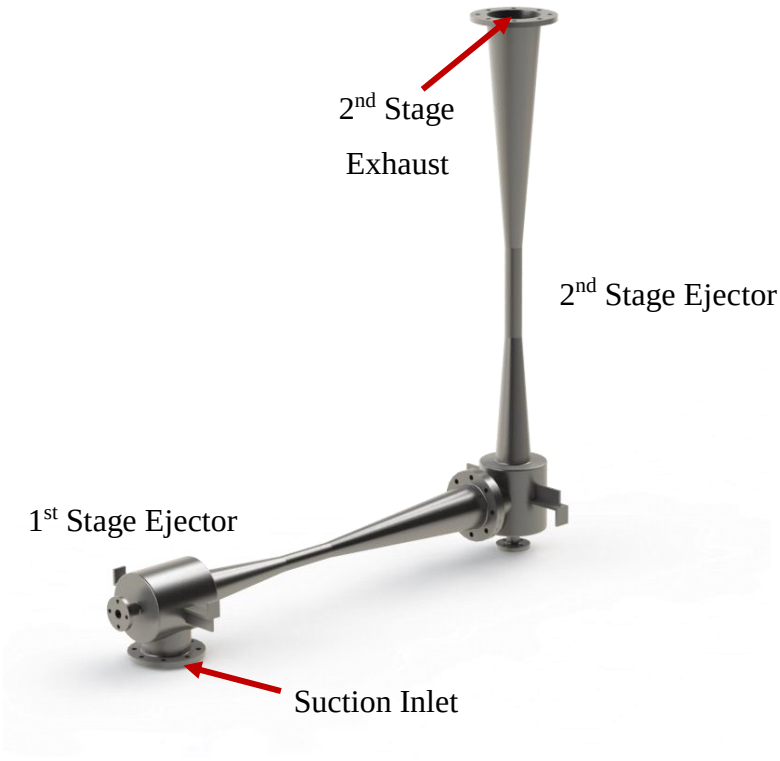

Figure 36: CAD rendering of the two-stage ejector system.

Table 8: Relevant values for the two-stage ejector system.

Parameter	**1st Stage Ejector**	**2nd Stage Ejector**
Suction Inlet Diameter (inch)	8.5	8.5
Motive Inlet Diameter (inch)	1.95	2.44
Pre-contraction Diameter (inch)	6.5	6.75
Constant Section Diameter (inch)	2.65	3
Diffuser Exit Diameter (inch)	8.5	10
Nozzle Throat Diameter (inch)	0.355	0.654
Nozzle Exit Diameter (inch)	0.5	1.25
Motive Mass Flow (lbm/s)	1.13	3.84
Contracting Length (inch)	20.25	24
Constant Section Length (inch)	11	17
Diffuser Length (inch)	37	42
Total Length (inch)	85.25	101
Maximum Rated Pressure (psia)	500	500

The two-stage ejector was only experimentally characterized at its full-flow state, with the 1st and 2nd stage motive stagnation pressure set at the maximum rated pressure of 500 psia. This is primarily because there are no plans to supply less than 500 psia to each of the two stage during the experimental testing of rocket engines within the altitude chamber. For this reason, all modeling results assume a constant motive stagnation pressure of 500 psia for each of the two stages. The experimentally measured relationship between 1st stage suction mass flow rate and 1st stage suction stagnation pressure is given in Figure 37.

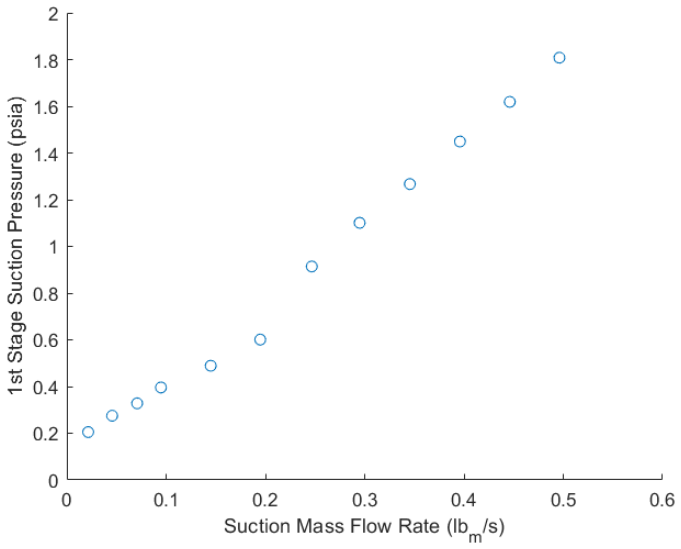

Figure 37: Relationship between 1st stage suction stagnation pressure and 1st stage suction mass flow rate for two-stage ejector system.

From the graph in Figure 37, there is an approximately quadratic relationship between the suction mass flow rate and suction stagnation pressure for the 1st stage ejector. Due to limitations on facility air usage, we were unable to characterize the full operational range of the two-stage ejector at its full-flow state. However, the presence of this approximately quadratic relationship could allow for extrapolation to higher suction mass flow rates, if the need arises.

The new model was then used to evaluate the experimental characterization data set for the two-stage ejector. The primary motivation for this modeling step was to ensure that the performance of the two-stage ejector could still be captured by the new model. The modeling

results for the experimental characterization of the two-stage ejector are given in Figure 38 and Figure 39.

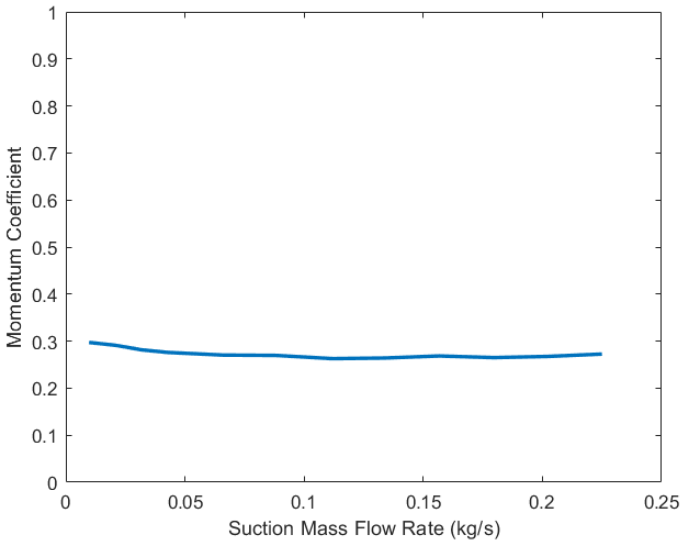

Figure 38: Graph showing momentum coefficient versus suction mass flow rate for first stage ejector.

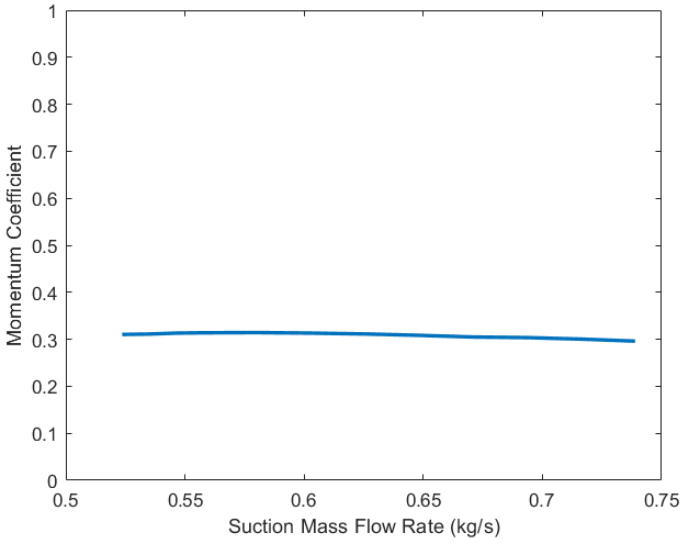

Figure 39: Graph showing momentum coefficient versus suction mass flow rate for second stage ejector.

From the graphs given in Figure 38 and Figure 39, it can be seen that all of the data points collected during the experimental characterization of the two-stage ejector are successfully defined using the new model. Moreover, each of the calculated momentum

coefficient curves are smooth and fittable, allowing for interpolation between experimental data points. It can also be seen in Figure 38 and Figure 39 that the momentum coefficient curves are relatively constant when compared to the modeling results for the single stage ejector, shown in Figure 29. This is due to the limited range of the characterization data for the two-stage ejector. Performing a more complete experimental characterization of the two-stage ejector over its full operational range would help further inform the modeling results, as well as avoid extrapolation.

4.8 New Model: Two-Stage Ejector 90 Newton Rocket Engine Test Results

Once it was determined that the new model could successfully capture the performance of the two-stage ejector, the new model was evaluated using rocket engine test data. The results of this modeling step would help to determine whether the new model is a viable predictive tool to be used with the two-stage ejector system. The relevant rocket exhaust flow conditions for the experimental test to be evaluated using the new model are given in the table below. While the exhaust temperature and molecular weight are approximately values, they are shown to be sufficient in proving the viability of the new model as a predictive tool for the testing of rocket engines using the two-stage ejector system.

Table 9: Relevant flow conditions for the rocket engine test using the two-stage ejector.

Parameter	**1st Stage Ejector**
Suction Temperature (K)	1000
Suction Molecular Weight (kg/kmol)	22
Suction Heat Capacity Ratio	1.3
Suction Mass Flow Rate (lb_m/s)	0.106
Suction Pressure (psia)	1.4

Similar to the treatment of the rocket exhaust mass flow in the single-stage modeling, the rocket exhaust mass flow is converted into an equivalent mass flow of nitrogen. The calculated momentum coefficient values for the two ejector stages resulting from this equivalent nitrogen mass flow treatment is then overlaid on the momentum coefficient curves derived from the experimental characterization data. This visual comparison between the momentum coefficient values for the equivalent nitrogen mass flow treatment and experimental characterization data is presented in Figure 40 and Figure 41.

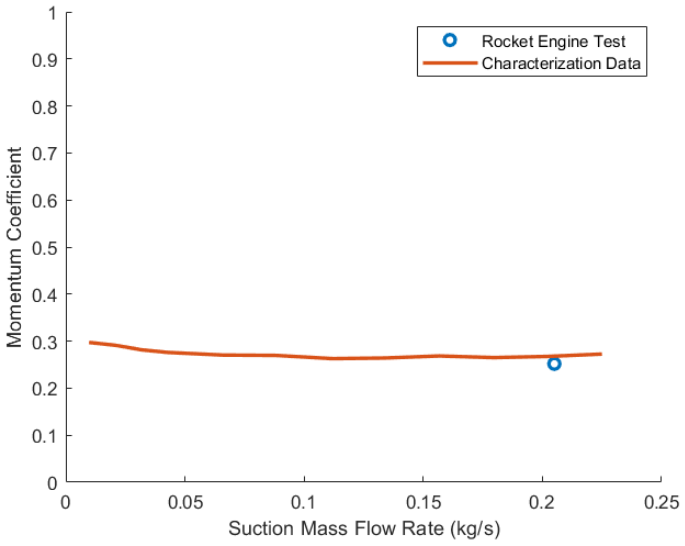

Figure 40: Comparison on momentum coefficient value between characterization data and equivalent nitrogen flow for rocket engine test for 1st stage ejector.

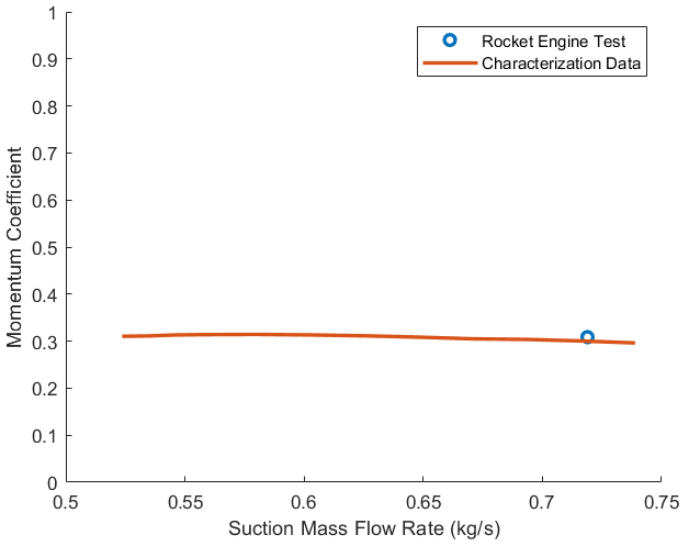

Figure 41: Comparison on momentum coefficient value between characterization data and equivalent nitrogen flow for rocket engine test for 2nd stage ejector.

From the results given in Figure 40 and Figure 41, it can be seen that there is generally good agreement between the ejector characterization data and equivalent nitrogen mass flow

treatment of the rocket exhaust. In this way, it is shown that the equivalent nitrogen mass flow methodology can be implemented with reasonable accuracy to predict the performance of both the single-stage and two-stage ejector systems during the testing of rocket engines at reduced pressure.

4.9 Graphical User Interface: Overview

In an effort to improve accessibility, a simple graphical user interface (GUI) was created to allow the user to input suction and motive flow conditions relevant to their desired testing conditions for either the single-stage and two-stage ejector system. There also exists the option to input characterization data for alternate ejector geometries, further extending the predictive capabilities of the new 1-D model. The general procedure for using the GUI is provided below for reference.

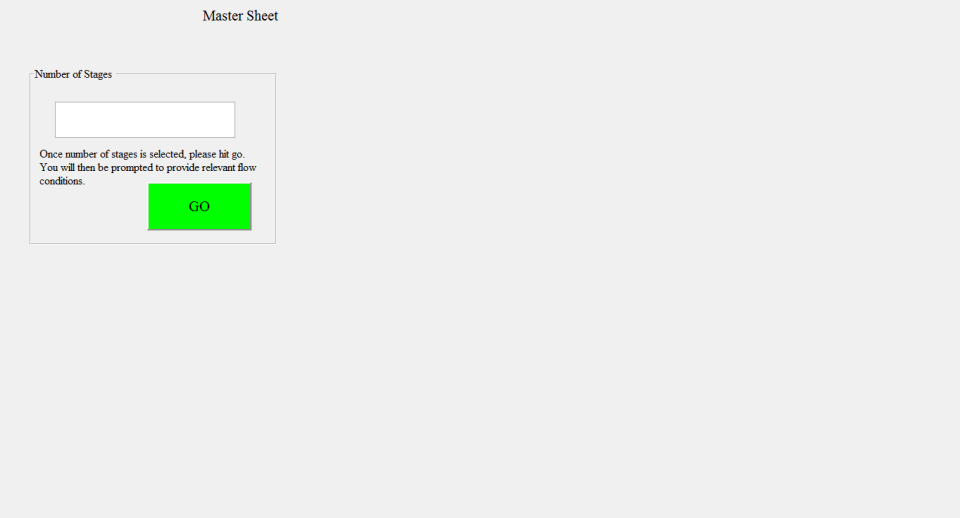

Figure 42: Screen of model GUI used to specify the number of ejector stages used.

This page of the GUI is relatively straightforward, requiring only the number of desired number of ejector stages for the evaluation. Currently, only single-stage and two-stage ejectors are available. This GUI also only treats multi-stage ejector configured in series. This is because the GUI is set up to handle only ejector for which we already have characterization data.

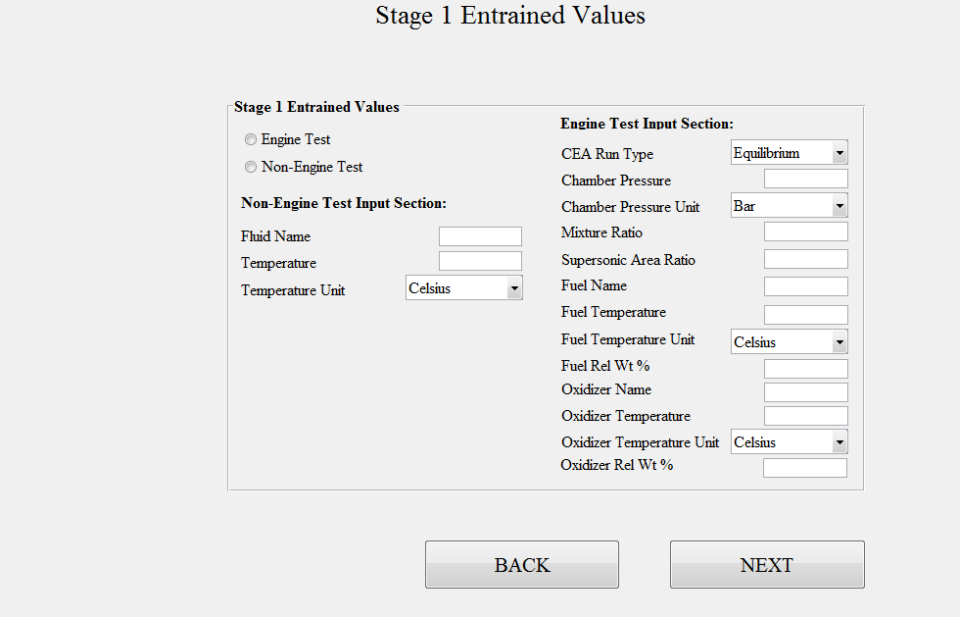

Figure 43: Screen of model GUI used to specify 1st stage suction flow values.

Figure 43 is used to specify whether or not you are evaluating a rocket engine test. After choosing one of the two options, you can then specify all of the relevant entrained flow conditions. This section of the GUI also has a built-in function which can run Chemical Equilibrium with Application (CEA). After specifying all of the relevant entrained conditions, Figure 44 is used to define the 1st stage motive flow conditions and ejector dimensions.

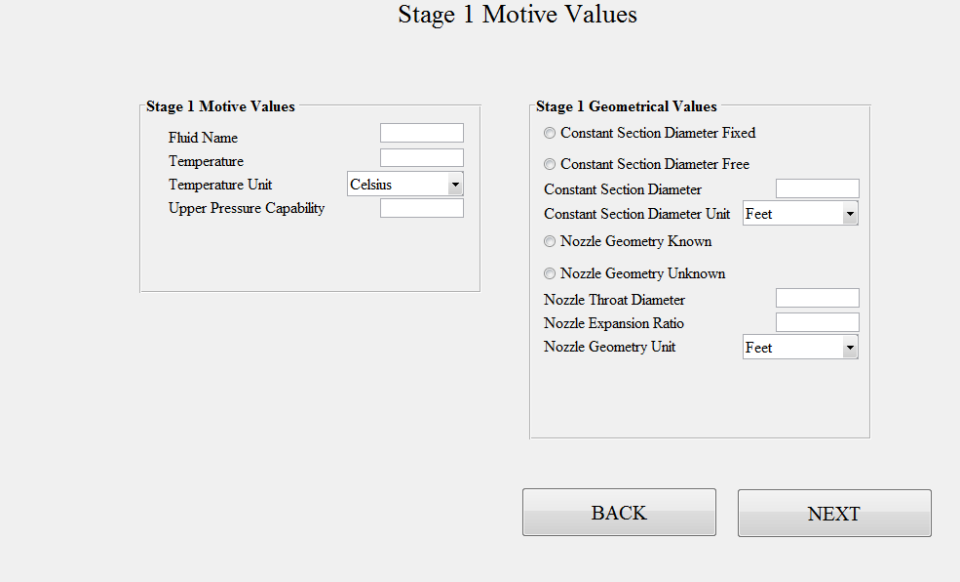

Figure 44: Screen of model GUI used to specify 1st stage motive flow values.

The section of the GUI given in Figure 44 is used to specify the motive conditions and geometrical dimensions relevant the 1st stage ejector. This includes the constant section diameter, pre-contraction diameter, and nozzle geometry. If a two-stage system was specified in Figure 42, then Figure 45 is displayed.

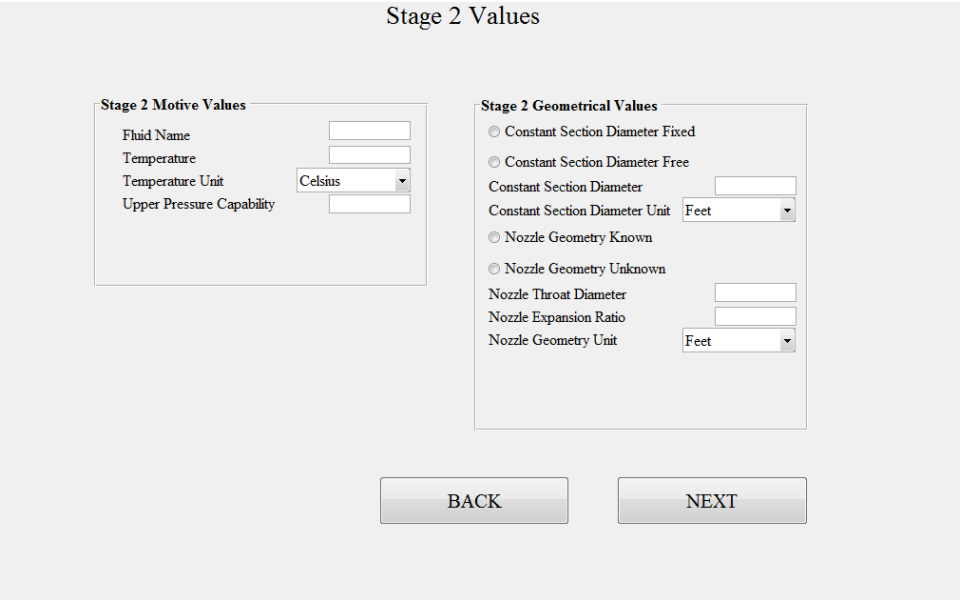

Figure 45: Screen of model GUI used to specify 2nd stage motive flow values.

The inputs for the 2nd stage motive conditions and geometrical dimensions are identical to those given in Figure 44. Once this section is completed, the model can be evaluated for what ejector options were chosen in the GUI. This GUI serves as a preliminary tool to meet basic ejector modeling needs. However, the complexity of this GUI, as well as the complexity of the new model, can be revised as necessary. In this way, the new model and GUI serve as a foundation on which to build increasingly accurate modeling architectures.

While not modeled within the context of this thesis, the new hybrid rocket engine designed as part of a collaborative effort between Zucrow Labs and JPL is scheduled to test in the altitude chamber in late July of this year. This will be the first major testing campaign that occurs within the altitude chamber following the completion of this thesis. As the new JPL motor is optimized for 90 lbf at 100,000 ft, it is essential that the performance of the two-stage ejector in ZL3 be well understood. The design of the new JPL motor began in mid-January of this year, and it is discussed in detail in the following section.

5 JPL MOTOR DESIGN

Over the last five years, Dr. Pourpoint's research group has collaborated with JPL to characterize the performance of a hybrid motor design, which could potentially be used for the Mars Ascent Vehicle (MAV) mission. One of the major constraining factors in propellant choice is the ambient temperature on the surface of Mars, roughly -55°C. This motivated the use of a hybrid propulsion architecture with a solid fuel and an oxidizer with a freezing point well below this average temperature. The oxidizer of interest in the project was Mixed Oxides of Nitrogen (MON). There are two main constituents of MON: nitric oxide (NO) and nitrogen tetroxide (N_2O_4). While nitrogen tetroxide has a relatively high freezing point of around -10°C, this freezing point can be depressed by introducing nitric oxide. Mixing nitric oxide with nitrogen tetroxide acts to lower the overall freezing point of the mixture, making this mixture a viable propellant candidate for use in the MAV mission.

The concentration of nitric oxide introduced into nitrogen tetroxide is measured on a mass basis, and is denoted in the number following MON. For example, a mixture of Nitrogen Tetroxide and 25% by weight of Nitric Oxide is denoted as MON-25. It has been shown in literature than MON-25 has a freezing point around -55°C [34]. For this reason, MON-25 has been pursued as a potential propellant to be used on the Mars Ascent Vehicle (MAV) project in collaboration with JPL. Though characterization of the hybrid configuration was initially performed at sea-level conditions [35], it is more representative to test the hybrid motor in a reduce pressure environment corresponding more closely to the Martian atmosphere.

A new motor design is proposed for testing at reduced pressures within the altitude chamber to closely represent atmospheric conditions experienced on Mars. The functional and performance requirements for the new JPL motor are given on the next page.

Functional Requirements:

- Ease of cleaning/disassembly
- Design failure model for safety
- 2 to 5 second firing duration
- Combustion chamber pressure/temperature measurement capability
- Expendable components of standard dimensions

Performance Requirements:

- 600 psia over-pressurization threshold with safety factor > 3 for all components
    - 200-300 nominal operating pressure
- 0.1 lb_m/s MON flow rate
- ~0.01 lb_m/s liquid igniter/N_2 flow rate prior to steady operation
- 90 lb_f thrust

While these functional and performance requirements acted to guide much of the design process, there were additional factors which served to further constrain the potential design space. There are unique challenges inherent to the testing of a motor in an altitude chamber at reduced pressure. First, there is a limited number of flanges on the altitude chamber. Many of these flanges are already used for optical access for recording tests and optical measurement of the flow, and for thermocouple and pressure transducer feedthroughs. For this reason, it is beneficial to design a motor which minimizes the number of necessary feedthroughs outside of basic pressure and temperature instrumentation. MON-25 is extremely corrosive, requiring the motor to be made of materials which are compatible with this oxidizer. 316 stainless steel has been shown to be chemically compatible with MON-25, and it is thus chosen to be the material for the main body of the motor. A final implicit requirement was that the new JPL motor had to be able to accept the existing grain geometry used for atmospheric tests.

The design of a new system capability is inherently iterative in nature, with all associated elements being subject to change over time. These changes are reflected in both the system design and the overarching design requirements which guide the project. One should not expect to arrive at the optimal solution with the first design concept. Instead, the initial conceptual design serves only as a benchmark by which to compare subsequent designs. With each iteration

of design, the team slowly converges on the optimal solution by resolving shortcomings present in the previous design iterations. It is the task of the designer to efficiently utilize all relevant expertise to ensure that the design process continues to converge on the optimal solution.

The design decisions made in this project were highly transparent and involved all relevant faculty and staff at the Zucrow Labs and engineers at the National Aeronautics and Space Administration (NASA) and the Jet Propulsion Laboratory (JPL). All significant changes made to the design were presented to NASA/JPL, and appropriate revisions were determined and implemented. Though there exist roughly eight iterations for the design of the new JPL motor for reduced-pressure testing, only the final iteration is discussed within the context of this thesis. There are five major components relating to the design of the JPL motor: CAD design; FEA analysis and stress analysis; thermal expansion analysis; thermal stress analysis; and shear pin design. Each of these five components of the design process will be detailed in this section of the thesis.

The first step is to create a three-dimensional model, which helps to visually determine the impact of decisions made throughout the design process. This is accomplished using Computer Aided Design (CAD); Solidworks 2019 is used to create all of the CAD models presented within this thesis. Some aspects of the design were fixed or constrained at the beginning of the design process. For example, the combustor had to accommodate the same grain configuration used in the previous JPL motor for atmospheric performance characterization. The new combustor also had to use the same spray injector present in the atmospheric testing campaign, as the flow behavior and performance of the old spray injector was already experimentally validated.

It is also important to design a motor that minimizes the probability of a catastrophic over-pressurization event occurring. There are multiple mechanisms by which this over-pressurization can occur, including blockage of the nozzle throat, high ignition delay, and de-bonding of the fuel grain within the combustion chamber. The concept of over-pressurization varies from motor to motor and defines the upper pressure threshold that is tolerable for the given motor configuration. If the pressure within the motor rises above this upper threshold, there must exist a reliable mechanism to quickly relieve pressure. Otherwise, there is a high likelihood that the entire motor will be lost.

In design, it is often beneficial to define a factor of safety for each component of the motor. A factor of safety is the ratio of the maximum stress experienced to the maximum stress that the

component can withstand. The maximum allowable stress for a given component depends on the component geometry, as well as its material composition. The desired factor of safety for a system can vary widely depending on the risk threshold for the mission or application. For instance, a factor of safety of 1.4 to 1.5 is often desirable for flight-ready systems [36]. Flight-ready systems are generally designed with a lower factor of safety to optimize operational performance. Increasing the amount of stress that a component can withstand often means increasing wall thicknesses or using exotic materials. These two factors serve to increase the cost of the final flight system, and also potentially reduce the relative performance of the system through an increase in overall weight. For non-flight systems, it is often advantageous to have a higher safety factor. The increase in weight and cost is less significant for non-flight systems, and thus priority can shift toward minimizing associated operational risks. It will be shown that each component of the motor designed within the context of this thesis has a factor of safety of at least 2, aside from the nozzle insert. The reasoning for the slightly lower factor of safety for the nozzle insert will be explained later in the thesis.

The CAD model is composed of seven major components: injector housing, injector flange, main pipe section, main pipe partial, nozzle housing and expansion section, nozzle insert, and shear pins. Each of these components will first be discussed in detail individually. The inter-relations between these components will then be discussed, culminating in the final discussion of the motor as a whole. There are also smaller supporting components associated with the motor design which will be discussed as appropriate.

5.1 Injector Assembly Design

The injector housing is the upstream-most component of the motor and supports oxidizer, igniter, and nitrogen injection into the combustion chamber of the motor. A CAD model depicting the overall geometry of the injector housing is given in Figure 46 to support the proceeding discussions.

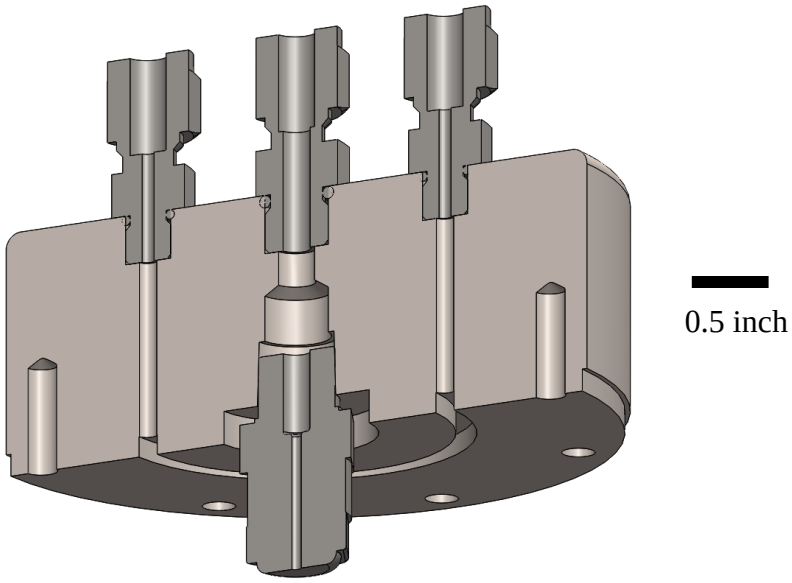

Figure 46: CAD model cutaway view showing all major design components of injector housing, as well as the full-cone spray injector.

As can be seen in Figure 46, there are three main ports which support the injection of three different fluids into the motor. The larger ¼ inch diameter port in the center supports the main flow of MON-25, and feeds into a full-cone spray injector. There are two smaller 1/8 inch ports which feed an annular injection ring; one of these ports is for the nitrogen purge, and the other is for the igniter liquid. As the fuel grain includes moisture sensitive additives, it is necessary to continuously purge the grain with nitrogen before and after firing. Igniter injection is included to help ensure successful ignition in the new reduced-pressure testing environment within the altitude chamber. The full injector assembly, which includes both the injector housing and injector flange, is shown in Figure 47.

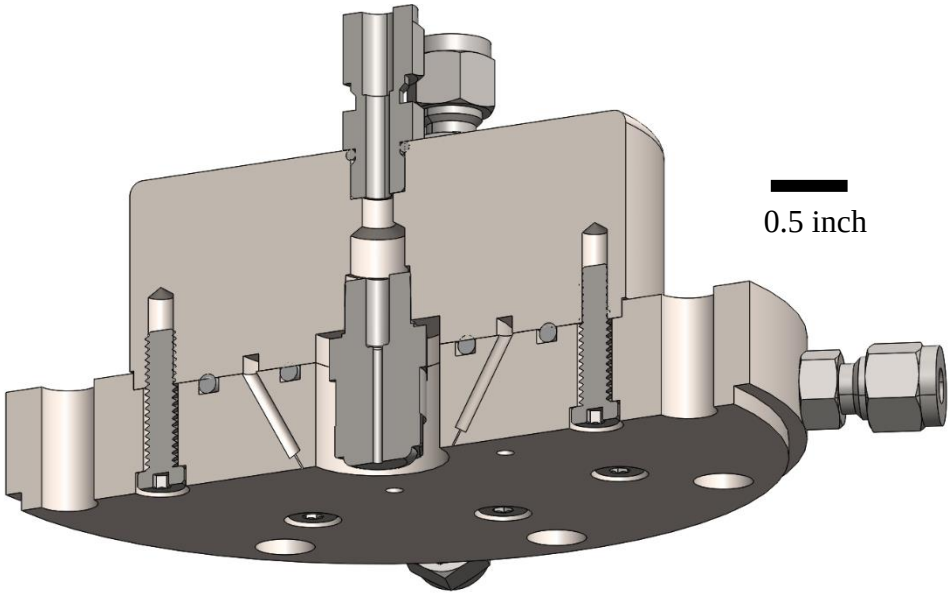

Figure 47: CAD model depicting full injector assembly.

In Figure 47, the injection holes in the injector flange are clocked 90° from the nitrogen and igniter ports in the injector housing. The design of these injection holes is discussed later in this section of the thesis. This 90° clocking ensures that each of the two injection holes receives an equal flow rate of both nitrogen and igniter fluid from the upstream injection ports. The injector housing and injector flange are machined as two separate parts to aid in machinability, adaptability, and ease of cleaning. If an annular ring were not included in the design, each injection hole would have to be fed by individual ports in the injector housing. While this is not necessarily an issue with only two injection holes, it would quickly become problematic as the number of injection holes increased. As the injector assembly is composed of two parts, a change in injection hole configuration only requires redesigning the injector flange. This saves in long term design/machining costs, and also allows for ease of access for cleaning the annular ring.

In addition to supporting the injection of relevant testing fluids into the combustion chamber, the injector flange also supports the measurement of the combustion chamber pressure and temperature. There are four 1/8 inch instrumentation ports machined into the injector flange; these are shown in Figure 48 for reference.

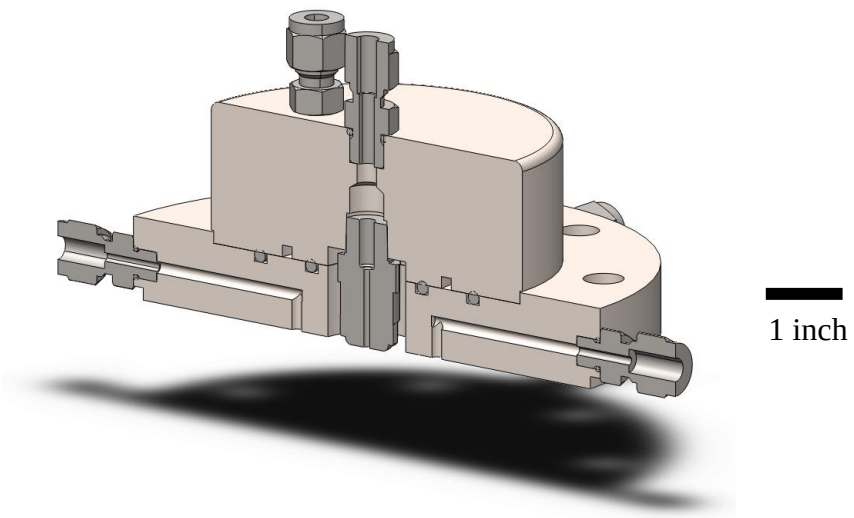

Figure 48: CAD cutaway view showing instrumentation ports in the injector flange used for combustion chamber pressure and temperature measurement.

Dividing the injector assembly into two components necessitated the addition of two sealing O-rings between the injector flange and injector housing. The inner O-ring acts to prevent the mixing of MON-25 and the igniter fluid. The outer O-ring is designed to prevent the igniter fluid, as well as combustion gases, from leaking into the altitude chamber. The sizing of these two O-ring grooves, and all other O-ring grooves on the motor, was completed using the Parker O-ring handbook [37]. It was essential that the O-rings were compatible with MON-25, as they would be exposed to the main oxidizer flow during testing. Polytetrafluoroethylene (PTFE) is known to be compatible with MON-25, and thus PTFE was chosen as the O-ring material.

In the design requirements, a 10% mass flow of igniter fluid relative to the main MON-25 flow is desired. As the main MON-25 mass flow is roughly 0.1 lb_m/s, the injection holes are design to support a total igniter flow rate of roughly 0.01 lb_m/s. It is also important to have an adequate pressure drop across the injection holes, in order to prevent the flow of combustion gases back into the annular ring. For our implementation, a desired pressure drop of roughly 100 psia was defined. Equation (23) is used to determine the size and number of injection holes necessary to achieve this desired mass flow and pressure drop.

$$\Delta P = \frac{1}{2\rho}\left(\frac{\dot{m}}{NC_d A}\right)^2 \tag{23}$$

A 114 psia theoretical pressure drop was achieved using two 0.012 inch diameter injection holes. These small diameter holes were produced using EDM drilling methods and satisfied both our mass flow and pressure drop criteria.

A flange outer diameter of 6 inches and a flange thickness of 0.75 inch was chosen for each of the four flanges on the motor. The outer diameter for each flange was only constrained by the geometry of the motor components. It was desirable to minimize the outer diameter of the flanges, as this would equate to less raw material and machining cost. However, there also had to be enough space for the bolts to slide into the bolt holes. The main driving constraint for the minimum diameter of the flanges was the injector housing. The outer diameter of the injector housing is roughly 4 inches, approximately 1 inch larger than the outer diameter for all other motor components. A flange outer diameter of 6 inches ensured that there were no interference issues between the connecting bolts and the body of the motor. Equation (24) is used to validate the thickness for all flanges on the motor.

$$\sigma = P\left(\frac{D_{flange}}{T_{flange}}\right)^2 \tag{24}$$

A safety factor is defined as the ratio of the calculated stress in the component to the yield strength of the material. As mentioned in the performance requirements provided by JPL, our factor of safety is defined relative to a chamber pressure of 600 psia. This is much higher than the chamber pressure expected during nominal motor operation, and it represents the critical point at which the pressure within the combustion chamber must be relieved. A relief mechanism in the form of a free floating nozzle insert held in place by graphite shear pins is included in the motor design to ensure that the pressure within the combustion chamber of the motor does not rise above this 600 psia threshold. As a result, all of the safety factors defined in the design process denote the ratio of the stress experienced in the component for a chamber pressure of 600 psia to the maximum allowable stress for that part. For a chamber pressure of 600 psia, the maximum stress in the motor flanges given a flange thickness of ¾ inch was 9,700 psi. As the yield strength of 316 Stainless Steel is approximately 30,000 psi, this yielded a safety factor of over 3 for the thickness of the flanges used on the motor.

5.2 Main Pipe Section/Partial Design

The next step was to determine the necessary wall thickness for the main pipe section and main pipe partial. This was accomplished first using basic hoop stress calculations. There are two main regimes for calculating hoop stress: thin-walled and thick-walled. The thin-walled assumption is appropriate if the ratio of the outer diameter to inner diameter is less than 1.1, while the thick-walled assumption is appropriate if this ratio is greater than 1.5. The main pipe section has a ratio value of approximately 1.33. The safety factor for the main pipe section and main pipe partial are calculated using both assumptions, and the results of these two assumptions are compared. Equation (25) defines the stress in the pipe using the thin-walled assumption, and Equation (26) defines the stress in the pipe using the thick-walled assumption.

$$\sigma = \frac{0.5PD_{in}}{t} \tag{25}$$

$$\sigma = P\frac{{D_{out}}^2 + {D_{in}}^2}{{D_{out}}^2 - {D_{in}}^2} \tag{26}$$

The calculated stress using the thin-walled assumption was roughly 2,800 psi, and the calculated stress using the thick-walled assumption was roughly 3,100 psi. In our case, 316 stainless steel was utilized as the material for the main pipe section and main pipe partial. This yields a safety factor of 11 using the thin-walled assumption and 10 using the thick-walled assumption. This is more than sufficient for our purposes, and thus we move on to the next steps in the design process.

It was determined that the center body of the motor, which holds the phenolic case and fuel grain, needed to be modular, allowing for different grain configurations to be evaluated with various post-combustion chamber lengths. For this reason, the center body of the motor was divided into two sections: main pipe section and main pipe partial. By removing main pipe partial, and cutting a shorter phenolic case length, the motor could be tested with a shortened post-combustion chamber. The two proposed configurations are given in Figure 49 below, with and without main pipe partial.

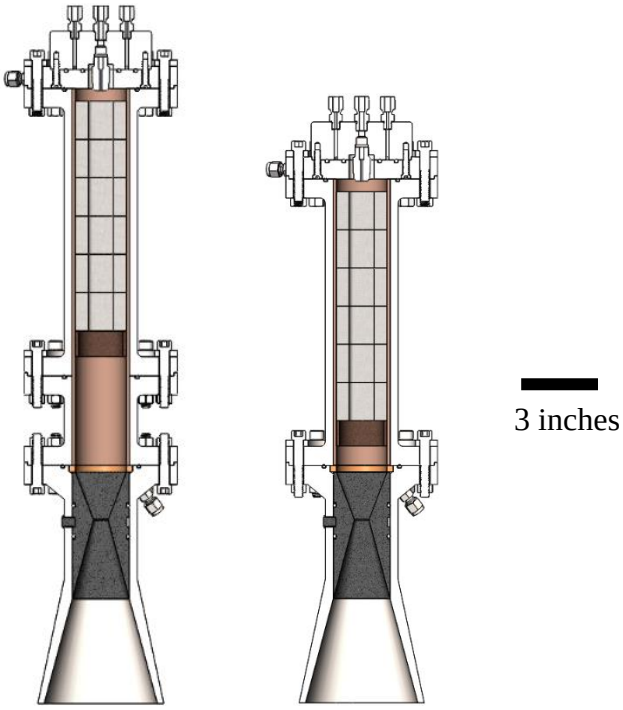

Figure 49: CAD cutaway view showing the normal and shortened motor configurations.

One important step in the design process is to determine the bolt sizes necessary to prevent point failures at flanged connections. Both tensile stress and bolt shear stress calculations were performed for the bolted connections between the injector housing and injector flange, as well as between the injector flange and main pipe section. While there are two other flanged connections on the motor (main pipe section – main pipe partial and main pipe partial – nozzle housing/expansion section), these use the same flanges and bolted connections as between the injector flange and main pipe section. A factor of safety can again be defined here based on the tensile and shear strength of the material, Grade-8 steel in this case for all of the bolts. Again, a pressure of 600 psia is used in this calculation to represent the maximum pressure threshold for the motor. Equation (27) is used to calculate bolt shear stress, and Equation (28) is used to calculate bolt tensile stress. There is one term in Equation (28), called the bolt tensile area, which must be calculated separately using Equation (29).

$$\sigma = \frac{P(D_o{}^2)}{L_e(E)(N)} \tag{27}$$

$$\sigma = \frac{\pi/_4 PD_o{}^2}{A_t N} \tag{28}$$

$$A_t = \frac{\pi}{4}(D_m - 0.938194p)^2 \tag{29}$$

It was determined that eight ¼”-20 bolts were sufficient to connect the injector housing and injector flange. This number and size of bolts yields a factor of safety of 9 for bolt tensile shear, and a factor of safety of 8 for bolt thread shear. 3/8”-16 bolts were chosen for the three main flanged connections on the motor. This yields a factor of safety of 22 for bolt tensile shear, and a factor of safety of 23 for bolt thread shear. Once the bolt sizes and numbers are determined, we move onto the design of the nozzle housing/expansion section.

5.3 Nozzle Assembly Design

The nozzle housing/expansion section, and the nozzle insert, were designed simultaneously. A CAD model showing the final geometry of the nozzle housing/expansion section and nozzle insert is given in Figure 50.

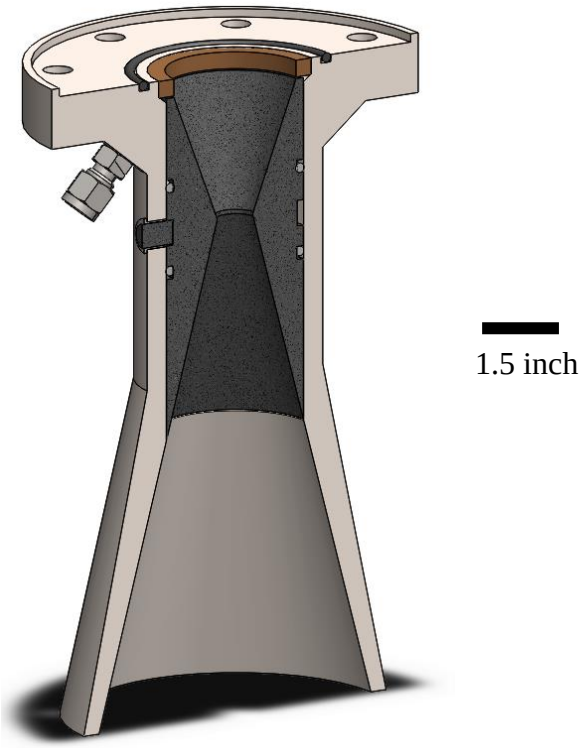

Figure 50: CAD cutaway view showing the major design elements associated with the overall nozzle assembly.

The nozzle insert is design to be our pressure-relief mechanism in the event of over-pressurization. If the chamber pressure were to exceed the maximum threshold of 600 psi, the shear pins would fail, ejecting the nozzle insert out of the bottom of the motor. For this reason, it was essential that none of the downstream inner diameters were smaller than the outer diameter of the nozzle insert. The inner diameter of the upstream side of the nozzle insert was set by the inner diameter of the phenolic case holding the fuel grain. This helped to ensure that the flow was not disturbed while traveling from the combustion chamber into the throat of the nozzle insert. The throat diameter for the nozzle insert was designed to match that of the existing JPL motor, so that the exhaust mass flow and thrust values for reduced pressure testing would be comparable to those from the atmospheric tests. It was important to keep as much of the inner geometry consistent with the old JPL motor as possible. This would allow for the lessons learned in atmospheric testing to be applicable in the testing of the new motor. The expansion ratio of the nozzle housing/expansion section of the motor was sized such that the exhaust gases at the exit plane of the nozzle would be slightly under-expanded relative to a simulated altitude of

100,000 ft. This would allow the exhaust gases to continue expanding, eventually impinging with the walls of the downstream supersonic diffuser inlet. For a nozzle throat diameter of 0.6 inch an exit diameter of 4.45 inches was chosen to yield an exit pressure of approximately 0.25 psia. This theoretical exit pressure was determined using CEA with propellant and chamber values relevant to the testing of the new JPL motor, and it represents an equivalent altitude of approximately 91,000 ft.

5.4 Nozzle Assembly Thermal Analysis

An axisymmetric thermal analysis was performed for the nozzle housing/expansion section, phenolic ring, and nozzle insert. The heat transfer was determined using results from CEA and the Dittus-Boelter Correlation, which is given in Equation (30) for reference.

$$\mathrm{Nu_D} = 0.023\mathrm{Re}^{0.8}\mathrm{Pr}^{0.4} \tag{30}$$

The heat transfer was determined at three discrete locations within the model geometry: combustion chamber, nozzle throat, and exit of the expansion section. The heat transfer values were then interpolated between these three points to define the heat transfer distribution along the entire nozzle geometry. The thermal analysis was performed for a 2 second test, as well as for a 5 second test. While most of the atmospheric tests were around 2 seconds in length, it was essential to design the motor to support whatever testing conditions might arise in the future. The thermal analysis results for the 2 and 5 second firing durations are given in Figure 51.

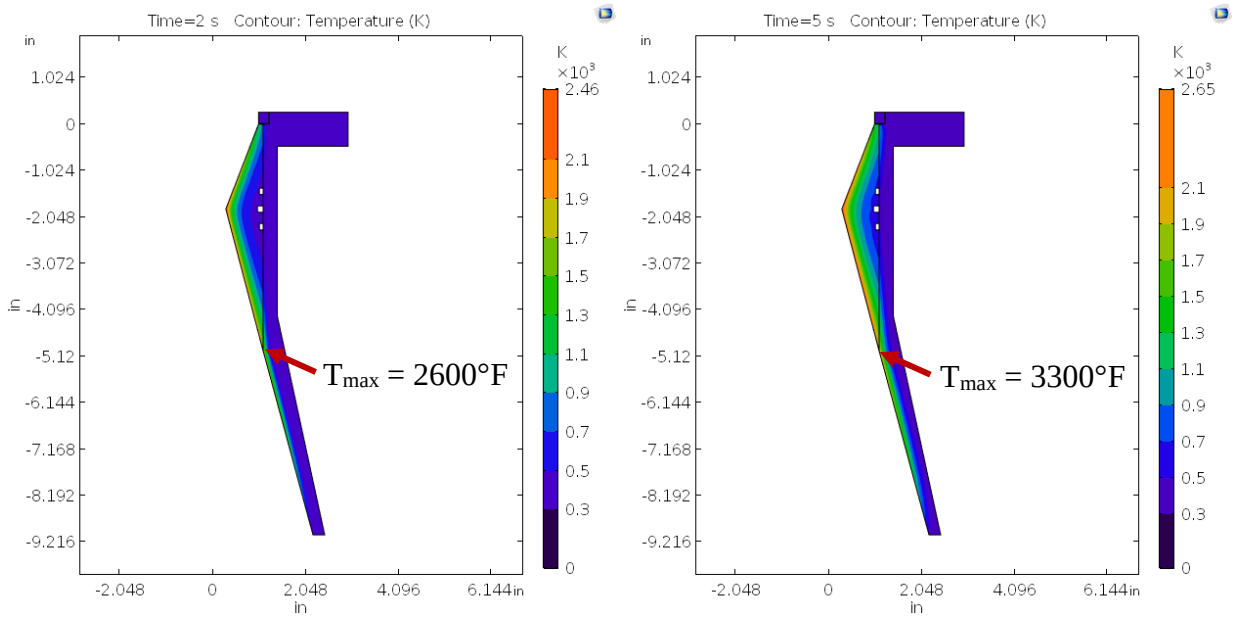

Figure 51: COMSOL thermal analysis result for 2 and 5 second firing durations without TBC.

From the results in Figure 51, it became clear that the proposed motor configuration would not survive without the addition of a thermal barrier coating. The melting temperature of 316 stainless steel is approximately 2550°F, while the maximum temperature experienced during even the 2 second test is 2600°F. A thermal barrier coating (TBC), made of Zirconia and an 8% weighting of Yttria-Oxide, was included in an updated thermal analysis. The thickness of each portion of the thermal barrier coating is given in Figure 52.

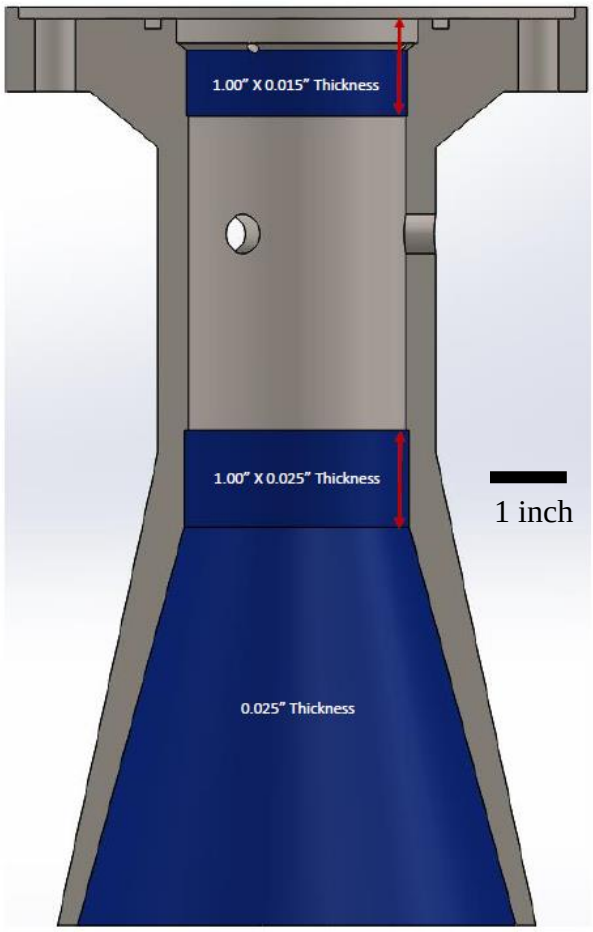

Figure 52: Thicknesses and locations of TBC application.

After adding the thermal barrier coating in the necessary locations, the thermal analysis was once again performed. The results for the 2 second and 5 second firing durations with thermal barrier coating included are given in Figure 53.

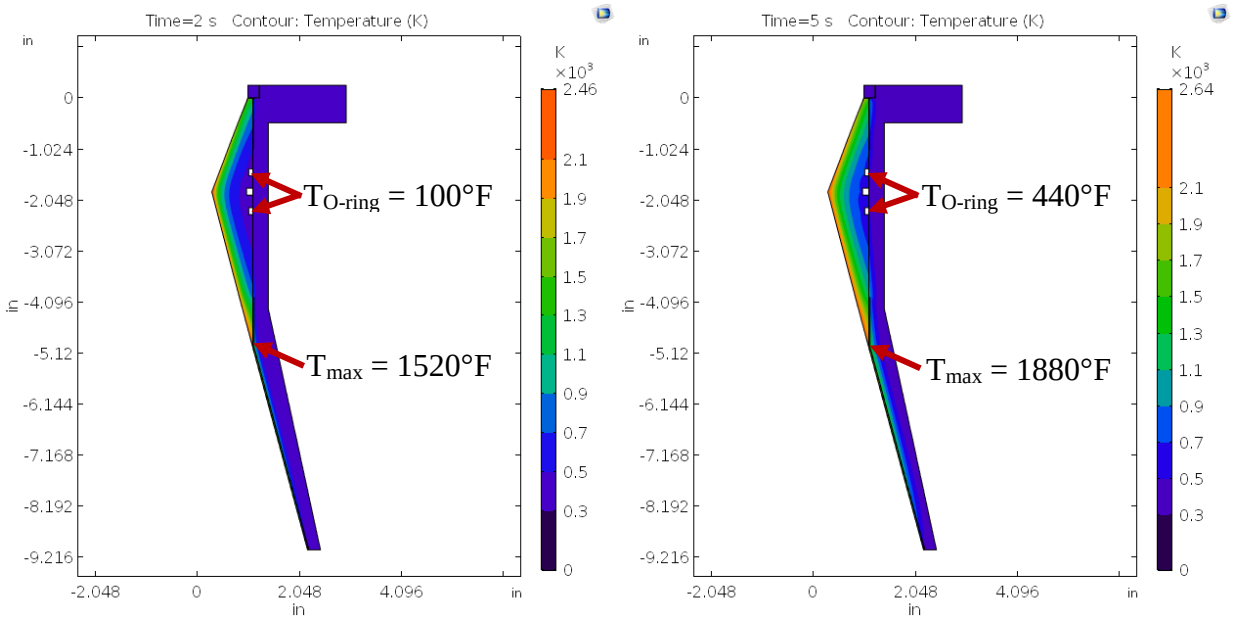

Figure 53: Thermal analysis results for 2 and 5 second firing durations with TBC.

From the results of this analysis, it can be seen that the maximum temperature experienced by the 316 stainless steel components is well below the melting temperature of the material. The thermal analysis also defined the maximum temperature that the nozzle insert O-rings would experience during the two firing durations. The maximum temperature experienced by the nozzle-insert O-rings for each of the two firing durations is shown in Figure 53 above. For a firing duration of 5 seconds, the maximum temperature experienced by the nozzle insert O-rings is approximately 440°F. While this is the maximum rated temperature for silicon O-rings, silicon does not deform or melt under momentary temperature loads. Furthermore, both nozzle insert O-rings will be changed out at the end of every test. For these reasons, we continued on to the next steps in the design process.

The design of the nozzle housing/expansion section and nozzle insert was perhaps the most difficult part of the design process. In order to protect the shear pins during testing, O-ring grooves were designed upstream and downstream of the shear pin groove in the nozzle insert. There was a maximum allowable diametrical clearance between the outer diameter of the nozzle insert and inner diameter of the nozzle housing/expansion section. The maximum diametrical clearance is defined in the extrusion limits section of the Parker O-ring Handbook [37]. The graph used for this portion of the design is provided in Figure 54 for reference.

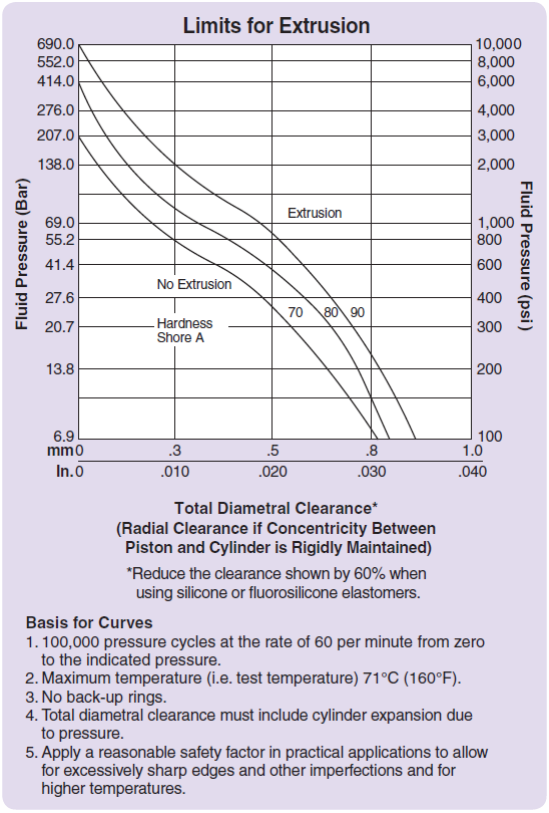

Figure 54: Graph of the extrusion limits for different material O-rings [37].

At the same time, there needed to be enough clearance to ensure that the nozzle insert does not interfere with the nozzle housing/expansion section during testing. As the nozzle insert and nozzle housing/expansion section heat up during testing, each component expands to a different degree. This is due to the temperature profile in the parts, as well as the difference in material thermal expansion coefficient between the parts. The results of the thermal analysis were used to determine an average temperature for the relevant surfaces of the two parts. Linear thermal expansion theory was used to determine the expansion of each component, and then finite element analysis (FEA) was then used to validate this linear calculation. FEA is an application that is built into Solidworks, and it can be used to determine the stress amount and concentrations within a part under real pressure and temperature loading conditions. Similar to the initial thermal analysis, we determined the thermal expansion for each of the two components after a 2 second and 5 second test. The results for the maximum thermal expansion of the outer diameter of the nozzle insert and the inner diameter for the nozzle housing/expansion section after 2 seconds and 5 seconds are given in Figure 55 and Figure 56, respectively.

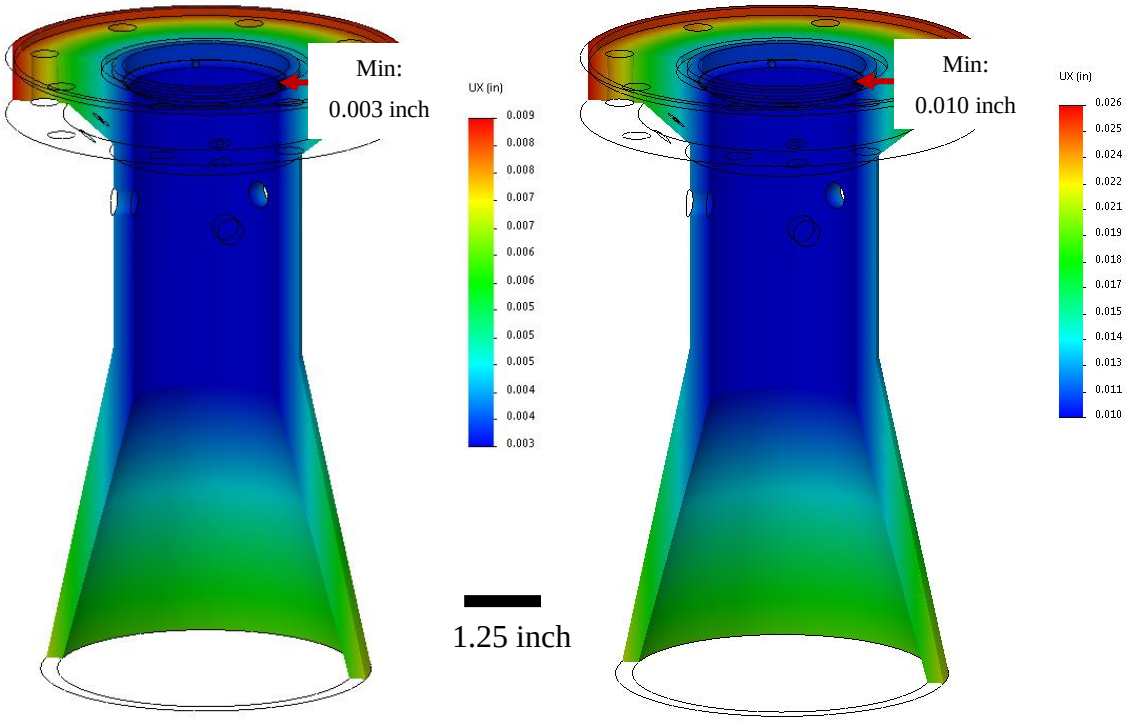

Figure 55: Minimum thermal expansion of nozzle housing/expansion section after 2 and 5 second firing duration.

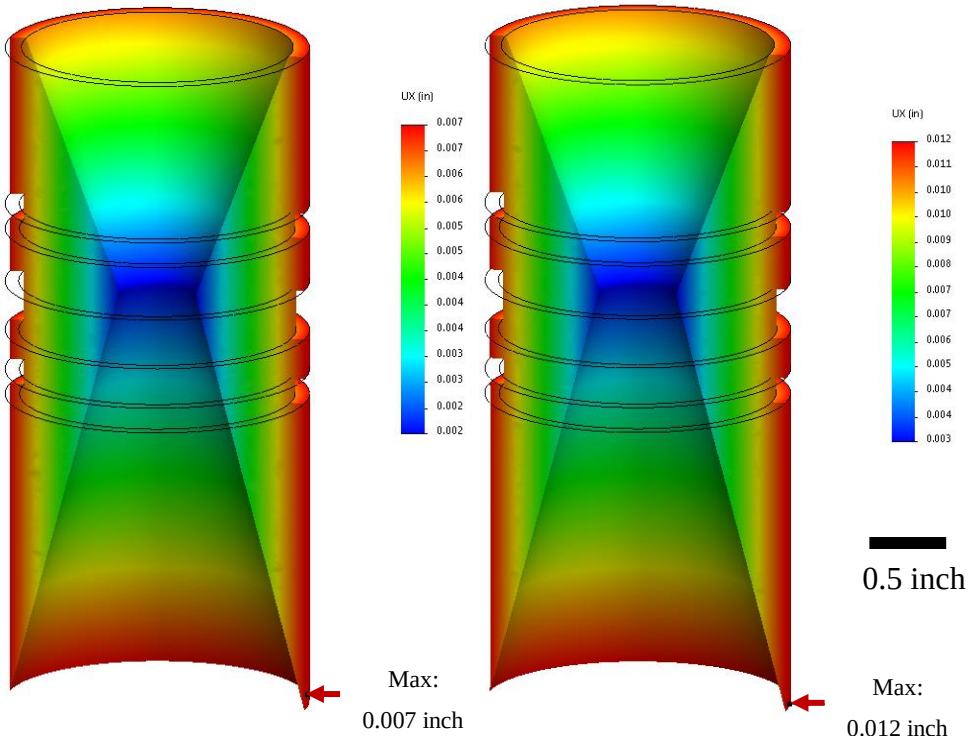

Figure 56: Maximum thermal expansion of nozzle insert after 2 and 5 second firing duration.

From the results, 0.010 inch of diametrical clearance is required between the nozzle insert and nozzle housing/expansion section to ensure that there is no interference during testing. The silicon O-rings being used have a Durometer rating of 70A. From Figure 54, these silicon O-rings can hold just over 200 psia at a diametrical clearance of 0.010 inch. While this pressure rating may seem low, there are a few factors to consider. First, the nozzle insert will expand to decrease this diametrical clearance during testing. Second, the extrusion limits for these O-rings are defined for a service life of over 100,000 cycles. Finally, this pressure of 200 psia is higher than the nominal motor operating pressure of 150 psia. The nozzle insert will be ejected in the case of over-pressurization, making the sealing of these O-rings non-critical. For the reasons above, it is determined that a diametrical clearance of 0.010 inch was both feasible and sufficient to prevent interface between the nozzle insert and nozzle housing/expansion section.

5.5 Finite Element Analysis (FEA)

The next step is to validate the CAD model design using finite element analysis (FEA). For an added layer of safety, the maximum temperature experienced by the 316 stainless steel components during the thermal analysis with TBC, 1100 K, is applied to all parts in the FEA analysis. The yield strength of materials decreases with increasing temperature, and this relationship between yield strength and temperature for 316 stainless steel is given in Figure 57.

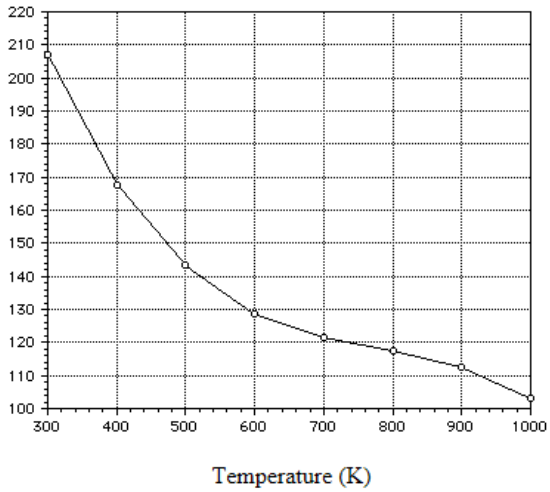

Figure 57: Relationship between 316 SS yield strength and temperature in Kelvin [38].

It can be seen from the figure above that at a temperature of 1100 K, the yield strength of 316 stainless steel is reduced by roughly a factor of 2. This means that the real factor of safety for each stainless steel component is roughly twice what is determined in the FEA results. As the FEA results serve as nothing more than validation for the design, they are excluded from the main body of this thesis. Instead, they are included in the appendix. It is determined from the FEA analysis that each of the parts has a factor of safety at or above 2, which validates the CAD design. The only component that did not have a factor of safety above 2 was the nozzle insert, with a safety factor of 1.9. However, we are less concerned with the safety factor for this component. The shear pins will fail in the event of over-pressurization, and the nozzle insert will be ejected at high velocity out of the motor. As the nozzle insert will likely not survive the impact with piping downstream of the motor, it is acceptable if the nozzle insert fails at, or slightly above, our upper pressure threshold of 600 psi. With this step, the design of the new JPL motor was completed. The final CAD rendering of the new JPL motor is given in Figure 58.

Figure 58: Final CAD rendering for the new JPL motor.

6 CONCLUSIONS

A comprehensive overview of ejector performance is compiled early in the thesis, detailing the operation of both single-stage and two-stage ejectors. This overview serves as a general reference which can be used in troubleshooting, as well as for future development.

A sensitivity analysis was performed to determine the motive/suction flow parameters which were most influential on the performance of the single-stage ejector. Through this sensitivity analysis, we determined that suction temperature was the most influential parameter for ejector performance under real-world rocket engine testing conditions. It was also determined that both the motive and suction heat capacity ratio had the smallest effect on ejector performance.

The new model proposed in this thesis was validated using experimental characterization data collected for the single-stage ejector. The validated model was then shown to be capable of predict the approximate performance of the single-stage ejector during the testing of an Aerotech F50-9T solid rocket motor within the altitude chamber. The new model was calibrated using experimental characterization data for the two-stage ejector, and was used to predict the performance of the two-stage ejector during the testing of a 90 Newton rocket engine at 54,000 ft. Through these experimental tests, the new model was proven to reliably predict the performance of both the single-stage and two-stage ejector systems under real rocket engine testing conditions.

A simple GUI was also created to provide a layer of abstraction between the underlying model and the end user. This GUI can be used by potential customers to determine the testing capabilities of the altitude chamber. The customer can determine what maximum simulated altitude is possible for the testing of their rocket engine within the altitude chamber. Similarly, the GUI can be used to determine the upper thrust limit for a given simulated altitude. This GUI provides flexibility to the end user, streamlining the process of collaboration between academia and industry.

A new rocket engine is also designed to characterize a hybrid grain configuration within the altitude chamber at reduced pressure, which serves as a continuation of the atmospheric testing campaign performed in collaboration with the Jet Propulsion Laboratory (JPL). The major steps of the design process are discussed, culminating in the final design of the motor.

This thesis provides a strong foundational modeling which can be used to support current and future work at the altitude facility of Zucrow Labs. The new model can also be used to inform the future path of the altitude facility and guide the development of new testing capabilities.

7 FUTURE WORK

In the future, the new model proposed within this thesis could be integrated into the two-stage ejector VI to allow for automated control of each stage of the ejector system. This automation would allow for instantaneous adjustment of the motive flow conditions to ensure that the ambient pressure within the altitude chamber remains absolutely constant over the course of a rocket engine test. This increase in testing control would act to increase the accuracy of future experimental testing results while simultaneously optimizing the performance of the two-stage ejector system. This automated control of the two-stage ejector system using the new model could also allow for the characterization of the full thrust-profile of a rocket engine. Similarly, this automated control could allow for the testing of a full flight profile at relevant atmospheric conditions. In this way, the altitude facility would be able to test the full thrust and altitude profile associated with a given mission.

The new model could be further improved by accounting for flow processes currently absorbed by the corrective coefficient. A parallel study of the ejector system using Computational Fluid Dynamics (CFD) would help to better inform the flow processes occurring within the ejector, yielding a more complete model. This updated model would benefit from an extension of the predictive capabilities to different ejector geometries. As the needs of the altitude facility shift over time, this updated model could be used to inform future ejector designs which provide improved thrust and simulated altitude capabilities.

With respect to the future needs of the altitude facility, the new model could also be used to determine the theoretical performance capabilities of the two-stage ejector configured in parallel, rather than series. This parallel configuration would allow for the altitude facility to support the testing of higher thrust motors at lower simulated altitudes. This new testing capability could potentially be relevant for the optimization of air-breathing propulsion systems, leading to increased collaboration between academia and industry. The model could also be used to predict the performance benefit of adding a third stage to the ejector system. The addition of a third ejector in series would allow for truly representative testing of medium-thrust rocket engines for deep space applications.

Though a preliminary theoretical sensitivity analysis was performed to determine the impact of different motive and suction flow parameters, it would be useful to experimentally test

motive fluids with different properties. This experimental data would inform the new model, allowing us to determine candidate fluids which could be used to further increase the performance of the two-stage ejector system. These new candidate fluids would serve to determine priorities regarding future facility development at ZL3.

REFERENCES

[1] R. Manikanda Kumaran, K. Vivekanand, T. Sundararajan, S. Balasubramanian, and D. Raja Manohar, "Analysis of Diffuser and Ejector Performance in a High Altitude Test Facility," in *45th AIAA/ASME/SAE/ASEE Joint Propulsion Conference & Exhibit*, Denver, Colorado, 2009.

[2] F. Kong and H. D. Kim, "Optimization study of a two-stage ejector–diffuser system," *International Journal of Heat and Mass Transfer*, vol. 101, pp. 1151–1162, Oct. 2016.

[3] K. Chunnanond and S. Aphornratana, "Ejectors: applications in refrigeration technology," *Renewable and Sustainable Energy Reviews*, vol. 8, no. 2, pp. 129–155, Apr. 2004.

[4] D.-W. Sun and I. Eames, "Recent developments in the design theories and applications of ejectors," *Journal of the Institute of Energy*, vol. 68, pp. 65–79, Jun. 1995.

[5] S. Ghorbanian and S. J. Nejad, "Ejector Modeling and Examining of Possibility of Replacing Liquid Vacuum Pump in Vacuum Production Systems," *International Journal of Chemical Engineering and Applications*, pp. 91–97, 2011.

[6] J. Liu, L. Wang, and L. Jia, "A predictive model for the performance of the ejector in refrigeration system," *Energy Conversion and Management*, vol. 150, pp. 269–276, Oct. 2017.

[7] J. R. Lines, "Understanding ejector systems necessary to troubleshoot vacuum distillation," *Oil and Gas Journal*, vol. 97, no. 7, pp. 40–45, 1999.

[8] R. K. McGovern, K. V. Bulusu, and M. A. Antar, "One-dimensional Model of an Optimal Ejector and Parametric Study of Ejector Efficiency," p. 12.

[9] J. Sarkar, "Ejector enhanced vapor compression refrigeration and heat pump systems—A review," *Renewable and Sustainable Energy Reviews*, vol. 16, no. 9, pp. 6647–6659, Dec. 2012.

[10] M. R. Kumaran, V. P. Kumaresan, T. Sundararajan, K. K., and R. D. Manohar, "Optimization of Second Throat Ejectors for High-Altitude Test Facility," *Journal of Propulsion and Power*, vol. 25, no. 3, pp. 697–706, May 2009.

[11] Graham Corporation, *Ejector - Steam Jet Ejectors - Well Operating*. .

[12] J. T. Munday and D. F. Bagster, "A New Ejector Theory Applied to Steam Jet Refrigeration," *Industrial & Engineering Chemistry Process Design and Development*, vol. 16, no. 4, pp. 442–449, Oct. 1977.

[13] J. Yan, N. Wen, L. Wang, X. Li, Z. Liu, and S. Li, “Optimization on ejector key geometries of a two-stage ejector-based multi-evaporator refrigeration system,” *Energy Conversion and Management*, vol. 175, pp. 142–150, Nov. 2018.

[14] Y. Li and Y. Wen, “The Energy-saving Analysis of Steam Ejector in plant Steam System,” in *2010 Asia-Pacific Power and Energy Engineering Conference*, 2010, pp. 1–4.

[15] N. Bilir and H. K. Ersoy, “Performance improvement of the vapour compression refrigeration cycle by a two-phase constant area ejector,” *International Journal of Energy Research*, vol. 33, no. 5, pp. 469–480, 2009.

[16] F. L. Li, B. Cao, and Q. Tian, “Analysis of Ejector Performance Using 1-D Model,” *Applied Mechanics and Materials*, vol. 253–255, pp. 781–785, Dec. 2012.

[17] T. Benjamin, “Eductor pumps: The calculations,” *World Pumps*, vol. 2001, pp. 34–38, Jan. 2001.

[18] F. D. Berkeley, “Ejectors,” *Graham Company Batavia, New York*, p. 6, 1958.

[19] C. Liao and F. R. Best, “Comprehensive Gas Ejector Model,” *Journal of Thermophysics and Heat Transfer*, vol. 24, no. 3, pp. 516–523, Jul. 2010.

[20] Y. Zhu, W. Cai, C. Wen, and Y. Li, “Simplified ejector model for control and optimization,” *Energy Conversion and Management*, vol. 49, no. 6, pp. 1424–1432, Jun. 2008.

[21] C. K. Drummond, “A Model for Prediction of STOVL Ejector Dynamics,” p. 14.

[22] J. H. Keenan and E. P. Neumann, “A Simple Air Ejector,” *Journal of Applied Mechanics*, vol. 9, pp. A75–A81, 1942.

[23] J. H. Keenan, E. P. Neumann, and F. Lustwerk, “An Investigation of Ejector Design by Analysis and Experiment,” *Journal of Applied Mechanics*, vol. ASME 17, pp. 299–309, 1950.

[24] I. Mcgregor, “The vapour-screen method of flow visualization,” *Journal of Fluid Mechanics*, vol. 11, no. 4, pp. 481–511, Dec. 1961.

[25] J. Fabri and R. Siestrunck, *Advances in Applied Mechanics*. Academic Press, 1958.

[26] B. J. Huang, J. M. Chang, C. P. Wang, and V. A. Petrenko, “A 1-D analysis of ejector performance,” *International Journal of Refrigeration*, vol. 22, no. 5, pp. 354–364, Aug. 1999.

[27] Y. Zhu, W. Cai, C. Wen, and Y. Li, “Shock circle model for ejector performance evaluation,” *Energy Conversion and Management*, vol. 48, no. 9, pp. 2533–2541, Sep. 2007.

[28] K. R. Hedges and P. G. Hill, “Compressible Flow Ejectors: Part I—Development of a Finite-Difference Flow Model,” *Journal of Fluids Engineering*, vol. 96, no. 3, p. 272, 1974.

[29] K. Banasiak and A. Hafner, “1D Computational model of a two-phase R744 ejector for expansion work recovery,” *International Journal of Thermal Sciences*, vol. 50, no. 11, pp. 2235–2247, Nov. 2011.

[30] M. Haida, M. Palacz, J. Smolka, A. J. Nowak, A. Hafner, and K. Banasiak, “A modified homogeneous relaxation model for CO2 two-phase flow in vapour ejector,” *Journal of Physics: Conference Series*, vol. 745, p. 032159, Sep. 2016.

[31] R. C. Bauer, R. C. German, and J. H. Panesci, “Methods for determining the performance of ejector-diffuser systems.,” *Journal of Spacecraft and Rockets*, vol. 3, no. 2, pp. 193–200, Feb. 1966.

[32] J. Coker, “ThrustCurve Hobby Rocket Motor Simulator Data Search,” 2008. [Online]. Available: http://www.thrustcurve.org/simfilesearch.jsp?id=701. [Accessed: 10-Jul-2019].

[33] A. Yetman, “A COMPARATIVE STUDY OF PUMPING SYSTEMS FOR A CHEMICAL PROPULSION ALTITUDE TEST STAND.” Goddard Space Flight Center, 1966.

[34] A. C. Wright, “USAF Propellant Handbooks. Nitric Acid/Nitrogen Tetroxide Oxidizers. Volume II.,” MARTIN MARIETTA AEROSPACE DENVER CO, Feb. 1977.

[35] A. Benhidjeb-Carayon, J. Gabl, and T. L. Pourpoint, “Hypergolic Ignition and Relights of a Paraffin-based Hybrid Grain,” in *2018 Joint Propulsion Conference*, 0 vols., American Institute of Aeronautics and Astronautics, 2018.

[36] J. J. Zipay, C. T. Modlin, and C. E. Larsen, “The Ultimate Factor of Safety for Aircraft and Spacecraft - Its History, Applications and Misconceptions,” in *57th AIAA/ASCE/AHS/ASC Structures, Structural Dynamics, and Materials Conference*, San Diego, California, USA, 2016.

[37] *Parker O-Ring Handbook; ORD 5700*. Cleveland, OH: Parker Hannafin Corporation, 2018.

[38] P. Karditsas and M.-J. Baptiste, “Austenitic Stainless Steel (316),” *www-ferp.ecsd.edu*. [Online]. Available: http://www-ferp.ucsd.edu/LIB/PROPS/PANOS/ss.html. [Accessed: 10-Jul-2019].

APPENDIX A. MATLAB CODES

EJECTOR_CEA_RUNNER.M:

```
function [output] = ejector_cea_runner(cea)

addpath('CEA_MATLAB', '-end');

% CEA_ROCKET_EXAMPLE: Example file for the MATLAB CEA wrapper. For in-depth
% documentation read the headers of cea_rocket_run.m,
% cea_rocket_run_single.m, and cea_rocket_read.m

% Change this variable to true to rerun CEA instead of using saved values
CEA_RUN = true;
CEA_SAVE_FILE = 'cea.mat';

Ru = 8.314;

% The CEA MATLAB code takes a MATLAB map (called a dictionary in Python or
% hash in C) as input. The dictionary uses MATLAB character arrays as the
% keys, and the value data type varies by which key is used. Details of
% each key are listed in cea_rocket_run.m
% For example: inp('key') = value.

inp = containers.Map;
inp('type') = cea.run_type;            % Sets the type of CEA calculation
inp('p') = cea.Pc;              % Chamber pressure
inp('p_unit') = cea.P_c_unit;           % Chamber pressure units
inp('o/f') = cea.o_f;             % Mixture ratio
inp('sup') = cea.AR_sup;              % Supersonic area ratios
inp('fuel') = cea.fuel_name;           % Fuel name from thermo.inp
inp('fuel_t') = cea.T_fuel;             % Fuel inlet temperature
inp('fuel_t_unit') = cea.T_fuel_unit;
inp('ox') = cea.ox_name;            % Ox name from thermo.inpj
inp('ox_t') = cea.T_ox;               % Ox inlet temperature
inp('ox_t_unit') = cea.T_ox_unit;

% inp('file_name') = 'H2O2_T.inp';    % Input/output file name

if CEA_RUN
   data = cea_rocket_run(inp);     % Call the CEA MATLAB code
   save(CEA_SAVE_FILE, 'data');
else
   load(CEA_SAVE_FILE);
end
```

```
% The output data structure, called 'data' in this case, is also a MATLAB
% map. 'data' contains a single entry for each of the CEA calculation types
% listed ('eq' and 'fr'). For instance, if only 'fr' is listed, then 'data'
% will only contain a single entry under data('fr').

if strcmp(cea.run_type,'eq') == 1
   data = data('eq');
elseif strcmp(cea.run_type,'fr') == 1
   data = data('fr');
else
   errormsg('Error: /n CEA Type must be one of the following: /n eq, fr');
end

% Use keys(data_eq) or keys(data_fr) to see the contents of each map
% respectively. Every output of CEA is contained in these keys, including
% molar concentrations. Most keys contain a 3D array with columns
% corresponding to the pressure, O/F, and area/pressure ratio inputs
% respectively. If only a single value is given for one of these inputs,
% the output will still be a 3D array. The squeeze() MATLAB function must
% be used to reduce the number of dimensions appropriately. Read the notes
% at the top of cea_rocket_read.m for more details.

% keys(data)

% Pulling out all results needed for the model
cp = squeeze(data('cp'));
output.Cp = cp(2);
gamma = squeeze(data('gammas'));
output.gamma = gamma(2);
t = squeeze(data('t'));
output.T = t(2);
isp = squeeze(data('isp'));
output.Isp = isp(2);
output.MW = (output.gamma*Ru)/(output.Cp*(output.gamma-1));
end
```

NEW_MODEL.M:

```
function eo = new_model(ei)

% This is the new model introduced in thesis.  This 1-D model uses
% isentropic relations, compressible gas dynamics, conservation of
% momentum, and conservation of energy to determine the flow conditions
% relevant for a single stage of an ejector system.  This model is only used
% for a constant-pressure ejector.  The calculation architecture is
% summarized in thesis defense presentation for reference.
```

```
R_u = 8.314; % [J/(mol*K)]

% Compressible Gas Dynamics: Motive Mass Flow [kg/s]
eo.mdot_p = (ei.P_p0)*(ei.A_t)*...
   sqrt(((ei.gamma_p/ei.R_p)*((2/(ei.gamma_p+1))^...
   ((ei.gamma_p+1)/(ei.gamma_p-1))))*(ei.n_p)/(ei.T_p0));

%VALUES FOR EXIT PLANE OF NOZZLE (p1)

% Isentropic Relation: Motive Nozzle Exit Static Pressure [Pa]
eo.P_p1 = ei.P_p0*((1+((ei.gamma_p-1)/2)*(ei.M_p1^2))^...
   ((-ei.gamma_p)/(ei.gamma_p-1)));

% Isentropic Relation: Motive Nozzle Exit Static Temperature [K]
eo.T_p1 = (ei.T_p0)*(1+((ei.gamma_p-1)/2)*(ei.M_p1^2))^(-1);

% Conditional introduced where either motive or suction gas accelerates
% isentropically to meet equal pressure mixing criteria.  Two options:
% 1) Motive nozzle exit static pressure higher than suction stagnation
% pressure
% 2) Suction stagnation pressure higher than motive nozzle exit static
% pressure
if eo.P_p1 > ei.P_s0
%   Mach Number of Motive Flow at Contracting Section Inlet
   eo.M_p2 = sqrt(((2)/(ei.gamma_p-1))*...
      ((((eo.P_p1/ei.P_s0)^((ei.gamma_p-1)/(ei.gamma_p)))*...
      (1+(((ei.gamma_p-1)/(2))*((ei.M_p1)^2))))-1));
%   Static Temperature of Motive Flow at Contracting Section Inlet [K]
   eo.T_p2 = ei.T_p0*(1+(ei.gamma_p-1)/2*eo.M_p2^2)^-1;
%   Static Pressure of Motive Flow at Contracting Section Inlet [Pa]
   eo.P_p2 = ei.P_s0;

%   Mach Number of Suction Flow at Contracting Section Inlet
   eo.M_s2 = 0;
%   Static Temperature of Suction Flow at Contracting Section Inlet [K]
   eo.T_s2 = ei.T_s0;
%   Static Pressure of Suction Flow at Contracting Section Inlet [Pa]
   eo.P_s2 = ei.P_s0;
else
%   Mach Number of Motive Flow at Contracting Section Inlet
   eo.M_p2 = ei.M_p1;
%   Static Temperature of Motive Flow at Contracting Section Inlet [K]
   eo.T_p2 = eo.T_p1;
%   Static Pressure of Motive Flow at Contracting Section Inlet [Pa]
   eo.P_p2 = eo.P_p1;
```

```
%   Mach Number of Suction Flow at Contracting Section Inlet
   eo.M_s2 = sqrt(((2)/(ei.gamma_s-1))*...
      ((((ei.P_s0/eo.P_p1)^((ei.gamma_s-1)/(ei.gamma_s)))*...
      (1+(((ei.gamma_s-1)/(2))*((0)^2))))-1));
%   Static Temperature of Suction Flow at Contracting Section Inlet [K]
   eo.T_s2 = (ei.T_s0)*((1+((ei.gamma_s-1)/2)*...
      (eo.M_s2^2))^(-1));
%   Static Pressure of Suction Flow at Contracting Section Inlet [Pa]
   eo.P_s2 = eo.P_p1;
end

% Isentropic relation: Expansion of Motive Plume in Mixing Chamber of
% Ejector [m^2]
eo.A_p2 = (ei.A_p1)*(ei.M_p1/eo.M_p2)*...
   (2/(ei.gamma_p+1)*(1+(ei.gamma_p-1)/2*eo.M_p2^2))^((ei.gamma_p+1)/(2*(ei.gamma_p-
1)))/...
   (2/(ei.gamma_p+1)*(1+(ei.gamma_p-1)/2*ei.M_p1^2))^((ei.gamma_p+1)/(2*(ei.gamma_p-
1)));

% Calculation of Suction Area [m^2]
eo.A_s2 = ei.A_c - eo.A_p2;

eo.A_mix = ei.A_3;

% Equal Pressure Mixing Assumption [Pa]
eo.P_mix = eo.P_s2;

% Mass Flow Averaged Heat Capacity [J/K]
eo.Cp_mix = (eo.mdot_p*ei.Cp_p+ei.mdot_s*ei.Cp_s)/(eo.mdot_p+ei.mdot_s);

% Calculation of Entrainment Ratio
eo.er = ei.mdot_s/eo.mdot_p;

% Mixed Mass Flow [kg/s]
eo.mdot_mix = eo.mdot_p + ei.mdot_s;

% Mixed Gamma from Comprehensive Ejector Model
eo.gamma_mix = ((ei.gamma_p/(ei.gamma_p-1))+...
   (ei.gamma_s/(ei.gamma_s-1))*(ei.R_s/ei.R_p)*eo.er)/...
   ((1/(ei.gamma_p-1))+(1/(ei.gamma_s-1))*(ei.R_s/ei.R_p)*eo.er);

% Mass Flow Averaged Molecular Weight [kg/mol]
eo.MW_mix = (eo.mdot_p*ei.MW_p+ei.mdot_s*ei.MW_s)/(eo.mdot_p+ei.mdot_s);
eo.R_mix = R_u/eo.MW_mix;
```

```
% Conservation of momentum: Mach Number of Mixed Flow
eo.M_mix =
sqrt(((ei.n_m*eo.A_p2)/(eo.gamma_mix*eo.A_mix))*(1+ei.gamma_p*eo.M_p2^2)+...
   ((eo.A_s2*ei.n_m)/(eo.gamma_mix*eo.A_mix))*(1+ei.gamma_s*eo.M_s2^2)-
1/eo.gamma_mix);

% Conservation of Energy: Static Temperature of Mixed Flow [K]
eo.T_mix = (1/(eo.mdot_mix*(eo.Cp_mix+0.5*eo.M_mix^2*eo.gamma_mix*eo.R_mix)))*...
   (eo.mdot_p*ei.Cp_p*eo.T_p2+0.5*eo.mdot_p*eo.M_p2^2*ei.gamma_p*ei.R_p*eo.T_p2+...
   ei.mdot_s*ei.Cp_s*eo.T_s2+0.5*eo.mdot_p*eo.M_s2^2*ei.gamma_s*ei.R_s*eo.T_s2);

% Shock occurs if Mach Number of Mixed Flow is greater than 1.
if eo.M_mix > 1
   % Normal Shock Theory: Static Pressure of Mixed Flow After Normal Shock [Pa]
   eo.P_3 = (eo.P_mix)*(1+((2*eo.gamma_mix)/(eo.gamma_mix+1))*...
      ((eo.M_mix^2)-1));
   % Normal Shock Theory: Mach Number of Mixed Flow After Normal Shock
   eo.M_3 = sqrt((1+((eo.gamma_mix-1)/2)*(eo.M_mix^2))/((eo.gamma_mix)*...
      (eo.M_mix^2)-((eo.gamma_mix-1)/2)));
else
%   Static Pressure of Mixed Flow without Normal Shock [Pa]
   eo.P_3 = eo.P_mix;
%   Mach Number of Mixed FLow without Normal Shock
   eo.M_3 = eo.M_mix;
end


% Isentropic Relation: Stagnation Pressure of Mixed Flow [Pa]
eo.P_e = real((eo.P_3)*((1+((eo.gamma_mix-1)/2)*(eo.M_3^2))^...
   ((eo.gamma_mix)/(eo.gamma_mix-1))));

end
```

SINGLE_STAGE_EJECTOR_SENSITIVITY_ANALYSIS.M:

```
% This script is used to determine the response of entrainment ratio to
% changes in model input conditions.  For this treatment, each of the input
% value is given some nominal value.  There is also a 10% higher and 10%
% lower value for each of the input values.  The script then scans over the
% full range of potential suction mass flow rates to determine the maximum
% suction mass flow rate which still satisfies the constant area and exit
% pressure constraints.  The suction stagnation pressure is held constant
% for this treatment.  The final sensitivity graph is created using
% excel.

% Constant Section Diameter Constraint Value [m]
```

```
D3_req = 2.15*0.0254;
% Motive Nozzle Throat Diameter [m]
Dt = 0.495*0.0254;
% Motive Nozzle Throat Area [m^2]
At = pi/4*((Dt)^2);
% Motive Nozzle Exit Diameter [m]
De = 1.16*0.0254;
% Motive Nozzle Exit Area [m^2]
Ae = pi/4*((De)^2);
% Motive Nozzle Expansion Ratio
eps = Ae/At;

% Gas coefficients
ox_a = 28.186;
ox_b = 6.3011;
ox_c = -0.74986;
ox_d = 0;

n2_a = 27.336;
n2_b = 6.23;
n2_c = -0.95082;
n2_d = 0;

% Efficiencies modified based on design point of single-stage ejector
n_p = 0.993;
n_s = 0.96;
phi_p = 0.9;
phi_m = 0.955;

%% MOTIVE FLOW PARAMETERS

% Motive Stagnation Pressure [Pa]
P_p0 = 214*6894.76;
% Motive Stagnation Temperature [F]
T_p0_F = 500;
% Motive Stagnation Temperature [K]
T_p0 = (T_p0_F-32).*5./9+273.15;
% Motive Stagnation Temperature Vector [K]
T_p0_vector = (([T_p0_F*0.9,T_p0_F,T_p0_F*1.1])-32).*5./9+273.15;
% Motive Heat Capacity Ratio
gamma_p = 1.4;
% Motive Heat Capacity Ratio Vector
gamma_p_vector = [gamma_p*0.9,gamma_p,gamma_p*1.1];
% Motive Molecular Weight [kg/mol]
MW_p = 0.02884;
% Motive Molecular Weight [kg/mol]
```

```
MW_p_vector = [MW_p*0.9,MW_p,MW_p*1.1];
% Motive Heat Capacity [J/(kg*K)]
Cp_p = (0.79*((n2_a)+(n2_b*(T_p0/1000))+...
   (n2_c*((T_p0/1000)^2))+(n2_d*((T_p0/1000)^3)))+...
   0.21*((ox_a)+(ox_b*(T_p0/1000))+(ox_c*((T_p0/1000)^2))+...
   (ox_d*((T_p0/1000)^3))))/(MW_p);
% Motive Heat Capacity Vector [J/(kg*K)]
Cp_p_vector = [Cp_p*0.9,Cp_p,Cp_p*1.1];
% Motive Heat Capacity Vector from Temperature Variance [J/(kg*K)]
Cp_p_T_p0_vector = (0.79.*((n2_a)+(n2_b.*(T_p0_vector./1000))+...
   (n2_c.*((T_p0_vector./1000).^2))+(n2_d.*((T_p0_vector./1000).^3)))+...
   0.21.*((ox_a)+(ox_b.*(T_p0_vector./1000))+(ox_c.*((T_p0_vector./1000).^2))+...
   (ox_d.*((T_p0_vector./1000).^3)))./(MW_p);
% Motive Heat Capacity Vector from Molecular Weight Variance [J/(kg*K)]
Cp_p_MW_p_vector = (0.79.*((n2_a)+(n2_b.*(T_p0./1000))+...
   (n2_c.*((T_p0./1000).^2))+(n2_d.*((T_p0./1000).^3)))+...
   0.21.*((ox_a)+(ox_b.*(T_p0./1000))+(ox_c.*((T_p0./1000).^2))+...
   (ox_d.*((T_p0./1000).^3)))./(MW_p_vector);

% Vector of Motive Nozzle Exit Mach Numbers from Heat Capacity Ratio
% Variance
M_p1_vector = zeros(1,length(gamma_p_vector));
for i = 1:length(gamma_p_vector)
   M_p1_vector(i) = Mach_finder(eps,gamma_p_vector(i),5);
end

%% SUCTION FLOW PARAMETERS

% Suction Stagnation Temperature [F]
T_s0_F = 500;
% Suction Stagnation Temperature [K]
T_s0 = (T_s0_F-32).*5./9+273.15;
% Suction Stagnation Temperature Vector [K]
T_s0_vector = (([T_s0_F*0.9,T_s0_F,T_s0_F*1.1])-32).*5./9+273.15;
% Suction Molecular Weight [kg/mol]
MW_s = 0.028;
% Suction Molecular Weight Vector [kg/mol]
MW_s_vector = [MW_s*0.9,MW_s,MW_s*1.1];
% Suction Heat Capacity Ratio
gamma_s = 1.4;
% Suction Heat Capacity Ratio Vector
gamma_s_vector = [gamma_s*0.9,gamma_s,gamma_s*1.1];
% Suction Heat Capacity Ratio [J/(kg*K)]
Cp_s = ((n2_a)+(n2_b*(T_s0/1000))+...
   (n2_c*((T_s0./1000)^2))+(n2_d*((T_s0/1000)^3)))/(MW_s);
% Suction Heat Capacity Ratio Vector [J/(kg*K)]
```

```
Cp_s_vector = [Cp_s*0.9,Cp_s,Cp_s*1.1];
% Suction Heat Capacity Ratio Vector from Temperature Variance [J/(kg*K)]
Cp_s_T_s0_vector = ((n2_a)+(n2_b.*(T_s0_vector./1000))+...
   (n2_c.*((T_s0_vector./1000).^2))+(n2_d.*((T_s0_vector./1000).^3)))./(MW_s);
% Suction Heat Capacity Ratio Vector from Molecular Weight Variance [J/(kg*K)]
Cp_s_MW_s_vector = ((n2_a)+(n2_b.*(T_s0./1000))+...
   (n2_c.*((T_s0./1000).^2))+(n2_d.*((T_s0./1000).^3)))./(MW_s_vector);
% Suction Stagnation Pressure [Pa]
P_s0 = 5*6894.76;

%% LOOPING STRUCTURE

% Matrix Used to Store all Input Value Combinations
sensitivity_matrix = zeros(13,9);

% Defining the Different Input Value Combinations
sensitivity_matrix(1,:) = [T_p0_vector(1),gamma_p_vector(2),MW_p_vector(2),...
   Cp_p_T_p0_vector(1),M_p1_vector(2),T_s0_vector(2),MW_s_vector(2),...
   gamma_s_vector(2),Cp_s_vector(2)];

sensitivity_matrix(2,:) = [T_p0_vector(3),gamma_p_vector(2),MW_p_vector(2),...
   Cp_p_T_p0_vector(3),M_p1_vector(2),T_s0_vector(2),MW_s_vector(2),...
   gamma_s_vector(2),Cp_s_vector(2)];

sensitivity_matrix(3,:) = [T_p0_vector(2),gamma_p_vector(1),MW_p_vector(2),...
   Cp_p_vector(2),M_p1_vector(1),T_s0_vector(2),MW_s_vector(2),...
   gamma_s_vector(2),Cp_s_vector(2)];

sensitivity_matrix(4,:) = [T_p0_vector(2),gamma_p_vector(3),MW_p_vector(2),...
   Cp_p_vector(2),M_p1_vector(3),T_s0_vector(2),MW_s_vector(2),...
   gamma_s_vector(2),Cp_s_vector(2)];

sensitivity_matrix(5,:) = [T_p0_vector(2),gamma_p_vector(2),MW_p_vector(1),...
   Cp_p_MW_p_vector(1),M_p1_vector(2),T_s0_vector(2),MW_s_vector(2),...
   gamma_s_vector(2),Cp_s_vector(2)];

sensitivity_matrix(6,:) = [T_p0_vector(2),gamma_p_vector(2),MW_p_vector(3),...
   Cp_p_MW_p_vector(3),M_p1_vector(2),T_s0_vector(2),MW_s_vector(2),...
   gamma_s_vector(2),Cp_s_vector(2)];

sensitivity_matrix(7,:) = [T_p0_vector(2),gamma_p_vector(2),MW_p_vector(2),...
   Cp_p_vector(2),M_p1_vector(2),T_s0_vector(1),MW_s_vector(2),...
   gamma_s_vector(2),Cp_s_T_s0_vector(1)];

sensitivity_matrix(8,:) = [T_p0_vector(2),gamma_p_vector(2),MW_p_vector(2),...
   Cp_p_vector(2),M_p1_vector(2),T_s0_vector(3),MW_s_vector(2),...
```

```
    gamma_s_vector(2),Cp_s_T_s0_vector(3)];

sensitivity_matrix(9,:) = [T_p0_vector(2),gamma_p_vector(2),MW_p_vector(2),...
    Cp_p_vector(2),M_p1_vector(2),T_s0_vector(2),MW_s_vector(1),...
    gamma_s_vector(2),Cp_s_MW_s_vector(1)];

sensitivity_matrix(10,:) = [T_p0_vector(2),gamma_p_vector(2),MW_p_vector(2),...
    Cp_p_vector(2),M_p1_vector(2),T_s0_vector(2),MW_s_vector(3),...
    gamma_s_vector(2),Cp_s_MW_s_vector(3)];

sensitivity_matrix(11,:) = [T_p0_vector(2),gamma_p_vector(2),MW_p_vector(2),...
    Cp_p_vector(2),M_p1_vector(2),T_s0_vector(2),MW_s_vector(2),...
    gamma_s_vector(1),Cp_s_vector(2)];

sensitivity_matrix(12,:) = [T_p0_vector(2),gamma_p_vector(2),MW_p_vector(2),...
    Cp_p_vector(2),M_p1_vector(2),T_s0_vector(2),MW_s_vector(2),...
    gamma_s_vector(3),Cp_s_vector(2)];

% Nominal Case Used to Compare Against Varied Test Cases
sensitivity_matrix(13,:) = [T_p0_vector(2),gamma_p_vector(2),MW_p_vector(2),...
    Cp_p_vector(2 ),M_p1_vector(2),T_s0_vector(2),MW_s_vector(2),...
    gamma_s_vector(2),Cp_s_vector(2)];

er_pass_vector = zeros(1,size(sensitivity_matrix,1));

% Going Through all of the Different Input Value Combinations
for j_3 = 1:size(sensitivity_matrix,1)

    % Loading in Relevant Input Values for this Combination Set
    sens_T_p0 = sensitivity_matrix(j_3,1);
    sens_gamma_p = sensitivity_matrix(j_3,2);
    sens_MW_p = sensitivity_matrix(j_3,3);
    sens_Cp_p = sensitivity_matrix(j_3,4);
    sens_M_p1 = sensitivity_matrix(j_3,5);
    sens_T_s0 = sensitivity_matrix(j_3,6);
    sens_MW_s = sensitivity_matrix(j_3,7);
    sens_gamma_s = sensitivity_matrix(j_3,8);
    sens_Cp_s = sensitivity_matrix(j_3,9);

    % Defining Range of Potential Suction Mass Flow Rates [kg/s]
    mdot_s_vector = 0.0001:0.0001:0.7;

    % Defining Arbitrarily High Exit Pressure
    P_e_pass = 50*101325;
    mdot_s_pass = 0;
```

```
    % Scanning Over Range of Potential Suction Mass Flow Rates
    for j_2 = 1:size(mdot_s_vector,2)

        % Loading in Current Suction Mass Flow Rate Being Evaluated
        mdot_s = mdot_s_vector(j_2);

        % Running the Huang Model
        [P_e,D_3,mdot_p] =...
            onedimensionalsolver...
            (At,Ae,sens_T_p0,P_p0,sens_Cp_p,sens_MW_p,sens_gamma_p,mdot_s,...

sens_T_s0,P_s0,sens_Cp_s,sens_MW_s,sens_gamma_s,n_p,n_s,phi_p,phi_m,sens_M_p1);

        % Successful Run Must Satisfy Both Area and Pressure Requirement
        if (D_3 <= D3_req -  0.005 || D_3 >= D3_req +  0.005) || (P_e < 101325)
            P_e = 0;
        else
            % This conditional is used to find the maximum suction mass
            % flow rate which still satisfies the above constraints
            if mdot_s > mdot_s_pass
                P_e_pass = P_e;
                mdot_s_pass = mdot_s;
            end
        end
    end

    % Saves the maximum suction mass flow rate, and thus entrainment ratio
    er_pass_vector(j_3) = mdot_s_pass/mdot_p;

end

t = 1:13;

plot(t,er_pass_vector);

% figure(1)
% plot(motive_pressure_vector_psi, er_vector)
% title('Entrainment Ratio vs Motive Pressure');
% ylabel('Entrainment Ratio');
% xlabel('Motive Pressure (psi)');
% legend('T_{s0} = 70 F','T_{s0} = 500 F','T_{s0} = 1000 F','T_{s0} = 1500 F');
% hold on
%
% figure(2)
% plot(motive_pressure_vector_psi, mdot_s_vector_lbs)
% title('Suction Flow Rate vs Motive Pressure');
```

```
% ylabel('Suction Flow Rate (lbm/s)');
% xlabel('Motive Pressure (psi)');
% legend('T_{s0} = 70 F','T_{s0} = 500 F','T_{s0} = 1000 F','T_{s0} = 1500 F');
% hold on
```

SINGLE_STAGE_EJECTOR_SENSITIVITY_ANALYSIS_RW.M:

```
% This script is used to determine the response of entrainment ratio to
% changes in model input conditions.  For this treatment, each of the input
% value is given some nominal value.  The high and low input values are
% defined relative to what we expect - or could expect - during a rocket
% test.  The script then scans over the full range of potential
% suction mass flow rates to determine the maximum suction mass flow rate
% which still satisfies the constant area and exit pressure constraints.
% The final sensitivity graph is created using excel.

% Constant Section Diameter Constraint Value [m]
D3_req = 2.15*0.0254;
% Motive Nozzle Throat Diameter [m]
Dt = 0.495*0.0254;
% Motive Nozzle Throat Area [m^2]
At = pi/4*((Dt)^2);
% Motive Nozzle Exit Diameter [m]
De = 1.16*0.0254;
% Motive Nozzle Exit Area [m^2]
Ae = pi/4*((De)^2);
% Motive Nozzle Expansion Ratio
eps = Ae/At;

% Gas coefficients

ox_a = 28.186;
ox_b = 6.3011;
ox_c = -0.74986;
ox_d = 0;

n2_a = 27.336;
n2_b = 6.23;
n2_c = -0.95082;
n2_d = 0;

% Efficiencies modified based on design point of single-stage ejector
n_p = 0.993;
n_s = 0.96;
phi_p = 0.9;
phi_m = 0.955;
```

```
%% MOTIVE FLOW PARAMETERS

% Motive Stagnation Pressure [Pa]
P_p0 = 214*6894.76;
% Motive Stagnation Temperature [K]
T_p0 = 477; % K
% Motive Stagnation Temperature Vector [K]
T_p0_vector = [298,477,700];
% Motive Heat Capacity Ratio
gamma_p = 1.4;
% Motive Heat Capacity Ratio Vector
gamma_p_vector = [1.28,1.4,1.67];
% Motive Molecular Weight [kg/mol]
MW_p = 0.02884; % kg/mol
% Motive Molecular Weight [kg/mol]
MW_p_vector = [0.018,0.02884,0.039];
% Motive Heat Capacity [J/(kg*K)]
Cp_p = (0.79*((n2_a)+(n2_b*(T_p0/1000))+...
    (n2_c*((T_p0/1000)^2))+(n2_d*((T_p0/1000)^3)))+...
    0.21*((ox_a)+(ox_b*(T_p0/1000))+(ox_c*((T_p0/1000)^2))+...
    (ox_d*((T_p0/1000)^3))))/(MW_p); % J/kg-K
% Motive Heat Capacity Vector [J/(kg*K)]
Cp_p_vector = [Cp_p*0.9,Cp_p,Cp_p*1.1];
% Motive Heat Capacity Vector from Temperature Variance [J/(kg*K)]
Cp_p_T_p0_vector = (0.79.*((n2_a)+(n2_b.*(T_p0_vector./1000))+...
    (n2_c.*((T_p0_vector./1000).^2))+(n2_d.*((T_p0_vector./1000).^3)))+...
    0.21.*((ox_a)+(ox_b.*(T_p0_vector./1000))+(ox_c.*((T_p0_vector./1000).^2))+...
    (ox_d.*((T_p0_vector./1000).^3)))).*(MW_p); % J/kg-K
% Motive Heat Capacity Vector from Molecular Weight Variance [J/(kg*K)]
Cp_p_MW_p_vector = (0.79.*((n2_a)+(n2_b.*(T_p0./1000))+...
    (n2_c.*((T_p0./1000).^2))+(n2_d.*((T_p0./1000).^3)))+...
    0.21.*((ox_a)+(ox_b.*(T_p0./1000))+(ox_c.*((T_p0./1000).^2))+...
    (ox_d.*((T_p0./1000).^3)))).*(MW_p_vector); % J/kg-K

M_p1_vector = zeros(1,length(gamma_p_vector));
for i = 1:length(gamma_p_vector)
    M_p1_vector(i) = Mach_finder(eps,gamma_p_vector(i),5);
end

%% SUCTION FLOW PARAMETERS

% Suction Stagnation Temperature [K]
T_s0 = 1000; % K
% Suction Stagnation Temperature Vector [K]
T_s0_vector = [298,1000,2500]; % K
```

```
% Suction Molecular Weight [kg/mol]
MW_s = 0.02;
% Suction Molecular Weight Vector [kg/mol]
MW_s_vector = [0.010,0.020,0.028];
% Suction Heat Capacity Ratio
gamma_s = 1.3;
% Suction Heat Capacity Ratio Vector
gamma_s_vector = [1.19,1.3,1.4];
% Suction Heat Capacity Ratio [J/(kg*K)]
Cp_s = ((n2_a)+(n2_b*(T_s0/1000))+...
   (n2_c*((T_s0./1000)^2))+(n2_d*((T_s0/1000)^3)))/(MW_s); % J/kg-K
% Suction Heat Capacity Ratio Vector [J/(kg*K)]
Cp_s_vector = [Cp_s*0.9,Cp_s,Cp_s*1.1];
% Suction Heat Capacity Ratio Vector from Temperature Variance [J/(kg*K)]
Cp_s_T_s0_vector = ((n2_a)+(n2_b.*(T_s0_vector./1000))+...
   (n2_c.*((T_s0_vector./1000).^2))+(n2_d.*((T_s0_vector./1000).^3)))./(MW_s); % J/kg-K
% Suction Heat Capacity Ratio Vector from Molecular Weight Variance [J/(kg*K)]
Cp_s_MW_s_vector = ((n2_a)+(n2_b.*(T_s0./1000))+...
   (n2_c.*((T_s0./1000).^2))+(n2_d.*((T_s0./1000).^3)))./(MW_s_vector); % J/kg-K
% Suction Stagnation Pressure [Pa]
P_s0 = 5*6894.76;    % Pa

%% LOOPING STRUCTURE

% Matrix Used to Store all Input Value Combinations
sensitivity_matrix = zeros(13,9);

% Defining the Different Input Value Combinations
sensitivity_matrix(1,:) = [T_p0_vector(1),gamma_p_vector(2),MW_p_vector(2),...
   Cp_p_T_p0_vector(1),M_p1_vector(2),T_s0_vector(2),MW_s_vector(2),...
   gamma_s_vector(2),Cp_s_vector(2)];

sensitivity_matrix(2,:) = [T_p0_vector(3),gamma_p_vector(2),MW_p_vector(2),...
   Cp_p_T_p0_vector(3),M_p1_vector(2),T_s0_vector(2),MW_s_vector(2),...
   gamma_s_vector(2),Cp_s_vector(2)];

sensitivity_matrix(3,:) = [T_p0_vector(2),gamma_p_vector(1),MW_p_vector(2),...
   Cp_p_vector(2),M_p1_vector(1),T_s0_vector(2),MW_s_vector(2),...
   gamma_s_vector(2),Cp_s_vector(2)];

sensitivity_matrix(4,:) = [T_p0_vector(2),gamma_p_vector(3),MW_p_vector(2),...
   Cp_p_vector(2),M_p1_vector(3),T_s0_vector(2),MW_s_vector(2),...
   gamma_s_vector(2),Cp_s_vector(2)];

sensitivity_matrix(5,:) = [T_p0_vector(2),gamma_p_vector(2),MW_p_vector(1),...
   Cp_p_MW_p_vector(1),M_p1_vector(2),T_s0_vector(2),MW_s_vector(2),...
```

```
    gamma_s_vector(2),Cp_s_vector(2)];

sensitivity_matrix(6,:) = [T_p0_vector(2),gamma_p_vector(2),MW_p_vector(3),...
    Cp_p_MW_p_vector(3),M_p1_vector(2),T_s0_vector(2),MW_s_vector(2),...
    gamma_s_vector(2),Cp_s_vector(2)];

sensitivity_matrix(7,:) = [T_p0_vector(2),gamma_p_vector(2),MW_p_vector(2),...
    Cp_p_vector(2),M_p1_vector(2),T_s0_vector(1),MW_s_vector(2),...
    gamma_s_vector(2),Cp_s_T_s0_vector(1)];

sensitivity_matrix(8,:) = [T_p0_vector(2),gamma_p_vector(2),MW_p_vector(2),...
    Cp_p_vector(2),M_p1_vector(2),T_s0_vector(3),MW_s_vector(2),...
    gamma_s_vector(2),Cp_s_T_s0_vector(3)];

sensitivity_matrix(9,:) = [T_p0_vector(2),gamma_p_vector(2),MW_p_vector(2),...
    Cp_p_vector(2),M_p1_vector(2),T_s0_vector(2),MW_s_vector(1),...
    gamma_s_vector(2),Cp_s_MW_s_vector(1)];

sensitivity_matrix(10,:) = [T_p0_vector(2),gamma_p_vector(2),MW_p_vector(2),...
    Cp_p_vector(2),M_p1_vector(2),T_s0_vector(2),MW_s_vector(3),...
    gamma_s_vector(2),Cp_s_MW_s_vector(3)];

sensitivity_matrix(11,:) = [T_p0_vector(2),gamma_p_vector(2),MW_p_vector(2),...
    Cp_p_vector(2),M_p1_vector(2),T_s0_vector(2),MW_s_vector(2),...
    gamma_s_vector(1),Cp_s_vector(2)];

sensitivity_matrix(12,:) = [T_p0_vector(2),gamma_p_vector(2),MW_p_vector(2),...
    Cp_p_vector(2),M_p1_vector(2),T_s0_vector(2),MW_s_vector(2),...
    gamma_s_vector(3),Cp_s_vector(2)];

% Nominal Case Used to Compare Against Varied Test Cases
sensitivity_matrix(13,:) = [T_p0_vector(2),gamma_p_vector(2),MW_p_vector(2),...
    Cp_p_vector(2),M_p1_vector(2),T_s0_vector(2),MW_s_vector(2),...
    gamma_s_vector(2),Cp_s_vector(2)];

er_pass_vector = zeros(1,size(sensitivity_matrix,1));

% Going Through all of the Different Input Value Combinations
for j_3 = 1:size(sensitivity_matrix,1)

    % Loading in Relevant Input Values for this Combination Set
    sens_T_p0 = sensitivity_matrix(j_3,1);
    sens_gamma_p = sensitivity_matrix(j_3,2);
    sens_MW_p = sensitivity_matrix(j_3,3);
    sens_Cp_p = sensitivity_matrix(j_3,4);
    sens_M_p1 = sensitivity_matrix(j_3,5);
```

```
    sens_T_s0 = sensitivity_matrix(j_3,6);
    sens_MW_s = sensitivity_matrix(j_3,7);
    sens_gamma_s = sensitivity_matrix(j_3,8);
    sens_Cp_s = sensitivity_matrix(j_3,9);

    % Defining Range of Potential Suction Mass Flow Rates [kg/s]
    mdot_s_vector = 0.0001:0.0001:0.7; %kg/s

    % Defining Arbitrarily High Exit Pressure
    P_e_pass = 50*101325;
    mdot_s_pass = 0;

    % Scanning Over Range of Potential Suction Mass Flow Rates
    for j_2 = 1:size(mdot_s_vector,2)

        % Loading in Current Suction Mass Flow Rate Being Evaluated
        mdot_s = mdot_s_vector(j_2);

        % Running the Huang Model
        [P_e,D_3,mdot_p] =...
            onedimensionalsolver...
            (At,Ae,sens_T_p0,P_p0,sens_Cp_p,sens_MW_p,sens_gamma_p,mdot_s,...

sens_T_s0,P_s0,sens_Cp_s,sens_MW_s,sens_gamma_s,n_p,n_s,phi_p,phi_m,sens_M_p1);

        % Successful Run Must Satisfy Both Area and Pressure Requirement
        if (D_3 <= D3_req -  0.005 || D_3 >= D3_req +  0.005) || (P_e < 101325)
            P_e = 0;
        else
            % This conditional is used to find the maximum suction mass
            % flow rate which still satisfies the above constraints
            if mdot_s > mdot_s_pass
                P_e_pass = P_e;
                mdot_s_pass = mdot_s;
            end
        end
    end

    % Saves the maximum suction mass flow rate, and thus entrainment ratio
    er_pass_vector(j_3) = mdot_s_pass/mdot_p;

end

t = 1:13;

plot(t,er_pass_vector);
```

```
% figure(1)
% plot(motive_pressure_vector_psi, er_vector)
% title('Entrainment Ratio vs Motive Pressure');
% ylabel('Entrainment Ratio');
% xlabel('Motive Pressure (psi)');
% legend('T_{s0} = 70 F','T_{s0} = 500 F','T_{s0} = 1000 F','T_{s0} = 1500 F');
% hold on
%
% figure(2)
% plot(motive_pressure_vector_psi, mdot_s_vector_lbs)
% title('Suction Flow Rate vs Motive Pressure');
% ylabel('Suction Flow Rate (lbm/s)');
% xlabel('Motive Pressure (psi)');
% legend('T_{s0} = 70 F','T_{s0} = 500 F','T_{s0} = 1000 F','T_{s0} = 1500 F');
% hold on
```

SINGLE_STAGE_EJECTOR_SENSITIVITY_ANALYSIS_RW_ALT.M:

```
% This script is used to determine the response of simulated altitude to
% changes in model input conditions.  For this treatment, each of the input
% value is given some nominal value.  The high and low input values are
% defined relative to what we expect - or could expect - during a rocket
% test.  The script then scans over the full range of potential
% suction stagnation pressures to determine the minimum suction stagnation
% pressure which still satisfies the constant area and exit pressure
% constraints. The final sensitivity graph is created using excel.

% Constant Section Diameter Constraint Value [m]
D3_req = 2.15*0.0254;
% Motive Nozzle Throat Diameter [m]
Dt = 0.495*0.0254;
% Motive Nozzle Throat Area [m^2]
At = pi/4*((Dt)^2);
% Motive Nozzle Exit Diameter [m]
De = 1.16*0.0254;
% Motive Nozzle Exit Area [m^2]
Ae = pi/4*((De)^2);
% Motive Nozzle Expansion Ratio
eps = Ae/At;

% Gas coefficients
ox_a = 28.186;
ox_b = 6.3011;
ox_c = -0.74986;
ox_d = 0;
```

```
n2_a = 27.336;
n2_b = 6.23;
n2_c = -0.95082;
n2_d = 0;

% Efficiencies modified based on design point of single-stage ejector
n_p = 0.993;
n_s = 0.96;
phi_p = 0.9;
phi_m = 0.955;

% These lines and the for loop are used to define the relationship between
% altitude and pressure
alt =  0:10:100000;
pressure = zeros(1,size(alt,2));

for i = 1:length(alt)
   [a_temp, p_temp, rho_temp, h_temp] = atmosphere(alt(i),1);
   pressure(i) = p_temp*47.880258888889;
end

%% MOTIVE FLOW PARAMETERS

% Motive Stagnation Pressure [Pa]
P_p0 = 215*6894.76;
% Motive Stagnation Temperature [K]
T_p0 = 477;
% Motive Stagnation Temperature Vector [K]
T_p0_vector = [298,477,700];
% Motive Heat Capacity Ratio
gamma_p = 1.4;
% Motive Heat Capacity Ratio Vector
gamma_p_vector = [1.28,1.4,1.67];
% Motive Molecular Weight [kg/mol]
MW_p = 0.02884;
% Motive Molecular Weight [kg/mol]
MW_p_vector = [0.018,0.028,0.039];
% Motive Heat Capacity [J/(kg*K)]
Cp_p = (0.79*((n2_a)+(n2_b*(T_p0/1000))+...
   (n2_c*((T_p0/1000)^2))+(n2_d*((T_p0/1000)^3)))+...
   0.21*((ox_a)+(ox_b*(T_p0/1000))+(ox_c*((T_p0/1000)^2))+...
   (ox_d*((T_p0/1000)^3))))/(MW_p); % J/kg-K
% Motive Heat Capacity Vector [J/(kg*K)]
Cp_p_vector = [Cp_p*0.9,Cp_p,Cp_p*1.1];
% Motive Heat Capacity Vector from Temperature Variance [J/(kg*K)]
```

```
Cp_p_T_p0_vector = (0.79.*((n2_a)+(n2_b.*(T_p0_vector./1000))+...
   (n2_c.*((T_p0_vector./1000).^2))+(n2_d.*((T_p0_vector./1000).^3)))+...
   0.21.*((ox_a)+(ox_b.*(T_p0_vector./1000))+(ox_c.*((T_p0_vector./1000).^2))+...
   (ox_d.*((T_p0_vector./1000).^3)))./(MW_p); % J/kg-K
% Motive Heat Capacity Vector from Molecular Weight Variance [J/(kg*K)]
Cp_p_MW_p_vector = (0.79.*((n2_a)+(n2_b.*(T_p0./1000))+...
   (n2_c.*((T_p0./1000).^2))+(n2_d.*((T_p0./1000).^3)))+...
   0.21.*((ox_a)+(ox_b.*(T_p0./1000))+(ox_c.*((T_p0./1000).^2))+...
   (ox_d.*((T_p0./1000).^3)))./(MW_p_vector); % J/kg-K

% Vector of Motive Nozzle Exit Mach Numbers from Heat Capacity Ratio
% Variance
M_p1_vector = zeros(1,length(gamma_p_vector));
for i = 1:length(gamma_p_vector)
   M_p1_vector(i) = Mach_finder(eps,gamma_p_vector(i),5);
end

%% SUCTION FLOW PARAMETERS

% Suction Stagnation Temperature [K]
T_s0 = 1644;
% Suction Stagnation Temperature Vector [K]
T_s0_vector = [298,1644,2500];
% Suction Molecular Weight [kg/mol]
MW_s = 0.02;
% Suction Molecular Weight Vector [kg/mol]
MW_s_vector = [0.010,0.020,0.028];
% Suction Heat Capacity Ratio
gamma_s = 1.3;
% Suction Heat Capacity Ratio Vector
gamma_s_vector = [1.19,1.3,1.4];
% Suction Heat Capacity Ratio [J/(kg*K)]
Cp_s = ((n2_a)+(n2_b*(T_s0/1000))+...
   (n2_c*((T_s0./1000)^2))+(n2_d*((T_s0/1000)^3)))/(MW_s);
% Suction Heat Capacity Ratio Vector [J/(kg*K)]
Cp_s_vector = [Cp_s*0.9,Cp_s,Cp_s*1.1];
% Suction Heat Capacity Ratio Vector from Temperature Variance [J/(kg*K)]
Cp_s_T_s0_vector = ((n2_a)+(n2_b.*(T_s0_vector./1000))+...
   (n2_c.*((T_s0_vector./1000).^2))+(n2_d.*((T_s0_vector./1000).^3)))./(MW_s);
% Suction Heat Capacity Ratio Vector from Molecular Weight Variance [J/(kg*K)]
Cp_s_MW_s_vector = ((n2_a)+(n2_b.*(T_s0./1000))+...
   (n2_c.*((T_s0./1000).^2))+(n2_d.*((T_s0./1000).^3)))./(MW_s_vector);
% Suction Mass Flow Rate [kg/s]
mdot_s = 0.033;

%% LOOPING STRUCTURE
```

```
% Matrix Used to Store all Input Value Combinations
sensitivity_matrix = zeros(13,9);

% Defining the Different Input Value Combinations
sensitivity_matrix(1,:) = [T_p0_vector(1),gamma_p_vector(2),MW_p_vector(2),...
    Cp_p_T_p0_vector(1),M_p1_vector(2),T_s0_vector(2),MW_s_vector(2),...
    gamma_s_vector(2),Cp_s_vector(2)];

sensitivity_matrix(2,:) = [T_p0_vector(3),gamma_p_vector(2),MW_p_vector(2),...
    Cp_p_T_p0_vector(3),M_p1_vector(2),T_s0_vector(2),MW_s_vector(2),...
    gamma_s_vector(2),Cp_s_vector(2)];

sensitivity_matrix(3,:) = [T_p0_vector(2),gamma_p_vector(1),MW_p_vector(2),...
    Cp_p_vector(2),M_p1_vector(1),T_s0_vector(2),MW_s_vector(2),...
    gamma_s_vector(2),Cp_s_vector(2)];

sensitivity_matrix(4,:) = [T_p0_vector(2),gamma_p_vector(3),MW_p_vector(2),...
    Cp_p_vector(2),M_p1_vector(3),T_s0_vector(2),MW_s_vector(2),...
    gamma_s_vector(2),Cp_s_vector(2)];

sensitivity_matrix(5,:) = [T_p0_vector(2),gamma_p_vector(2),MW_p_vector(1),...
    Cp_p_MW_p_vector(1),M_p1_vector(2),T_s0_vector(2),MW_s_vector(2),...
    gamma_s_vector(2),Cp_s_vector(2)];

sensitivity_matrix(6,:) = [T_p0_vector(2),gamma_p_vector(2),MW_p_vector(3),...
    Cp_p_MW_p_vector(3),M_p1_vector(2),T_s0_vector(2),MW_s_vector(2),...
    gamma_s_vector(2),Cp_s_vector(2)];

sensitivity_matrix(7,:) = [T_p0_vector(2),gamma_p_vector(2),MW_p_vector(2),...
    Cp_p_vector(2),M_p1_vector(2),T_s0_vector(1),MW_s_vector(2),...
    gamma_s_vector(2),Cp_s_T_s0_vector(1)];

sensitivity_matrix(8,:) = [T_p0_vector(2),gamma_p_vector(2),MW_p_vector(2),...
    Cp_p_vector(2),M_p1_vector(2),T_s0_vector(3),MW_s_vector(2),...
    gamma_s_vector(2),Cp_s_T_s0_vector(3)];

sensitivity_matrix(9,:) = [T_p0_vector(2),gamma_p_vector(2),MW_p_vector(2),...
    Cp_p_vector(2),M_p1_vector(2),T_s0_vector(2),MW_s_vector(1),...
    gamma_s_vector(2),Cp_s_MW_s_vector(1)];

sensitivity_matrix(10,:) = [T_p0_vector(2),gamma_p_vector(2),MW_p_vector(2),...
    Cp_p_vector(2),M_p1_vector(2),T_s0_vector(2),MW_s_vector(3),...
    gamma_s_vector(2),Cp_s_MW_s_vector(3)];

sensitivity_matrix(11,:) = [T_p0_vector(2),gamma_p_vector(2),MW_p_vector(2),...
```

```
    Cp_p_vector(2),M_p1_vector(2),T_s0_vector(2),MW_s_vector(2),...
    gamma_s_vector(1),Cp_s_vector(2)];

sensitivity_matrix(12,:) = [T_p0_vector(2),gamma_p_vector(2),MW_p_vector(2),...
    Cp_p_vector(2),M_p1_vector(2),T_s0_vector(2),MW_s_vector(2),...
    gamma_s_vector(3),Cp_s_vector(2)];

% Nominal Case Used to Compare Against Varied Test Cases
sensitivity_matrix(13,:) = [T_p0_vector(2),gamma_p_vector(2),MW_p_vector(2),...
    Cp_p_vector(2),M_p1_vector(2),T_s0_vector(2),MW_s_vector(2),...
    gamma_s_vector(2),Cp_s_vector(2)];

P_s0_pass_vector = zeros(1,size(sensitivity_matrix,1));

% Going Through all of the Different Input Value Combinations
for j_3 = 1:size(sensitivity_matrix,1)

    % Loading in Relevant Input Values for this Combination Set
    sens_T_p0 = sensitivity_matrix(j_3,1);
    sens_gamma_p = sensitivity_matrix(j_3,2);
    sens_MW_p = sensitivity_matrix(j_3,3);
    sens_Cp_p = sensitivity_matrix(j_3,4);
    sens_M_p1 = sensitivity_matrix(j_3,5);
    sens_T_s0 = sensitivity_matrix(j_3,6);
    sens_MW_s = sensitivity_matrix(j_3,7);
    sens_gamma_s = sensitivity_matrix(j_3,8);
    sens_Cp_s = sensitivity_matrix(j_3,9);

    % Defining Range of Potential Suction Stagnation Pressures [Pa]
    P_s0_vector = 0.001*6894.76:0.001*6894.76:14.7*6894.76;


    % Defining Arbitrarily High Exit Pressure
    P_e_pass = 50*101325;
    P_s0_pass = 20*6894.76;

    % Scanning Over Range of Potential Suction Stagnation Pressures
    for j_2 = 1:size(P_s0_vector,2)

        % Loading in Current Suction Stagnation Pressure Being Evaluated
        P_s0 = P_s0_vector(j_2);

        % Running the Huang Model
        [P_e,D_3,mdot_p] =...
            onedimensionalsolver...
            (At,Ae,sens_T_p0,P_p0,sens_Cp_p,sens_MW_p,sens_gamma_p,mdot_s,...
```

```
sens_T_s0,P_s0,sens_Cp_s,sens_MW_s,sens_gamma_s,n_p,n_s,phi_p,phi_m,sens_M_p1);

        % Successful Run Must Satisfy Both Area and Pressure Requirement
        if (D_3 <= D3_req -  0.005 || D_3 >= D3_req +  0.005) || (P_e < 101325)
            P_e = 0;
        else
            % This conditional is used to find the maximum suction mass
            % flow rate which still satisfies the above constraints
            if P_s0 < P_s0_pass
                P_e_pass = P_e;
                P_s0_pass = P_s0;
            end
        end
    end

    % Saves the minimum suction stagnation pressure
    P_s0_pass_vector(j_3) = P_s0_pass;

end

% Converting minimum suction stagnation pressures to equivalent simulated
% altitudes
alt_pass_vector = zeros(1,length(P_s0_pass_vector));

for i = 1:length(P_s0_pass_vector)
    P_s0_temp = P_s0_pass_vector(i);
    [~,index] = min(abs(pressure-P_s0_temp));
    alt_pass_vector(i) = alt(index);
end

t = 1:13;
figure(1)
hold on
plot(pressure./6894.76,alt);
scatter(P_s0_pass_vector./6894.76,alt_pass_vector);
hold off

% figure(1)
% plot(motive_pressure_vector_psi, er_vector)
% title('Entrainment Ratio vs Motive Pressure');
% ylabel('Entrainment Ratio');
% xlabel('Motive Pressure (psi)');
% legend('T_{s0} = 70 F','T_{s0} = 500 F','T_{s0} = 1000 F','T_{s0} = 1500 F');
% hold on
%
```

```
% figure(2)
% plot(motive_pressure_vector_psi, mdot_s_vector_lbs)
% title('Suction Flow Rate vs Motive Pressure');
% ylabel('Suction Flow Rate (lbm/s)');
% xlabel('Motive Pressure (psi)');
% legend('T_{s0} = 70 F','T_{s0} = 500 F','T_{s0} = 1000 F','T_{s0} = 1500 F');
% hold on
```

TEST_DATA_ANALYSIS_ SINGLE_STAGE_EJECTOR_4_5_EXP.M:

```
% This script is used to load experimental characterization data for the
% single-stage ejector with low expansion ratio nozzle.  The new 1-D model
% is then used to determine the momentum coefficient value that satisfies
% each of the experimentally defined data points.  The results momentum
% coefficient curve is then shown graphically.  Must have curve-fitting
% toolbox to run this script.

% Loading Data from Single-Stage Ejector Performance Characterization
test_data = xlsread('VE_4_5_Test_Results.xlsx',1,'A2:D196');
% Motive Stagnation Pressure [Pa]
P_p0_vector = ((test_data(:,1)).').*6894.75729;
% Suction Mass Flow Rate [kg/s]
mdot_s_vector = ((test_data(:,4)).')./2.20462262;
% Suction Stagnation Pressure [Pa]
P_s0_vector = ((test_data(:,2)).').*6894.75729;
% Mixing Chamber Static Pressure [Pa]
P_mc_vector = ((test_data(:,3)).').*6894.75729;

%Typical isentropic efficiency for CD nozzle
n_p = 0.993;

% Initializing Momentum Coefficient Scanning Range
n_m_vector = 0.001:0.001:1;

%DEFINING GEOMETRY VALUES AND CONSTANT VALUES

% Constant Section Diameter [m]
D_3 = 2.15*0.0254;
% Constant Section Area [m^2]
A_3 = (pi)/(4)*((D_3)^2);
% Motive Nozzle Throat Diameter [m]
D_t = 0.495*0.0254;
% Motive Nozzle Throat Area [m^2]
A_t = pi/4*((D_t)^2);
% Motive Nozzle Exit Diameter [m]
D_p1 = 1.16*0.0254;
```

```
% Motive NOzzle Exit Area [m^2]
A_p1 = pi/4*((D_p1)^2);
% Motive Nozzle Expansion Ratio
eps = A_p1/A_t;
% Contraction Section Diameter [m]
D_c = 4*0.0254;
% Contraction Section Area [m^2]
A_c = pi/4*((D_c)^2);

% Coefficients Used for Heat Capacity Calaculation
a_ox = 28.186;
b_ox = 6.3011;
c_ox = -0.74986;
d_ox = 0;

% Coefficients Used for Heat Capacity Calculation
a_n2 = 27.336;
b_n2 = 6.23;
c_n2 = -0.95082;
d_n2 = 0;

% Universal Gas Constant [J/(K*mol)]
R_u = 8.314;

%% DEFINING MOTIVE FLOW VALUES

% Motive Stagnation Temperature [K]
T_p0 = 298;
% Motive Heat Capacity Ratio
gamma_p = 1.4;
% Motive Molecular Weight [kg/mol]
MW_p = 0.029;
% Motive Heat Capacity [J/K]
Cp_p = (0.79*((a_n2)+(b_n2*(T_p0/1000))+...
    (c_n2*((T_p0/1000)^2))+(d_n2*((T_p0/1000)^3)))+...
    0.21*((a_ox)+(b_ox*(T_p0/1000))+(c_ox*((T_p0/1000)^2))+...
    (d_ox*((T_p0/1000)^3))))/(MW_p);
% Mach Number at Motive Nozzle Exit Plane
M_p1 = Mach_finder(eps,gamma_p,5);
% Motive Specific Gas Constant [J/(kg*K)]
R_p = R_u/MW_p;

%% DEFINING ENTRAINED FLOW VALUES

% Suction Stagnation Temperature [K]
T_s0 = 298;
```

```
% Suction Molecular Weight [kg/mol]
MW_s = 0.028;
% Suction Heat Capacity Ratio
gamma_s = 1.4;
% Suction Heat Capacity [J/K]
Cp_s = ((a_n2)+...
   (b_n2*(T_s0/1000))+...
   (c_n2*((T_s0/1000)^2))+...
   (d_n2*((T_s0/1000)^3)))/...
   (MW_s);
% Suction Specific Gas Constant [J/(kg*K)]
R_s = R_u/MW_s;

%% RUNNING THE CODE

% These vectors are defined so that only the experimental data points which
% yield a momentum coefficient between 0 and 1 are reflected in the fit.
success_n_m_vector = [];
success_P_exit_vector = zeros(1,length(P_p0_vector));
successful_run_index = [];

% Outer loop scans over all of the experimental data points
for j_2 = 1:length(P_p0_vector)

   % Current best values.  Exit pressure is main constraint, so initially
   % set to some arbitrarily high value.
   current_success_n_m = 0;
   current_success_mdot = 0;
   current_success_P_e = 101325*50;

   % Loading in values corresponding to current experimental data point
   P_p0 = P_p0_vector(j_2);
   P_s0 = P_s0_vector(j_2);
   mdot_s = mdot_s_vector(j_2);

   % Scanning over range of possible momentum coefficient value
   for j_1 = 1:length(n_m_vector)

      % Loading in current momentum coefficient value
      n_m = n_m_vector(j_1);

      % Loading all constant model input values into a struct
      ei.A_t = A_t;
      ei.T_p0 = T_p0;
      ei.P_p0 = P_p0;
      ei.Cp_p = Cp_p;
```

```
        ei.MW_p = MW_p;
        ei.gamma_p = gamma_p;
        ei.mdot_s = mdot_s;
        ei.T_s0 = T_s0;
        ei.P_s0 = P_s0;
        ei.Cp_s = Cp_s;
        ei.MW_s = MW_s;
        ei.gamma_s = gamma_s;
        ei.n_p = n_p;
        ei.M_p1 = M_p1;
        ei.R_p = R_p;
        ei.R_s = R_s;
        ei.A_3 = A_3;
        ei.n_m = n_m;
        ei.A_p1 = A_p1;
        ei.A_c = A_c;

        % Running model
        eo = new_model(ei);

        % Exit pressure must be higher than ambient (14.7 psia) for a run
        % to be successful
        if eo.P_e < 101325
            eo.P_e = 0;
            D_3 = 0;
            eo.mdot_p = 0;
        end

        % Choosing momentum coefficient value which yields exit pressure
        % JUST above ambient pressure
        if eo.P_e ~= 0
            if eo.P_e < current_success_P_e
                current_success_n_m = n_m;
                current_success_P_e = eo.P_e;
            end
        end
    end

    if current_success_P_e < 101325*50
        success_n_m_vector(j_2) = current_success_n_m;
        success_P_exit_vector(j_2) = current_success_P_e;
        successful_run_index = [successful_run_index, j_2];
    end
end

%% DEFINING ALL VALUES FOR FITTING AND GRAPHING
```

```
stg1_P_p0_vector_graph = P_p0_vector(successful_run_index)./6894.76;
stg1_P_p1_vector_graph = stg1_P_p0_vector_graph.*((1+((gamma_p-1)/2)*(M_p1^2))^...
   ((-gamma_p)/(gamma_p-1)));
stg1_mdot_s_vector_graph = mdot_s_vector(successful_run_index);
success_n_m_vector_graph = success_n_m_vector(successful_run_index);
success_P_exit_vector_graph = success_P_exit_vector(successful_run_index);
stg1_P_s0_vector_graph = P_s0_vector(successful_run_index);
stg1_P_mc_vector_graph = P_mc_vector(successful_run_index);
stg1_P_ratio_vector_graph = stg1_P_p1_vector_graph./stg1_P_mc_vector_graph;

stg1_P_p0_vector_col = stg1_P_p0_vector_graph.';
stg1_mdot_s_vector_col = stg1_mdot_s_vector_graph.';
success_n_m_vector_col = success_n_m_vector_graph.';
success_P_exit_vector_col = (success_P_exit_vector_graph.')./6894.7;
stg1_P_s0_vector_col = (stg1_P_s0_vector_graph.')./6894.7;
stg1_P_mc_vector_col = (stg1_P_mc_vector_graph.')./6894.7;
stg1_P_ratio_vector_col = stg1_P_ratio_vector_graph.';


%% PLOTTING DATA ALONG WITH CURVE FITS

% Creating Fit
[nm_fit,nm_gof] = createFit(stg1_P_p0_vector_graph, mdot_s_vector,
success_n_m_vector_graph);

figure(1)
hold on
scatter3(stg1_P_p0_vector_graph,stg1_mdot_s_vector_graph,success_n_m_vector_graph);
plot(nm_fit,[stg1_P_p0_vector_col,stg1_mdot_s_vector_col],success_n_m_vector_col);
hold off
xlabel('Motive Pressure (psia)');
ylabel('Suction Mass Flow Rate (kg/s)');
zlabel('Energy Efficiency Coefficient');
set(legend,'visible','off')
zlim([0 1]);
```

TEST_DATA_ANALYSIS_ SINGLE_STAGE_EJECTOR_8_5_EXP.M:

```
% This script is used to load experimental characterization data for the
% single-stage ejector with high expansion ratio nozzle.  The new 1-D model
% is then used to determine the momentum coefficient value that satisfies
% each of the experimentally defined data points.  The results momentum
% coefficient curve is then shown graphically.  Must have curve-fitting
% toolbox to run this script.
```

```
% Loading Data from Single-Stage Ejector Performance Characterization
test_data = xlsread('VE_8_5_Test_Results.xlsx',1,'A2:C178');
% Motive Stagnation Pressure [Pa]
P_p0_vector = ((test_data(:,1)).').*6894.75729;
% Suction Mass Flow Rate [kg/s]
mdot_s_vector = ((test_data(:,3)).')./2.20462262;
% Suction Stagnation Pressure [Pa]
P_s0_vector = ((test_data(:,2)).').*6894.75729;

%Typical isentropic efficiency for CD nozzle
n_p = 0.993;

% Initializing Momentum Coefficient Scanning Range
n_m_vector = 0.001:0.001:1;

%DEFINING GEOMETRY VALUES AND CONSTANT VALUES

% Constant Section Diameter [m]
D_3 = 2.15*0.0254;
% Constant Section Area [m^2]
A_3 = (pi)/(4)*((D_3)^2);
% Motive Nozzle Throat Diameter [m]
D_t = 0.495*0.0254;
% Motive Nozzle Throat Area [m^2]
A_t = pi/4*((D_t)^2);
% Motive Nozzle Exit Diameter [m]
D_p1 = 1.16*0.0254;
% Motive NOzzle Exit Area [m^2]
A_p1 = pi/4*((D_p1)^2);
% Motive Nozzle Expansion Ratio
eps = A_p1/A_t;
% Contraction Section Diameter [m]
D_c = 4*0.0254;
% Contraction Section Area [m^2]
A_c = pi/4*((D_c)^2);

% Coefficients Used for Heat Capacity Calaculation
a_ox = 28.186;
b_ox = 6.3011;
c_ox = -0.74986;
d_ox = 0;

% Coefficients Used for Heat Capacity Calculation
a_n2 = 27.336;
b_n2 = 6.23;
c_n2 = -0.95082;
```

```
d_n2 = 0;

% Universal Gas Constant [J/(K*mol)]
R_u = 8.314;

%% DEFINING MOTIVE FLOW VALUES

% Motive Stagnation Temperature [K]
T_p0 = 298;
% Motive Heat Capacity Ratio
gamma_p = 1.4;
% Motive Molecular Weight [kg/mol]
MW_p = 0.029;
% Motive Heat Capacity [J/K]
Cp_p = (0.79*((a_n2)+(b_n2*(T_p0/1000))+...
    (c_n2*((T_p0/1000)^2))+(d_n2*((T_p0/1000)^3)))+...
    0.21*((a_ox)+(b_ox*(T_p0/1000))+(c_ox*((T_p0/1000)^2))+...
    (d_ox*((T_p0/1000)^3))))/(MW_p);
% Mach Number at Motive Nozzle Exit Plane
M_p1 = Mach_finder(eps,gamma_p,5);
% Motive Specific Gas Constant [J/(kg*K)]
R_p = R_u/MW_p;

%% DEFINING ENTRAINED FLOW VALUES

% Suction Stagnation Temperature [K]
T_s0 = 298;
% Suction Molecular Weight [kg/mol]
MW_s = 0.028;
% Suction Heat Capacity Ratio
gamma_s = 1.4;
% Suction Heat Capacity [J/K]
Cp_s = ((a_n2)+...
    (b_n2*(T_s0/1000))+...
    (c_n2*((T_s0/1000)^2))+...
    (d_n2*((T_s0/1000)^3)))/...
    (MW_s);
% Suction Specific Gas Constant [J/(kg*K)]
R_s = R_u/MW_s;

%% RUNNING THE CODE

% These vectors are defined so that only the experimental data points which
% yield a momentum coefficient between 0 and 1 are reflected in the fit.
success_n_m_vector = [];
success_P_exit_vector = zeros(1,length(P_p0_vector));
```

```
successful_run_index = [];

% Outer loop scans over all of the experimental data points
for j_2 = 1:length(P_p0_vector)

    % Current best values.  Exit pressure is main constraint, so initially
    % set to some arbitrarily high value.
    current_success_n_m = 0;
    current_success_mdot = 0;
    current_success_P_e = 101325*50;

    % Loading in values corresponding to current experimental data point
    P_p0 = P_p0_vector(j_2);
    P_s0 = P_s0_vector(j_2);
    mdot_s = mdot_s_vector(j_2);

    % Scanning over range of possible momentum coefficient value
    for j_1 = 1:length(n_m_vector)

        % Loading in current momentum coefficient value
        n_m = n_m_vector(j_1);

        % Loading all constant model input values into a struct
        ei.A_t = A_t;
        ei.T_p0 = T_p0;
        ei.P_p0 = P_p0;
        ei.Cp_p = Cp_p;
        ei.MW_p = MW_p;
        ei.gamma_p = gamma_p;
        ei.mdot_s = mdot_s;
        ei.T_s0 = T_s0;
        ei.P_s0 = P_s0;
        ei.Cp_s = Cp_s;
        ei.MW_s = MW_s;
        ei.gamma_s = gamma_s;
        ei.n_p = n_p;
        ei.M_p1 = M_p1;
        ei.R_p = R_p;
        ei.R_s = R_s;
        ei.A_3 = A_3;
        ei.n_m = n_m;
        ei.A_p1 = A_p1;
        ei.A_c = A_c;

        % Running model
        eo = new_model(ei);
```

```
        % Exit pressure must be higher than ambient (14.7 psia) for a run
        % to be successful
        if eo.P_e < 101325
            eo.P_e = 0;
            D_3 = 0;
            eo.mdot_p = 0;
        end

        % Choosing momentum coefficient value which yields exit pressure
        % JUST above ambient pressure
        if eo.P_e ~= 0
            if eo.P_e < current_success_P_e
                current_success_n_m = n_m;
                current_success_P_e = eo.P_e;
            end
        end
    end

    if current_success_P_e < 101325*50
        success_n_m_vector(j_2) = current_success_n_m;
        success_P_exit_vector(j_2) = current_success_P_e;
        successful_run_index = [successful_run_index, j_2];
        passed = passed + 1
    else
        failed_run_index = [failed_run_index, j_2];
        failed = failed + 1
    end
end

%% DEFINING ALL VALUES FOR FITTING AND GRAPHING

stg1_P_p0_vector_graph = P_p0_vector(successful_run_index)./6894.76;
stg1_P_p1_vector_graph = stg1_P_p0_vector_graph.*((1+((gamma_p-1)/2)*(M_p1^2))^...
    ((-gamma_p)/(gamma_p-1)));
stg1_mdot_s_vector_graph = mdot_s_vector(successful_run_index);
success_n_m_vector_graph = success_n_m_vector(successful_run_index);
success_P_exit_vector_graph = success_P_exit_vector(successful_run_index);
stg1_P_s0_vector_graph = P_s0_vector(successful_run_index);

stg1_P_p0_vector_col = stg1_P_p0_vector_graph.';
stg1_mdot_s_vector_col = stg1_mdot_s_vector_graph.';
success_n_m_vector_col = success_n_m_vector_graph.';
success_P_exit_vector_col = (success_P_exit_vector_graph.')./6894.7;
stg1_P_s0_vector_col = (stg1_P_s0_vector_graph.')./6894.7;
```

```
%% PLOTTING DATA ALONG WITH CURVE FITS

% Creating Fit
[nm_fit,nm_gof] = createFit(stg1_P_p0_vector_graph, mdot_s_vector,
success_n_m_vector_graph);

figure(1)
hold on
scatter3(stg1_P_p0_vector_graph,stg1_mdot_s_vector_graph,success_n_m_vector_graph);
plot(nm_fit,[stg1_P_p0_vector_col,stg1_mdot_s_vector_col],success_n_m_vector_col);
hold off
xlabel('Motive Pressure (psia)');
ylabel('Suction Mass Flow Rate (kg/s)');
zlabel('Energy Efficiency Coefficient');
set(legend,'visible','off')
zlim([0 1]);
```

TEST_DATA_ANALYSIS_ SINGLE_STAGE_EJECTOR_F50_MOTOR.M:

```
% This script is used to load experimental characterization data for the
% single-stage ejector with original nozzle during the testing of a small
% solid rocket motor within the altitude chamber.  The new 1-D model is then
% used to determine the momentum coefficient value that satisfies each
% of the experimentally defined data points.  The resulting momentum
% coefficient curve is then shown graphically.

%% Determining the Isp of the motor

% Defining thrust curve for F50-9T motor, taken from Aerotech website
time_step = 0.1;
f50_time_vector = 0:time_step:1.5;
f50_thrust_vector = [72,70.5,70,69.5,68,67,64,61,56.5,51.5,43,25,6,2,1,0];

f50_time_vector_col = f50_time_vector.';
f50_thrust_vector_col = f50_thrust_vector.';

plot(f50_time_vector,f50_thrust_vector);

% Creating a fit for interpolation
f50_thrust_fit = fit(f50_time_vector_col,f50_thrust_vector_col,'poly7');

plot(f50_thrust_fit,f50_time_vector_col,f50_thrust_vector_col);

% Determine Isp such that thrust and mass flow are true
Isp = 130; %s
```

```
total_prop_mass_available = 54.25/1000;
gravity = 9.81;

% Determining exhaust mass flow curve
f50_mass_flow_vector = f50_thrust_vector./((gravity).*(Isp));

% Validating Isp value
total_prop_mass = 0;

for integr_index = 1:size(f50_mass_flow_vector,2)-1
   avg_mass_flow =
(f50_mass_flow_vector(integr_index)+f50_mass_flow_vector(integr_index+1))/2;
   total_prop_mass = total_prop_mass + ((time_step)*(avg_mass_flow));
end

disp(total_prop_mass);
disp(total_prop_mass_available);

%% Determining the steady state temperature of the exhaust flow

% Determining the assymptotic temperature approach
f_50_temp_vector = [380,615,810,960,1085,1175];
f_50_temp_time_vector = [148,148.2,148.4,148.6,148.8,149];

f_50_temp_vector_col = f_50_temp_vector.';
f_50_temp_time_vector_col = f_50_temp_time_vector.';

plot(f_50_temp_time_vector,f_50_temp_vector);

f50_temp_fit = fit(f_50_temp_time_vector_col,f_50_temp_vector_col,'poly2');

x_temp_graphing_vector = 100:0.01:200;

y_temp_graphing_vector = (-500)./(x_temp_graphing_vector-147.5)+1500;

figure(1)
plot(x_temp_graphing_vector,y_temp_graphing_vector);
hold on
scatter(f_50_temp_time_vector,f_50_temp_vector);
title('Projected Temperature vs Time');
xlabel('Time (sec)');
ylabel('Temperature (k)');
xlim([146 170]);
ylim([200 1700]);

%% Code to evaluate the test firing data points
```

```
% Typical efficiency for CD nozzle
ei.n_p = 0.993;

% Defining full range of potential momentum coefficient values
n_m_vector = 0.001:0.001:1;
% Experimental run time
time_vector = 147.85:0.1:149.35;

%DEFINING GEOMETRY VALUES AND CONSTANT VALUES

% Constant Section Diameter [m]
D_3 = 2.15 * 0.0254;
% Constant Section Area [m^2]
ei.A_3 = (pi)/(4)*((D_3)^2);
% Motive Nozzle Throat Diameter [m]
D_t = 0.495 * 0.0254;
% Motive Nozzle Throat Area [m^2]
ei.A_t = pi/4*((D_t)^2);
% Motive Nozzle Exit Diameter [m]
D_e = 1.16*0.0254;
% Motive NOzzle Exit Area [m^2]
ei.A_p1 = pi/4*((D_e)^2);
% Motive Nozzle Expansion Ratio
eps = ei.A_p1/ei.A_t;
% Contraction Section Diameter [m]
D_c = 4*0.0254;
% Contraction Section Area [m^2]
ei.A_c = pi/4*((D_c)^2);

% Universal Gas Constant [J/(K*mol)]
R_u = 8.314;

% Coefficients Used for Heat Capacity Calaculation
a_ox = 28.186;
b_ox = 6.3011;
c_ox = -0.74986;
d_ox = 0;

a_n2 = 27.336;
b_n2 = 6.23;
c_n2 = -0.95082;
d_n2 = 0;

%DEFINING MOTIVE FLOW VALUES
```

```
% Motive Stagnation Temperature [K]
ei.T_p0 = 298;
% Motive Heat Capacity Ratio
ei.gamma_p = 1.4;
% Motive Molecular Weight [kg/mol]
ei.MW_p = 0.029;
% Motive Heat Capacity [J/K]
ei.Cp_p = (0.79*((a_n2)+(b_n2*(ei.T_p0/1000))+...
   (c_n2*((ei.T_p0/1000)^2))+(d_n2*((ei.T_p0/1000)^3)))+...
   0.21*((a_ox)+(b_ox*(ei.T_p0/1000))+(c_ox*((ei.T_p0/1000)^2))+...
   (d_ox*((ei.T_p0/1000)^3))))/(ei.MW_p);
% Mach Number at Motive Nozzle Exit Plane
ei.M_p1 = Mach_finder(eps,ei.gamma_p,5);
% Motive Specific Gas Constant [J/(kg*K)]
ei.R_p = R_u/ei.MW_p;
% Defining Motive Stagnation Pressure [Pa}
P_p0_vector = (167*6894.7).*(ones(size(f50_mass_flow_vector,2)));
% Calculating Motive Mass Flow Rate [kg/s]
mdot_p = (P_p0_vector(1))*(ei.A_t)*...
   sqrt(((ei.gamma_p/ei.R_p)*((2/(ei.gamma_p+1))^...
   ((ei.gamma_p+1)/(ei.gamma_p-1))))*(ei.n_p)/(ei.T_p0));

%DEFINING ENTRAINED FLOW VALUES

% Suction Stagnation Temperature [K]
ei.T_s0 = 1500;
% Suction Molecular Weight [kg/mol]
ei.MW_s = 0.02304;
% Suction Heat Capacity Ratio
ei.gamma_s = 1.278;
% Suction Specific Gas Constant [J/(kg*K)]
ei.R_s = R_u/ei.MW_s;
% Suction Heat Capacity [J/K]
ei.Cp_s = ((ei.gamma_s)*(ei.R_s))/(ei.gamma_s-1);
% Defining Response of Suction Stagnation Pressure During Testing
P_s0_vector_psi = [8.35,8.35,8.35,8.35,8.35,8.35,8.35,8.32,8.25,8.1,...
   7.85,7.7,7.5,7.45,7.42,7.4];
P_s0_vector = P_s0_vector_psi.*6894.7;
% Converting to Equivalent Nitrogen Mass Flow Rate [kg/s]
mdot_s_vector = f50_mass_flow_vector.*(ei.T_s0./298).*(ei.MW_p./ei.MW_s);

figure(2)
yyaxis left;
plot(time_vector,f50_mass_flow_vector);
xlabel('Time (sec)');
ylabel('Entrained Mass Flow (kg/sec)');
```

```
title('Comparing Entrained Pressure/Mass Flow Curves F50-6T');
yyaxis right;
plot(time_vector,P_s0_vector);
ylabel('Entrained Pressure (psia)');

success_n_m_vector = zeros(1,size(f50_mass_flow_vector,2));
success_pressure_exit_vector = zeros(1,size(f50_mass_flow_vector,2));

successful_run_index = [];

% Equivalent Nitrogen Mass Flow Rate Fluid Characteristics
ei.T_s0 = ei.T_p0;  %from fit of temp data
ei.MW_s = ei.MW_p; %from data sheet for grain
ei.gamma_s = ei.gamma_p; %from Data Sheet for grain
ei.R_s = R_u/ei.MW_p;
ei.Cp_s = ((ei.gamma_p)*(ei.R_p))/(ei.gamma_p-1);

% Scanning Over Range of POtential Suction Mass Flow Rate Values
for j_2 = 1:length(mdot_s_vector)

    % Current best values.  Exit pressure is main constraint, so initially
    % set to some arbitrarily high value.
    current_success_n_m = 0;
    current_success_pressure_exit = 101325*50;

    % Loading in values corresponding to current experimental data point
    ei.P_p0 = P_p0_vector(j_2);
    ei.P_s0 = P_s0_vector(j_2);
    ei.mdot_s = mdot_s_vector(j_2);

    % Scanning over range of possible momentum coefficient value
    for j_1 = 1:size(n_m_vector,2)

        % Loading in current momentum coefficient value
        ei.n_m = n_m_vector(j_1);

        % Running model
        eo = new_model(ei);

        % Exit pressure must be higher than ambient (14.7 psia) for a run
        % to be successful
        if eo.P_e < 101325
            eo.P_e = 0;
            D_3 = 0;
            eo.mdot_p = 0;
        end
```

```
        % Choosing momentum coefficient value which yields exit pressure
        % JUST above ambient pressure
        if eo.P_e ~= 0
            if eo.P_e < current_success_pressure_exit
                current_success_n_m = ei.n_m;
                current_success_pressure_exit = eo.P_e;
            end
        end
    end
    if current_success_pressure_exit < 101325*40
        success_n_m_vector(j_2) = current_success_n_m;
        success_pressure_exit_vector(j_2) = current_success_pressure_exit;
        successful_run_index = [successful_run_index, j_2];
    end
end

% Preparing for Graphing
P_p0_vector_psi = P_p0_vector(successful_run_index)./6894.76;
mdot_s_vector_graph = mdot_s_vector(successful_run_index);
success_n_m_vector_graph = success_n_m_vector(successful_run_index);
success_P_e_vector_graph = success_pressure_exit_vector(successful_run_index)./6894.76;
P_s0_vector_graphing = P_s0_vector(successful_run_index);

figure(5)
scatter3(P_p0_vector_psi,mdot_s_vector_graph,success_n_m_vector_graph);

figure(3)
scatter(mdot_s_vector_graph,P_s0_vector_graphing);

figure(4)
hold on
stem3(P_p0_vector_psi,mdot_s_vector_graph,P_s0_vector_psi);

figure(9)
hold on
stem3(P_p0_vector_psi,mdot_s_vector_graph,success_n_m_vector_graph);
```

TEST_DATA_ANALYSIS_SINGLE_STAGE_EJECTOR_ORIGINAL_NOZZLE.M:

```
% This script is used to load experimental characterization data for the
% single-stage ejector with original nozzle.  The new 1-D model is then
% used to determine the momentum coefficient value that satisfies each
% of the experimentally defined data points.  The resulting momentum
% coefficient curve is then shown graphically.  Must have curve-fitting
% toolbox to run this script.
```

```
% Loading Data from Single-Stage Ejector Performance Characterization
test_data = xlsread('VE_Test_Results.xlsx',2,'C2:G166');
% Motive Stagnation Pressure [Pa]
P_p0_vector = ((test_data(:,1)).').*6894.75729;
% Motive Mass Flow Rate [kg/s]
mdot_p_vector = ((test_data(:,2)).')./2.20462262;
% Suction Mass Flow Rate [kg/s]
mdot_s_vector = ((test_data(:,3)).')./2.20462262;
% Suction Stagnation Pressure [Pa]
P_s0_vector = ((test_data(:,4)).').*6894.75729;
% Mixing Chamber Static Pressure [Pa]
P_mc_vector = ((test_data(:,5)).').*6894.75729;

%Typical isentropic efficiency for CD nozzle
n_p = 0.993;

% Initializing Momentum Coefficient Scanning Range
n_m_vector = 0.001:0.001:1;

% DEFINING GEOMETRY VALUES AND CONSTANT VALUES

% Constant Section Diameter [m]
D_3 = 2.15*0.0254;
% Constant Section Area [m^2]
A_3 = (pi)/(4)*((D_3)^2);
% Motive Nozzle Throat Diameter [m]
D_t = 0.495*0.0254;
% Motive Nozzle Throat Area [m^2]
A_t = pi/4*((D_t)^2);
% Motive Nozzle Exit Diameter [m]
D_p1 = 1.16*0.0254;
% Motive NOzzle Exit Area [m^2]
A_p1 = pi/4*((D_p1)^2);
% Motive Nozzle Expansion Ratio
eps = A_p1/A_t;
% Contraction Section Diameter [m]
D_c = 4*0.0254;
% Contraction Section Area [m^2]
A_c = pi/4*((D_c)^2);

% Coefficients Used for Heat Capacity Calaculation
a_ox = 28.186;
b_ox = 6.3011;
c_ox = -0.74986;
d_ox = 0;
```

```
% Coefficients Used for Heat Capacity Calculation
a_n2 = 27.336;
b_n2 = 6.23;
c_n2 = -0.95082;
d_n2 = 0;

% Universal Gas Constant [J/(K*mol)]
R_u = 8.314;

%% DEFINING MOTIVE FLOW VALUES

% Motive Stagnation Temperature [K]
T_p0 = 298;
% Motive Heat Capacity Ratio
gamma_p = 1.4;
% Motive Molecular Weight [kg/mol]
MW_p = 0.029;
% Motive Heat Capacity [J/K]
Cp_p = (0.79*((a_n2)+(b_n2*(T_p0/1000))+...
    (c_n2*((T_p0/1000)^2))+(d_n2*((T_p0/1000)^3)))+...
    0.21*((a_ox)+(b_ox*(T_p0/1000))+(c_ox*((T_p0/1000)^2))+...
    (d_ox*((T_p0/1000)^3))))/(MW_p);
% Mach Number at Motive Nozzle Exit Plane
M_p1 = Mach_finder(eps,gamma_p,5);
% Motive Specific Gas Constant [J/(kg*K)]
R_p = R_u/MW_p;

%% DEFINING ENTRAINED FLOW VALUES

% Suction Stagnation Temperature [K]
T_s0 = 298;
% Suction Molecular Weight [kg/mol]
MW_s = 0.028;
% Suction Heat Capacity Ratio
gamma_s = 1.4;
% Suction Heat Capacity [J/K]
Cp_s = ((a_n2)+...
    (b_n2*(T_s0/1000))+...
    (c_n2*((T_s0/1000)^2))+...
    (d_n2*((T_s0/1000)^3)))/...
    (MW_s);
% Suction Specific Gas Constant [J/(kg*K)]
R_s = R_u/MW_s;

%% RUNNING THE CODE
```

```
% These vectors are defined so that only the experimental data points which
% yield a momentum coefficient between 0 and 1 are reflected in the fit.
success_n_m_vector = [];
success_P_exit_vector = zeros(1,length(P_p0_vector));
successful_run_index = [];

% Outer loop scans over all of the experimental data points
for j_2 = 1:length(P_p0_vector)

    % Current best values.  Exit pressure is main constraint, so initially
    % set to some arbitrarily high value.
    current_success_n_m = 0;
    current_success_mdot = 0;
    current_success_P_e = 101325*50;

    % Loading in values corresponding to current experimental data point
    P_p0 = P_p0_vector(j_2);
    P_s0 = P_s0_vector(j_2);
    mdot_s = mdot_s_vector(j_2);

    % Scanning over range of possible momentum coefficient values
    for j_1 = 1:length(n_m_vector)

        % Loading in current momentum coefficient value
        n_m = n_m_vector(j_1);

        % Loading all constant model input values into a struct
        ei.A_t = A_t;
        ei.T_p0 = T_p0;
        ei.P_p0 = P_p0;
        ei.Cp_p = Cp_p;
        ei.MW_p = MW_p;
        ei.gamma_p = gamma_p;
        ei.mdot_s = mdot_s;
        ei.T_s0 = T_s0;
        ei.P_s0 = P_s0;
        ei.Cp_s = Cp_s;
        ei.MW_s = MW_s;
        ei.gamma_s = gamma_s;
        ei.n_p = n_p;
        ei.M_p1 = M_p1;
        ei.R_p = R_p;
        ei.R_s = R_s;
        ei.A_3 = A_3;
        ei.n_m = n_m;
        ei.A_p1 = A_p1;
```

```
        ei.A_c = A_c;

        % Running model
        eo = new_model(ei);

        % Exit pressure must be higher than ambient (14.7 psia) for a run
        % to be successful
        if eo.P_e < 101325
            eo.P_e = 0;
            D_3 = 0;
            eo.mdot_p = 0;
        end
        % Choosing momentum coefficient value which yields exit pressure
        % JUST above ambient pressure
        if eo.P_e ~= 0
            if eo.P_e < current_success_P_e
                current_success_n_m = n_m;
                current_success_P_e = eo.P_e;
            end
        end
    end

    if current_success_P_e < 101325*50
        success_n_m_vector(j_2) = current_success_n_m;
        success_P_exit_vector(j_2) = current_success_P_e;
        successful_run_index = [successful_run_index, j_2];
    end
end

%% DEFINING ALL VALUES FOR FITTING AND GRAPHING

stg1_P_p0_vector_graph = P_p0_vector(successful_run_index)./6894.76;
stg1_P_p1_vector_graph = stg1_P_p0_vector_graph.*((1+((gamma_p-1)/2)*(M_p1^2))^...
    ((-gamma_p)/(gamma_p-1)));
stg1_mdot_s_vector_graph = mdot_s_vector(successful_run_index);
success_n_m_vector_graph = success_n_m_vector(successful_run_index);
success_P_exit_vector_graph = success_P_exit_vector(successful_run_index);
stg1_P_s0_vector_graph = P_s0_vector(successful_run_index);
stg1_P_mc_vector_graph = P_mc_vector(successful_run_index);
stg1_P_ratio_vector_graph = stg1_P_p1_vector_graph./stg1_P_mc_vector_graph;
stg1_mdot_p_vector_graph = mdot_p_vector(successful_run_index);

stg1_P_p0_vector_col = stg1_P_p0_vector_graph.';
stg1_mdot_s_vector_col = stg1_mdot_s_vector_graph.';
success_n_m_vector_col = success_n_m_vector_graph.';
success_P_exit_vector_col = (success_P_exit_vector_graph.')./6894.7;
```

```
stg1_P_s0_vector_col = (stg1_P_s0_vector_graph.')./6894.7;
stg1_P_mc_vector_col = (stg1_P_mc_vector_graph.')./6894.7;
stg1_P_ratio_vector_col = stg1_P_ratio_vector_graph.';


%% PLOTTING DATA ALONG WITH CURVE FITS

% Creating Fit
[nm_fit,nm_gof] = createFit(stg1_P_p0_vector_graph, stg1_mdot_s_vector_graph,
success_n_m_vector_graph);
% Saving Fit
save('single_stage_fit.mat','nm_fit','nm_gof','stg1_P_p0_vector_graph','mdot_s_vector','success_
n_m_vector_graph');

figure(5)
hold on
scatter3(stg1_P_p0_vector_graph,stg1_mdot_s_vector_graph,success_n_m_vector_graph);
plot(nm_fit,[stg1_P_p0_vector_col,stg1_mdot_s_vector_col],success_n_m_vector_col);
hold off
xlabel('Motive Pressure (psia)');
ylabel('Suction Mass Flow Rate (kg/s)');
zlabel('Energy Efficiency Coefficient');
set(legend,'visible','off')
zlim([0 1]);
```

TEST_DATA_ANALYSIS_TWO_STAGE_EJECTOR.M:

```
% This script is used to load experimental characterization data for the
% two-stage ejector.  The new 1-D model is then used to determine the
% momentum coefficient value for each stage that satisfies each
% of the experimentally defined data points.  The resulting momentum
% coefficient curve is then shown graphically.  Must have curve-fitting
% toolbox to run this script.

%% DEFINING GAS CONSTANTS

% Coefficients Used for Heat Capacity Calaculation
a_ox = 28.186;
b_ox = 6.3011;
c_ox = -0.74986;
d_ox = 0;

a_n2 = 27.336;
b_n2 = 6.23;
c_n2 = -0.95082;
d_n2 = 0;
```

```
% Universal Gas Constant [J/(K*mol)]
R_u = 8.314;

%Typical isentropic efficiency for CD nozzle
stg1_n_p = 0.993;
stg2_n_p = 0.993;

% Initializing Momentum Coefficient Scanning Range
n_m_vector = 0.001:0.001:1;

%% DEFINING 1ST STAGE MOTIVE CONDITIONS

% Defining 1st Stage Geometrical Parameters

% Constant Section Diameter [m]
stg1_D_3 = 2.65*0.0254;
% Constant Section Area [m^2]
stg1_A_3 = (pi)/(4)*((stg1_D_3)^2);
% Motive Nozzle Throat Diameter [m]
stg1_D_t = 0.355*0.0254;
% Motive Nozzle Throat Area [m^2]
stg1_A_t = pi/4*((stg1_D_t)^2);
% Motive Nozzle Exit Diameter [m]
stg1_D_p1 = 0.5*0.0254;
% Motive NOzzle Exit Area [m^2]
stg1_A_p1 = pi/4*((stg1_D_p1)^2);
% Motive Nozzle Expansion Ratio
stg1_eps = stg1_A_p1/stg1_A_t;
% Contraction Section Diameter [m]
stg1_D_c = 6*0.0254;
% Contraction Section Area [m^2]
stg1_A_c = pi/4*((stg1_D_c)^2);

%% DEFINING 2ST STAGE MOTIVE FLOW VALUES

% Motive Stagnation Pressure [Pa]
stg1_P_p0 = 500*6894.76;
% Motive Stagnation Temperature [K]
stg1_T_p0 = 298;
% Motive Heat Capacity Ratio
stg1_gamma_p = 1.4;
% Motive Molecular Weight [kg/mol]
stg1_MW_p = 0.029;
% Motive Heat Capacity [J/K]
stg1_Cp_p = (0.79*((a_n2)+(b_n2*(stg1_T_p0/1000))+...
```

```
    (c_n2*((stg1_T_p0/1000)^2))+(d_n2*((stg1_T_p0/1000)^3)))+...
    0.21*((a_ox)+(b_ox*(stg1_T_p0/1000))+(c_ox*((stg1_T_p0/1000)^2))+...
    (d_ox*((stg1_T_p0/1000)^3))))/(stg1_MW_p);
% Mach Number at Motive Nozzle Exit Plane
stg1_M_p1 = Mach_finder(stg1_eps,stg1_gamma_p,5);
% Motive Specific Gas Constant [J/(kg*K)]
stg1_R_p = R_u/stg1_MW_p; % J/(kg*K)
% Motive Mass Flow Rate [kg/s]
stg1_mdot_p = (stg1_P_p0)*(stg1_A_t)*...
    sqrt(((stg1_gamma_p/stg1_R_p)*((2/(stg1_gamma_p+1))^...
    ((stg1_gamma_p+1)/(stg1_gamma_p-1))))*(stg1_n_p)/(stg1_T_p0));

%% DEFINING 2ND STAGE MOTIVE CONDITIONS

% Defining 2nd Stage Geometrical Parameters

% Constant Section Diameter [m]
stg2_D_3 = 3*0.0254;
% Constant Section Area [m^2]
stg2_A_3 = (pi)/(4)*((stg2_D_3)^2);
% Motive Nozzle Throat Diameter [m]
stg2_D_t = 0.654*0.0254;
% Motive Nozzle Throat Area [m^2]
stg2_A_t = pi/4*((stg2_D_t)^2);
% Motive Nozzle Exit Diameter [m]
stg2_D_p1 = 1.25*0.0254;
% Motive NOzzle Exit Area [m^2]
stg2_A_p1 = pi/4*((stg2_D_p1)^2);
% Motive Nozzle Expansion Ratio
stg2_eps = stg2_A_p1/stg2_A_t;
% Contraction Section Diameter [m]
stg2_D_c = 6.5*0.0254;
% Contraction Section Area [m^2]
stg2_A_c = pi/4*((stg2_D_c)^2);

% Defining 2nd Stage Motive Flow Values

% Motive Stagnation Pressure [Pa]
stg2_P_p0 = 500*6894.76;
% Motive Stagnation Temperature [K]
stg2_T_p0 = 298;
% Motive Heat Capacity Ratio
stg2_gamma_p = 1.4;
% Motive Molecular Weight [kg/mol]
stg2_MW_p = 0.029;
% Motive Heat Capacity [J/K]
```

```
stg2_Cp_p = (0.79*((a_n2)+(b_n2*(stg2_T_p0/1000))+...
   (c_n2*((stg2_T_p0/1000)^2))+(d_n2*((stg2_T_p0/1000)^3)))+...
   0.21*((a_ox)+(b_ox*(stg2_T_p0/1000))+(c_ox*((stg2_T_p0/1000)^2))+...
   (d_ox*((stg2_T_p0/1000)^3))))/(stg2_MW_p);
% Mach Number at Motive Nozzle Exit Plane
stg2_M_p1 = Mach_finder(stg2_eps,stg2_gamma_p,5);
% Motive Specific Gas Constant [J/(kg*K)]
stg2_R_p = R_u/stg2_MW_p;
% Motive Mass Flow Rate [kg/s]
stg2_mdot_p = (stg2_P_p0)*(stg2_A_t)*...
   sqrt(((stg2_gamma_p/stg2_R_p)*((2/(stg2_gamma_p+1))^...
   ((stg2_gamma_p+1)/(stg2_gamma_p-1))))*(stg2_n_p)/(stg2_T_p0));

%% DEFINING 1ST STAGE SUCTION CONDITIONS

% Suction Stagnation Temperature [K]
stg1_T_s0 = 298;
% Suction Molecular Weight [kg/mol]
stg1_MW_s = 0.028;
% Suction Heat Capacity Ratio
stg1_gamma_s = 1.4;
% Suction Heat Capacity [J/K]
stg1_Cp_s = ((a_n2)+...
   (b_n2*(stg1_T_s0/1000))+...
   (c_n2*((stg1_T_s0/1000)^2))+...
   (d_n2*((stg1_T_s0/1000)^3)))/...
   (stg1_MW_s);
% Suction Specific Gas Constant [J/(kg*K)]
stg1_R_s = R_u/stg1_MW_s;

% Suction Mass Flow Rate [kg/s]
stg1_mdot_s_vector = ([0.021463893, 0.045552867, 0.070780662, 0.09481173,...
   0.144939185, 0.194757808, 0.246680355, 0.294935511, 0.345506914,...
   0.395885297, 0.446070658, 0.496063])./2.205;

% Suction Stagnation Pressure [Pa]
stg1_P_s0_vector = ([0.205, 0.275, 0.328, 0.396, 0.489, 0.601, 0.914,...
   1.101, 1.267, 1.449, 1.619, 1.808]).*6894.75729;

%% DEFINING 2ND STAGE SUCTION CONDITIONS

% Suction Stagnation Temperature [K]
stg2_T_s0 = 298;
% Suction Molecular Weight [kg/mol]
stg2_MW_s = 0.028;
% Suction Heat Capacity Ratio
```

```
stg2_gamma_s = 1.4;
% Suction Heat Capacity [J/K]
stg2_Cp_s = ((a_n2)+...
   (b_n2*(stg2_T_s0/1000))+...
   (c_n2*((stg2_T_s0/1000)^2))+...
   (d_n2*((stg2_T_s0/1000)^3)))/...
   (stg2_MW_s);
% Suction Specific Gas Constant [J/(kg*K)]
stg2_R_s = R_u/stg2_MW_s;
% Suction Mass Flow Rate [kg/s]
stg2_mdot_s_vector = stg1_mdot_p+stg1_mdot_s_vector;
% Suction Stagnation Pressure [Pa]
stg2_P_s0_vector = ([4.391, 4.345, 4.226, 4.186, 4.16, 4.225, 4.335,...
   4.502, 4.716, 4.798, 4.99, 5.26]).*6894.75729;

%% RUNNING SCRIPT FOR 1ST STAGE

% Initializing vectors to store successful values
stg1_success_n_m_vector = [];
stg1_success_P_e_vector = [];
stg1_successful_run_index = [];

for j_2 = 1:length(stg1_mdot_s_vector)

   % Exit Pressure Initially Set to Arbitrarily High Value
   stg1_cs_P_e = 101325*50;

   % Loading in values corresponding to current experimental data point
   stg1_P_s0 = stg1_P_s0_vector(j_2);
   stg1_mdot_s = stg1_mdot_s_vector(j_2);
   stg1_P_e = stg2_P_s0_vector(j_2);

   % Scanning over range of possible momentum coefficient values
   for j_1 = 1:length(n_m_vector)

      % Loading in current momentum coefficient value
      n_m = n_m_vector(j_1);

      % Loading all Relevant Input Values
      ei.A_t = stg1_A_t;
      ei.T_p0 = stg1_T_p0;
      ei.P_p0 = stg1_P_p0;
      ei.Cp_p = stg1_Cp_p;
      ei.MW_p = stg1_MW_p;
      ei.gamma_p = stg1_gamma_p;
      ei.mdot_s = stg1_mdot_s;
```

```
        ei.T_s0 = stg1_T_s0;
        ei.P_s0 = stg1_P_s0;
        ei.Cp_s = stg1_Cp_s;
        ei.MW_s = stg1_MW_s;
        ei.gamma_s = stg1_gamma_s;
        ei.n_p = stg1_n_p;
        ei.M_p1 = stg1_M_p1;
        ei.R_p = stg1_R_p;
        ei.R_s = stg1_R_s;
        ei.A_3 = stg1_A_3;
        ei.n_m = n_m;
        ei.A_p1 = stg1_A_p1;
        ei.A_c = stg1_A_c;

        % Running model
        eo = new_model(ei);

        % Exit pressure must be higher than ambient (14.7 psia) for a run
        % to be successful
        if eo.P_e < stg1_P_e
            eo.P_e = 0;
        end
        % Choosing momentum coefficient value which yields exit pressure
        % JUST above ambient pressure
        if eo.P_e ~= 0
            if eo.P_e < stg1_cs_P_e
                stg1_cs_n_m = n_m;
                stg1_cs_P_e = eo.P_e;
            end
        end
    end

    if stg1_cs_P_e < 101325*50
        stg1_success_n_m_vector(j_2) = stg1_cs_n_m;
        stg1_success_P_e_vector(j_2) = stg1_cs_P_e;
        stg1_successful_run_index = [stg1_successful_run_index, j_2];
    end
end

%% DEFINING ALL OUTPUT VALUES FOR 1ST STAGE

stg1_mdot_s_vector_graph = stg1_mdot_s_vector(stg1_successful_run_index);
stg1_P_p0_graph = ones(1,length(stg1_mdot_s_vector_graph)).*stg1_P_p0./6894.76;
stg1_success_n_m_vector_graph = stg1_success_n_m_vector(stg1_successful_run_index);
stg1_success_P_exit_vector_graph = stg1_success_P_e_vector(stg1_successful_run_index);
stg1_P_s0_vector_graph = stg1_P_s0_vector(stg1_successful_run_index)./6894.76;
```

```
%% RUNNING SCRIPT FOR 1ST STAGE

% Initializing vectors to store successful values
stg2_success_n_m_vector = [];
stg2_success_P_e_vector = [];
stg2_successful_run_index = [];

for j_2 = 1:length(stg2_mdot_s_vector)

    % Exit Pressure Initially Set to Arbitrarily High Value
    stg2_cs_P_e = 101325*50;

    % Loading in values corresponding to current experimental data point
    stg2_P_s0 = stg2_P_s0_vector(j_2);
    stg2_mdot_s = stg2_mdot_s_vector(j_2);

    % Scanning over range of possible momentum coefficient values
    for j_1 = 1:length(n_m_vector)

        % Loading in current momentum coefficient value
        n_m = n_m_vector(j_1);

        % Loading all Relevant Input Values
        ei.A_t = stg2_A_t;
        ei.T_p0 = stg2_T_p0;
        ei.P_p0 = stg2_P_p0;
        ei.Cp_p = stg2_Cp_p;
        ei.MW_p = stg2_MW_p;
        ei.gamma_p = stg2_gamma_p;
        ei.mdot_s = stg2_mdot_s;
        ei.T_s0 = stg2_T_s0;
        ei.P_s0 = stg2_P_s0;
        ei.Cp_s = stg2_Cp_s;
        ei.MW_s = stg2_MW_s;
        ei.gamma_s = stg2_gamma_s;
        ei.n_p = stg2_n_p;
        ei.M_p1 = stg2_M_p1;
        ei.R_p = stg2_R_p;
        ei.R_s = stg2_R_s;
        ei.A_3 = stg2_A_3;
        ei.n_m = n_m;
        ei.A_p1 = stg2_A_p1;
        ei.A_c = stg2_A_c;

        % Running model
```

```
        eo = new_model(ei);

        % Exit pressure must be higher than ambient (14.7 psia) for a run
        % to be successful
        if eo.P_e < 101325
            eo.P_e = 0;
        end
        % Choosing momentum coefficient value which yields exit pressure
        % JUST above ambient pressure
        if eo.P_e ~= 0
            if eo.P_e < stg2_cs_P_e
                stg2_cs_n_m = n_m;
                stg2_cs_P_e = eo.P_e;
            end
        end
    end

    if stg2_cs_P_e < 101325*50
        stg2_success_n_m_vector(j_2) = stg2_cs_n_m;
        stg2_success_P_e_vector(j_2) = stg2_cs_P_e;
        stg2_successful_run_index = [stg2_successful_run_index, j_2];
    end
end

%% DEFINING ALL OUTPUT VALUES FOR 1ST STAGE

stg2_mdot_s_vector_graph = stg2_mdot_s_vector(stg2_successful_run_index);
stg2_P_p0_graph = ones(1,length(stg2_mdot_s_vector_graph)).*stg2_P_p0./6894.76;
stg2_success_n_m_vector_graph = stg2_success_n_m_vector(stg2_successful_run_index);
stg2_success_P_exit_vector_graph = stg2_success_P_e_vector(stg2_successful_run_index);
stg2_P_s0_vector_graph = stg2_P_s0_vector(stg2_successful_run_index)./6894.76;

%% PLOTTING DATA ALONG WITH CURVE FITS

[stg1_nm_fit,stg1_nm_gof] = createFit1(stg1_mdot_s_vector_graph,
stg1_success_n_m_vector_graph);
save('first_stage_fit.mat','stg1_nm_fit','stg1_nm_gof','stg1_mdot_s_vector_graph','stg1_success_
n_m_vector_graph');

[stg2_nm_fit,stg2_nm_gof] = createFit2(stg2_mdot_s_vector_graph,
stg2_success_n_m_vector_graph);
save('second_stage_fit.mat','stg2_nm_fit','stg2_nm_gof','stg2_mdot_s_vector_graph','stg2_succes
s_n_m_vector_graph');

figure(1)
hold on
```

```
yyaxis left
scatter(stg1_mdot_s_vector_graph,stg1_success_n_m_vector_graph, 'LineWidth', 2);
plot(stg1_nm_fit,stg1_mdot_s_vector_col,success_n_m_vector_col);
ylim([0 1]);
ylabel('Momentum Coefficient');
yyaxis right
plot(stg1_mdot_s_vector_graph,stg1_P_s0_vector_graph, 'LineWidth', 2);
ylim([0 15]);
ylabel('Suction Pressure (psia)');
xlabel('Suction Mass Flow Rate (kg/s)');
legend('Characterization Data','Suction Inlet Pressure');

figure(2)
hold on
yyaxis left
plot(stg2_mdot_s_vector_graph,stg2_success_n_m_vector_graph, 'LineWidth', 2);
ylim([0 1]);
ylabel('Momentum Coefficient');
yyaxis right
plot(stg2_mdot_s_vector_graph,stg2_P_s0_vector_graph, 'LineWidth', 2);
ylim([0 15]);
ylabel('Suction Pressure (psia)');
xlabel('Suction Mass Flow Rate (kg/s)');
legend('Characterization Data','Suction Inlet Pressure');

% figure(2)
%
stem3(stg1_P_p0_vector_graph./6894.7,stg1_mdot_s_vector_graph,success_P_exit_vector_grap
h./6894.7);
% title('Successful Exit Pressure for Various Motive Pressure/Suction Mass Flow
Combinations');
% xlabel('Motive Pressure');
% ylabel('Suction Mass Flow Rate (kg/s)');
% zlabel('Exit Pressure (psia)');
%
% figure(3)
%
stem3(stg1_P_p0_vector_graph./6894.7,stg1_P_s0_vector_graph./6894.7,success_n_m_vector_g
raph);
% title('Energy Efficiency Coefficient for Various Motive/Entrained Pressure Combinations');
% xlabel('Motive Pressure (psia)');
% ylabel('Suction Pressure (psia)');
% zlabel('Energy Efficiency Coefficient');
% zlim([0 1]);
%
% figure(4)
```

```
%
stem3(stg1_P_p0_vector_graph./6894.7,stg1_mdot_s_vector_graph,stg1_P_s0_vector_graph./68
94.7);
% title('Test Data Graph');
% xlabel('Motive Pressure (psia)');
% ylabel('Suction Mass Flow (kg/s)');
% zlabel('Suction Static Pressure (psia)');
% zlim([0 15]);
%
% figure(5)
% hold on
% stem3(stg1_mdot_s_vector_graph,stg1_P_ratio_vector_graph,success_n_m_vector_graph);
%
plot(fit_mdotein_pratio_success_n_m,[stg1_mdot_s_vector_col,stg1_P_ratio_vector_col],succes
s_n_m_vector_col);
% title('Test Data Graph');
% xlabel('Suction Mass Flow Rate (kg/s)');
% ylabel('Mixing Chamber Pressure Ratio');
% zlabel('Energy Efficiency Coefficient');
% zlim([0 1]);
%
% figure(6)
% scatter(stg1_P_p1_vector_graph./stg1_P_mc_vector_graph,success_n_m_vector_graph);
% title('Energy Efficiency Coefficient versus Mixing Chamber Pressure Ratio');
% xlabel('Mixing Chamber Pressure Ratio');
% ylabel('Energy Efficiency Coefficient');
%
% figure(7)
%
scatter(stg1_mdot_p_vector_graph./stg1_mdot_s_vector_graph,stg1_P_mc_vector_graph./6894.
7);
%
% figure(8)
% scatter(stg1_P_p0_vector_graph./6894.7,stg1_mdot_s_vector_graph);
%
% figure(9)
%
stem3(stg1_P_p0_vector_graph./6894.7,stg1_mdot_s_vector_graph,success_n_m_vector_graph)
;
% title('Energy Efficiency Coefficient for Various Motive Pressure/Suction Mass Flow
Combinations');
% xlabel('Motive Pressure (psia)');
% ylabel('Suction Mass Flow Rate (kg/s)');
% zlabel('Energy Efficiency Coefficient');
% zlim([0 1]);
```

TEST_DATA_ANALYSIS_TWO_STAGE_EJECTOR_90N.M:

```
% This script is used to load experimental rocket engine test data for the
% two-stage ejector with a 90 N engine.  The new 1-D model is then
% used to determine the momentum coefficient value that satisfies each
% of the experimentally defined data points.  The resulting momentum
% coefficient curve is then shown graphically.

%% DEFINING GAS CONSTANTS

% Coefficients Used for Heat Capacity Calaculation
a_ox = 28.186;
b_ox = 6.3011;
c_ox = -0.74986;
d_ox = 0;

a_n2 = 27.336;
b_n2 = 6.23;
c_n2 = -0.95082;
d_n2 = 0;

% Universal Gas Constant [J/(K*mol)]
R_u = 8.314;

%Typical isentropic efficiency for CD nozzle
stg1_n_p = 0.993;
%Typical isentropic efficiency for CD nozzle
stg2_n_p = 0.993;

% Initializing Momentum Coefficient Scanning Range
n_m_vector = 0.0001:0.0001:1;

%% DEFINING 1ST STAGE MOTIVE CONDITIONS

% Defining 1st Stage Geometrical Parameters

% Constant Section Diameter [m]
stg1_D_3 = 2.65*0.0254;
% Constant Section Area [m^2]
stg1_A_3 = (pi)/(4)*((stg1_D_3)^2);
% Motive Nozzle Throat Diameter [m]
stg1_D_t = 0.355*0.0254;
% Motive Nozzle Throat Area [m^2]
stg1_A_t = pi/4*((stg1_D_t)^2);
% Motive Nozzle Exit Diameter [m]
stg1_D_p1 = 0.5*0.0254;
% Motive NOzzle Exit Area [m^2]
```

```
stg1_A_p1 = pi/4*((stg1_D_p1)^2);
% Motive Nozzle Expansion Ratio
stg1_eps = stg1_A_p1/stg1_A_t;
% Contraction Section Diameter [m]
stg1_D_c = 6*0.0254;
% Contraction Section Area [m^2]
stg1_A_c = pi/4*((stg1_D_c)^2);

% Defining 1st Stage Motive Flow Values

% Motive Stagnation Pressure [Pa]
stg1_P_p0 = 500*6894.76;
% Motive Stagnation Temperature [K]
stg1_T_p0 = 298;
% Motive Heat Capacity Ratio
stg1_gamma_p = 1.4;
% Motive Molecular Weight [kg/mol]
stg1_MW_p = 0.029;
% Motive Heat Capacity [J/K]
stg1_Cp_p = (0.79*((a_n2)+(b_n2*(stg1_T_p0/1000))+...
    (c_n2*((stg1_T_p0/1000)^2))+(d_n2*((stg1_T_p0/1000)^3)))+...
    0.21*((a_ox)+(b_ox*(stg1_T_p0/1000))+(c_ox*((stg1_T_p0/1000)^2))+...
    (d_ox*((stg1_T_p0/1000)^3))))/(stg1_MW_p);
% Mach Number at Motive Nozzle Exit Plane
stg1_M_p1 = Mach_finder(stg1_eps,stg1_gamma_p,5);
% Motive Specific Gas Constant [J/(kg*K)]
stg1_R_p = R_u/stg1_MW_p; % J/(kg*K)
% Motive Mass Flow Rate [kg/s]
stg1_mdot_p = (stg1_P_p0)*(stg1_A_t)*...
    sqrt(((stg1_gamma_p/stg1_R_p)*((2/(stg1_gamma_p+1))^...
    ((stg1_gamma_p+1)/(stg1_gamma_p-1))))*(stg1_n_p)/(stg1_T_p0));

%% DEFINING 2ND STAGE MOTIVE CONDITIONS

% Defining 2nd Stage Geometrical Parameters

% Constant Section Diameter [m]
stg2_D_3 = 3*0.0254;
% Constant Section Area [m^2]
stg2_A_3 = (pi)/(4)*((stg2_D_3)^2);
% Motive Nozzle Throat Diameter [m]
stg2_D_t = 0.654*0.0254;
% Motive Nozzle Throat Area [m^2]
stg2_A_t = pi/4*((stg2_D_t)^2);
% Motive Nozzle Exit Diameter [m]
stg2_D_p1 = 1.25*0.0254;
```

```
% Motive NOzzle Exit Area [m^2]
stg2_A_p1 = pi/4*((stg2_D_p1)^2);
% Motive Nozzle Expansion Ratio
stg2_eps = stg2_A_p1/stg2_A_t;
% Contraction Section Diameter [m]
stg2_D_c = 6.5*0.0254;
% Contraction Section Area [m^2]
stg2_A_c = pi/4*((stg2_D_c)^2);

% Defining 2nd Stage Motive Flow Values

stg2_P_p0 = 500*6894.76;
% Motive Stagnation Temperature [K]
stg2_T_p0 = 298;
% Motive Heat Capacity Ratio
stg2_gamma_p = 1.4;
% Motive Molecular Weight [kg/mol]
stg2_MW_p = 0.029; % kg/mol
% Motive Heat Capacity [J/K]
stg2_Cp_p = (0.79*((a_n2)+(b_n2*(stg2_T_p0/1000))+...
    (c_n2*((stg2_T_p0/1000)^2))+(d_n2*((stg2_T_p0/1000)^3)))+...
    0.21*((a_ox)+(b_ox*(stg2_T_p0/1000))+(c_ox*((stg2_T_p0/1000)^2))+...
    (d_ox*((stg2_T_p0/1000)^3))))/(stg2_MW_p);
% Mach Number at Motive Nozzle Exit Plane
stg2_M_p1 = Mach_finder(stg2_eps,stg2_gamma_p,5);
% Motive Specific Gas Constant [J/(kg*K)]
stg2_R_p = R_u/stg2_MW_p;
% Motive Mass Flow Rate [kg/s]
stg2_mdot_p = (stg2_P_p0)*(stg2_A_t)*...
    sqrt(((stg2_gamma_p/stg2_R_p)*((2/(stg2_gamma_p+1))^...
    ((stg2_gamma_p+1)/(stg2_gamma_p-1))))*(stg2_n_p)/(stg2_T_p0));

%% DEFINING 1ST STAGE SUCTION CONDITIONS

% Suction Stagnation Temperature [K]
stg1_T_s0 = 298;
% Suction Molecular Weight [kg/mol]
stg1_MW_s = 0.028;
% Suction Heat Capacity Ratio
stg1_gamma_s = 1.4;
% Suction Heat Capacity [J/K]
stg1_Cp_s = ((a_n2)+...
    (b_n2*(stg1_T_s0/1000))+...
    (c_n2*((stg1_T_s0/1000)^2))+...
    (d_n2*((stg1_T_s0/1000)^3)))/...
    (stg1_MW_s);
```

```
% Suction Specific Gas Constant [J/(kg*K)]
stg1_R_s = R_u/stg1_MW_s;
% Suction Mass Flow Rate [kg/s]
stg1_mdot_s_vector = 0.048*(1000/298)*(0.028/0.022);
% Suction Stagnation Pressure [Pa]
stg1_P_s0_vector = 1.4*6894.75729;

%% DEFINING 2ND STAGE SUCTION CONDITIONS

% Suction Stagnation Temperature [K]
stg2_T_s0 = 298;
% Suction Molecular Weight [kg/mol]
stg2_MW_s = 0.028;
% Suction Heat Capacity Ratio
stg2_gamma_s = 1.4;
% Suction Heat Capacity [J/K]
stg2_Cp_s = ((a_n2)+...
    (b_n2*(stg2_T_s0/1000))+...
    (c_n2*((stg2_T_s0/1000)^2))+...
    (d_n2*((stg2_T_s0/1000)^3)))/...
    (stg2_MW_s);
% Suction Specific Gas Constant [J/(kg*K)]
stg2_R_s = R_u/stg2_MW_s;
% Suction Mass Flow Rate [kg/s]
stg2_mdot_s_vector = stg1_mdot_p+stg1_mdot_s_vector;
% Suction Stagnation Pressure [Pa]
stg2_P_s0_vector = 4.5*6894.75729;

%% RUNNING SCRIPT FOR 1ST STAGE

% Initializing vectors to store successful values
stg1_success_n_m_vector = [];
stg1_success_P_e_vector = [];
stg1_successful_run_index = [];

for j_2 = 1:length(stg1_mdot_s_vector)

    % Exit Pressure Initially Set to Arbitrarily High Value
    stg1_cs_P_e = 101325*50;

    % Loading in values corresponding to current experimental data point
    stg1_P_s0 = stg1_P_s0_vector(j_2);
    stg1_mdot_s = stg1_mdot_s_vector(j_2);
    stg1_P_e = stg2_P_s0_vector(j_2);

    % Scanning over range of possible momentum coefficient values
```

```
for j_1 = 1:length(n_m_vector)

   % Loading in current momentum coefficient value
   n_m = n_m_vector(j_1);

   % Loading all Relevant Input Values
   ei.A_t = stg1_A_t;
   ei.T_p0 = stg1_T_p0;
   ei.P_p0 = stg1_P_p0;
   ei.Cp_p = stg1_Cp_p;
   ei.MW_p = stg1_MW_p;
   ei.gamma_p = stg1_gamma_p;
   ei.mdot_s = stg1_mdot_s;
   ei.T_s0 = stg1_T_s0;
   ei.P_s0 = stg1_P_s0;
   ei.Cp_s = stg1_Cp_s;
   ei.MW_s = stg1_MW_s;
   ei.gamma_s = stg1_gamma_s;
   ei.n_p = stg1_n_p;
   ei.M_p1 = stg1_M_p1;
   ei.R_p = stg1_R_p;
   ei.R_s = stg1_R_s;
   ei.A_3 = stg1_A_3;
   ei.n_m = n_m;
   ei.A_p1 = stg1_A_p1;
   ei.A_c = stg1_A_c;

   % Running model
   eo = new_model(ei);

   % Exit pressure must be higher than ambient (14.7 psia) for a run
   % to be successful
   if eo.P_e < stg1_P_e
      eo.P_e = 0;
   end
   % Choosing momentum coefficient value which yields exit pressure
   % JUST above ambient pressure
   if eo.P_e ~= 0
      if eo.P_e < stg1_cs_P_e
         stg1_cs_n_m = n_m;
         stg1_cs_P_e = eo.P_e;
      end
   end
end

if stg1_cs_P_e < 101325*50
```

```
        stg1_success_n_m_vector(j_2) = stg1_cs_n_m;
        stg1_success_P_e_vector(j_2) = stg1_cs_P_e;
        stg1_successful_run_index = [stg1_successful_run_index, j_2];
    end
end

%% DEFINING ALL OUTPUT VALUES FOR 1ST STAGE

stg1_mdot_s_vector_graph = stg1_mdot_s_vector(stg1_successful_run_index);
stg1_P_p0_graph = ones(1,length(stg1_mdot_s_vector_graph)).*stg1_P_p0./6894.76;
stg1_success_n_m_vector_graph = stg1_success_n_m_vector(stg1_successful_run_index);
stg1_success_P_exit_vector_graph = stg1_success_P_e_vector(stg1_successful_run_index);
stg1_P_s0_vector_graph = stg1_P_s0_vector(stg1_successful_run_index);

%% RUNNING SCRIPT FOR 1ST STAGE

% Initializing vectors to store successful values
stg2_success_n_m_vector = [];
stg2_success_P_e_vector = [];
stg2_successful_run_index = [];

for j_2 = 1:length(stg2_mdot_s_vector)

    % Exit Pressure Initially Set to Arbitrarily High Value
    stg2_cs_P_e = 101325*50;

    % Loading in values corresponding to current experimental data point
    stg2_P_s0 = stg2_P_s0_vector(j_2);
    stg2_mdot_s = stg2_mdot_s_vector(j_2);

    % Scanning over range of possible momentum coefficient values
    for j_1 = 1:length(n_m_vector)

        % Loading in current momentum coefficient value
        n_m = n_m_vector(j_1);

        % Loading all Relevant Input Values
        ei.A_t = stg2_A_t;
        ei.T_p0 = stg2_T_p0;
        ei.P_p0 = stg2_P_p0;
        ei.Cp_p = stg2_Cp_p;
        ei.MW_p = stg2_MW_p;
        ei.gamma_p = stg2_gamma_p;
        ei.mdot_s = stg2_mdot_s;
        ei.T_s0 = stg2_T_s0;
        ei.P_s0 = stg2_P_s0;
```

```
        ei.Cp_s = stg2_Cp_s;
        ei.MW_s = stg2_MW_s;
        ei.gamma_s = stg2_gamma_s;
        ei.n_p = stg2_n_p;
        ei.M_p1 = stg2_M_p1;
        ei.R_p = stg2_R_p;
        ei.R_s = stg2_R_s;
        ei.A_3 = stg2_A_3;
        ei.n_m = n_m;
        ei.A_p1 = stg2_A_p1;
        ei.A_c = stg2_A_c;

        % Running model
        eo = new_model(ei);

        % Exit pressure must be higher than ambient (14.7 psia) for a run
        % to be successful
        if eo.P_e < 101325
            eo.P_e = 0;
        end
        % Choosing momentum coefficient value which yields exit pressure
        % JUST above ambient pressure
        if eo.P_e ~= 0
            if eo.P_e < stg2_cs_P_e
                stg2_cs_n_m = n_m;
                stg2_cs_P_e = eo.P_e;
            end
        end
    end

    if stg2_cs_P_e < 101325*50
        stg2_success_n_m_vector(j_2) = stg2_cs_n_m;
        stg2_success_P_e_vector(j_2) = stg2_cs_P_e;
        stg2_successful_run_index = [stg2_successful_run_index, j_2];
    end
end

%% DEFINING ALL OUTPUT VALUES FOR 1ST STAGE

stg2_mdot_s_vector_graph = stg2_mdot_s_vector(stg2_successful_run_index);
stg2_P_p0_graph = ones(1,length(stg2_mdot_s_vector_graph)).*stg2_P_p0./6894.76;
stg2_success_n_m_vector_graph = stg2_success_n_m_vector(stg2_successful_run_index);
stg2_success_P_exit_vector_graph = stg2_success_P_e_vector(stg2_successful_run_index);
stg2_P_s0_vector_graph = stg2_P_s0_vector(stg2_successful_run_index);

%% PLOTTING DATA ALONG WITH CURVE FITS
```

```
figure(1)
hold on
scatter(stg1_mdot_s_vector_graph,stg1_success_n_m_vector_graph, 'LineWidth', 2);
xlabel('Suction Mass Flow Rate (kg/s)');
ylabel('Momentum Coefficient');
ylim([0 1]);

figure(2)
hold on
scatter(stg2_mdot_s_vector_graph,stg2_success_n_m_vector_graph, 'LineWidth', 2);
xlabel('Suction Mass Flow Rate (kg/s)');
ylabel('Momentum Coefficient');
ylim([0 1]);

% figure(2)
%
stem3(stg1_P_p0_vector_graph./6894.7,stg1_mdot_s_vector_graph,success_P_exit_vector_grap
h./6894.7);
% title('Successful Exit Pressure for Various Motive Pressure/Suction Mass Flow
Combinations');
% xlabel('Motive Pressure');
% ylabel('Suction Mass Flow Rate (kg/s)');
% zlabel('Exit Pressure (psia)');
%
% figure(3)
%
stem3(stg1_P_p0_vector_graph./6894.7,stg1_P_s0_vector_graph./6894.7,success_n_m_vector_g
raph);
% title('Energy Efficiency Coefficient for Various Motive/Entrained Pressure Combinations');
% xlabel('Motive Pressure (psia)');
% ylabel('Suction Pressure (psia)');
% zlabel('Energy Efficiency Coefficient');
% zlim([0 1]);
%
% figure(4)
%
stem3(stg1_P_p0_vector_graph./6894.7,stg1_mdot_s_vector_graph,stg1_P_s0_vector_graph./68
94.7);
% title('Test Data Graph');
% xlabel('Motive Pressure (psia)');
% ylabel('Suction Mass Flow (kg/s)');
% zlabel('Suction Static Pressure (psia)');
% zlim([0 15]);
%
% figure(5)
```

```
% hold on
% stem3(stg1_mdot_s_vector_graph,stg1_P_ratio_vector_graph,success_n_m_vector_graph);
%
plot(fit_mdotein_pratio_success_n_m,[stg1_mdot_s_vector_col,stg1_P_ratio_vector_col],succes
s_n_m_vector_col);
% title('Test Data Graph');
% xlabel('Suction Mass Flow Rate (kg/s)');
% ylabel('Mixing Chamber Pressure Ratio');
% zlabel('Energy Efficiency Coefficient');
% zlim([0 1]);
%
% figure(6)
% scatter(stg1_P_p1_vector_graph./stg1_P_mc_vector_graph,success_n_m_vector_graph);
% title('Energy Efficiency Coefficient versus Mixing Chamber Pressure Ratio');
% xlabel('Mixing Chamber Pressure Ratio');
% ylabel('Energy Efficiency Coefficient');
%
% figure(7)
%
scatter(stg1_mdot_p_vector_graph./stg1_mdot_s_vector_graph,stg1_P_mc_vector_graph./6894.
7);
%
% figure(8)
% scatter(stg1_P_p0_vector_graph./6894.7,stg1_mdot_s_vector_graph);
%
% figure(9)
%
stem3(stg1_P_p0_vector_graph./6894.7,stg1_mdot_s_vector_graph,success_n_m_vector_graph)
;
% title('Energy Efficiency Coefficient for Various Motive Pressure/Suction Mass Flow
Combinations');
% xlabel('Motive Pressure (psia)');
% ylabel('Suction Mass Flow Rate (kg/s)');
% zlabel('Energy Efficiency Coefficient');
% zlim([0 1]);
```

APPENDIX B. MACHINE DRAWINGS

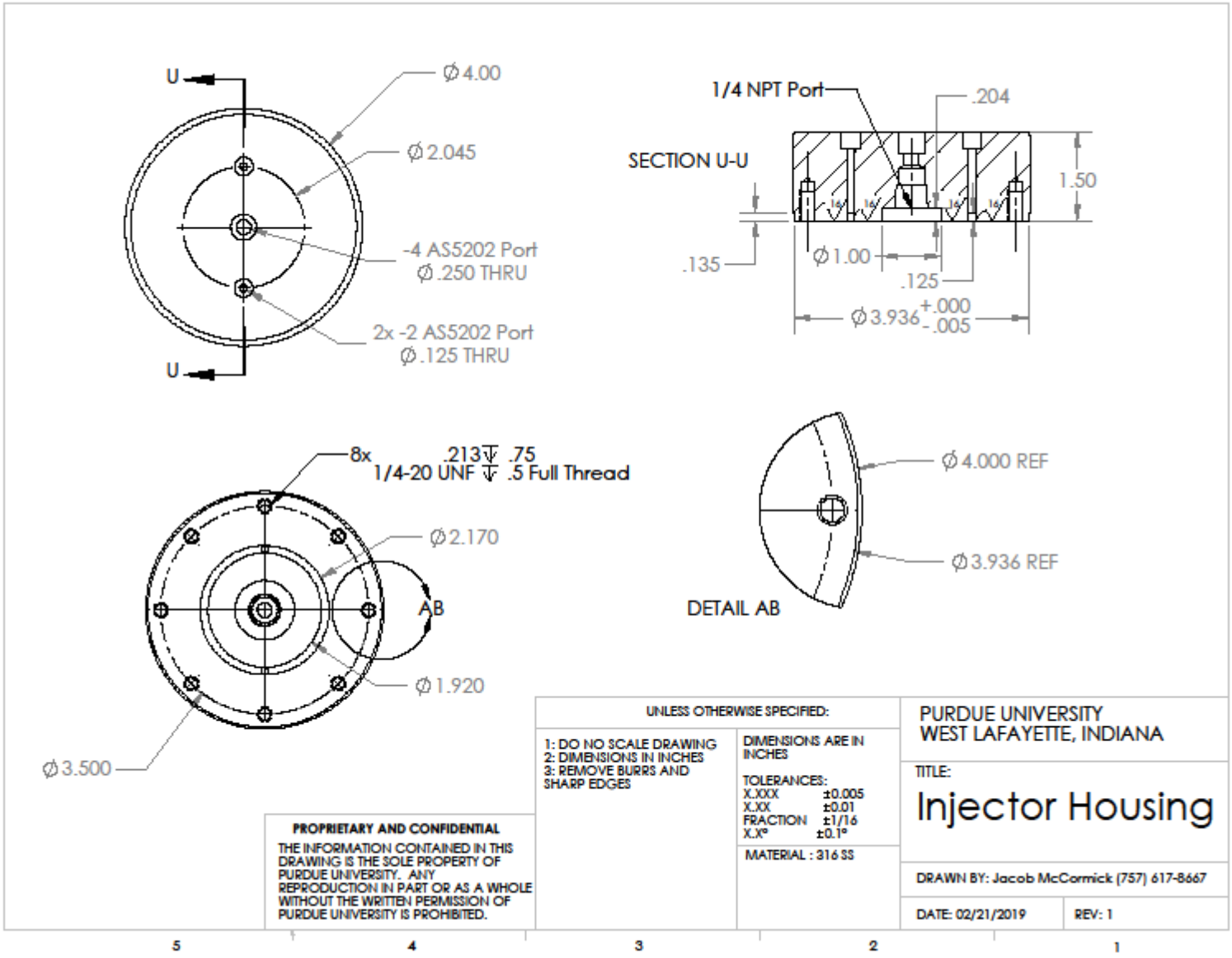
U
U
Ø4.00
Ø2.045
-4 AS5202 Port
Ø.250 THRU
2x -2 AS5202 Port
Ø.125 THRU
1/4 NPT Port
.204
SECTION U-U
1.50
.135
Ø1.00
.125
Ø3.936 +.000 -.005
8x .213 ↧ .75
1/4-20 UNF ↧ .5 Full Thread
Ø2.170
AB
Ø1.920
Ø3.500
Ø4.000 REF
Ø3.936 REF
DETAIL AB
UNLESS OTHERWISE SPECIFIED:
1: DO NO SCALE DRAWING
2: DIMENSIONS IN INCHES
3: REMOVE BURRS AND SHARP EDGES
DIMENSIONS ARE IN INCHES
TOLERANCES:
X.XXX ±0.005
X.XX ±0.01
FRACTION ±1/16
X.X° ±0.1°
MATERIAL : 316 SS
PROPRIETARY AND CONFIDENTIAL
THE INFORMATION CONTAINED IN THIS DRAWING IS THE SOLE PROPERTY OF PURDUE UNIVERSITY. ANY REPRODUCTION IN PART OR AS A WHOLE WITHOUT THE WRITTEN PERMISSION OF PURDUE UNIVERSITY IS PROHIBITED.
PURDUE UNIVERSITY
WEST LAFAYETTE, INDIANA
TITLE:
Injector Housing
DRAWN BY: Jacob McCormick (757) 617-8667
DATE: 02/21/2019
REV: 1
5
4
3
2
1

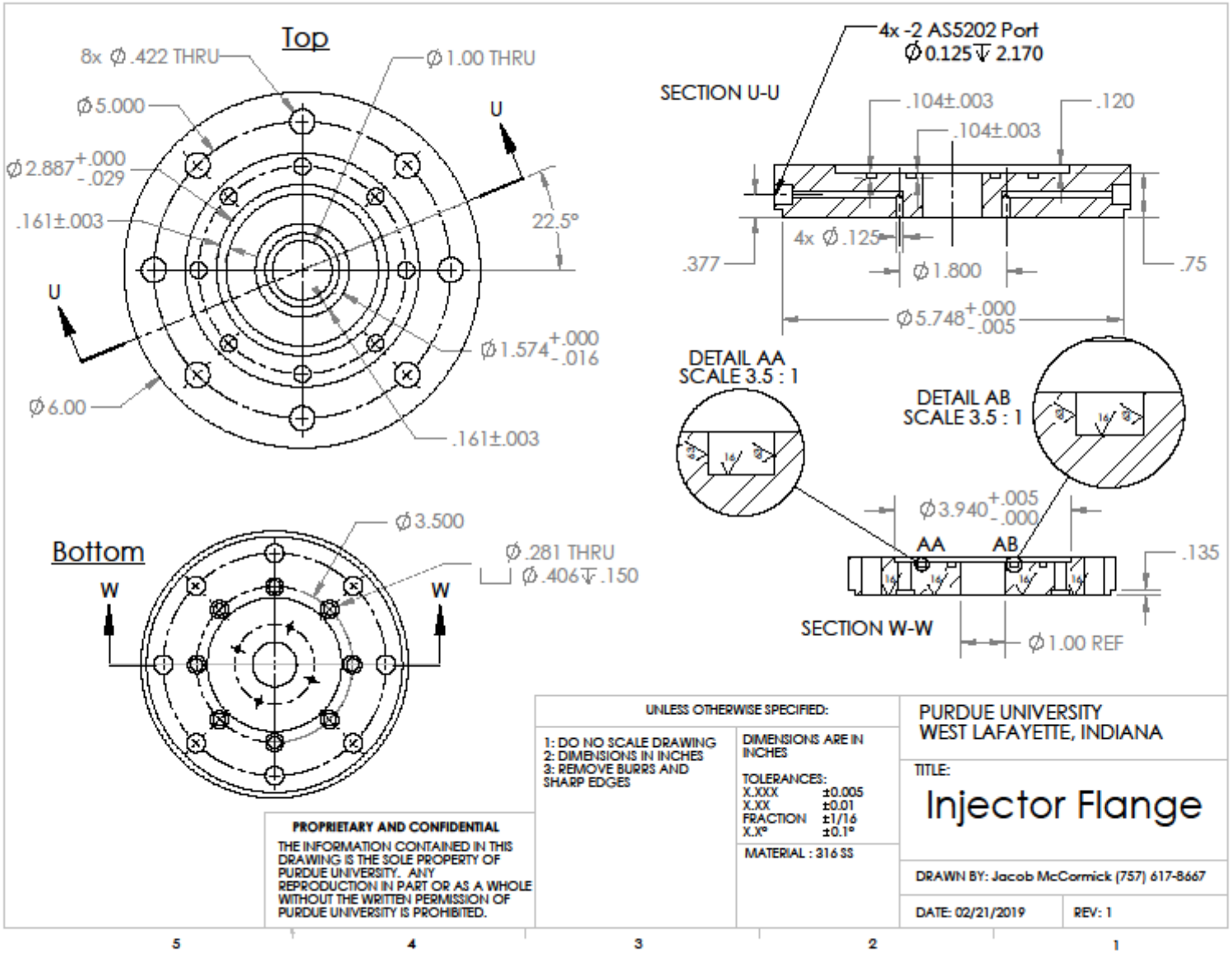
Top
8x Ø.422 THRU
Ø1.00 THRU
Ø5.000
Ø2.887 +.000 -.029
.161±.003
22.5°
U
U
Ø1.574 +.000 -.016
Ø6.00
.161±.003
4x -2 AS5202 Port
Ø0.125↧2.170
SECTION U-U
.104±.003
.104±.003
.120
4x Ø.125
.377
Ø1.800
.75
Ø5.748 +.000 -.005
DETAIL AA
SCALE 3.5 : 1
DETAIL AB
SCALE 3.5 : 1
Ø3.940 +.005 -.000
AA
AB
.135
SECTION W-W
Ø1.00 REF
Bottom
Ø3.500
Ø.281 THRU
Ø.406↧.150
W
W
PROPRIETARY AND CONFIDENTIAL
THE INFORMATION CONTAINED IN THIS DRAWING IS THE SOLE PROPERTY OF PURDUE UNIVERSITY. ANY REPRODUCTION IN PART OR AS A WHOLE WITHOUT THE WRITTEN PERMISSION OF PURDUE UNIVERSITY IS PROHIBITED.
UNLESS OTHERWISE SPECIFIED:
1: DO NO SCALE DRAWING
2: DIMENSIONS IN INCHES
3: REMOVE BURRS AND SHARP EDGES
DIMENSIONS ARE IN INCHES
TOLERANCES:
X.XXX ±0.005
X.XX ±0.01
FRACTION ±1/16
X.X° ±0.1°
MATERIAL : 316 SS
PURDUE UNIVERSITY
WEST LAFAYETTE, INDIANA
TITLE:
Injector Flange
DRAWN BY: Jacob McCormick (757) 617-8667
DATE: 02/21/2019
REV: 1
5
4
3
2
1

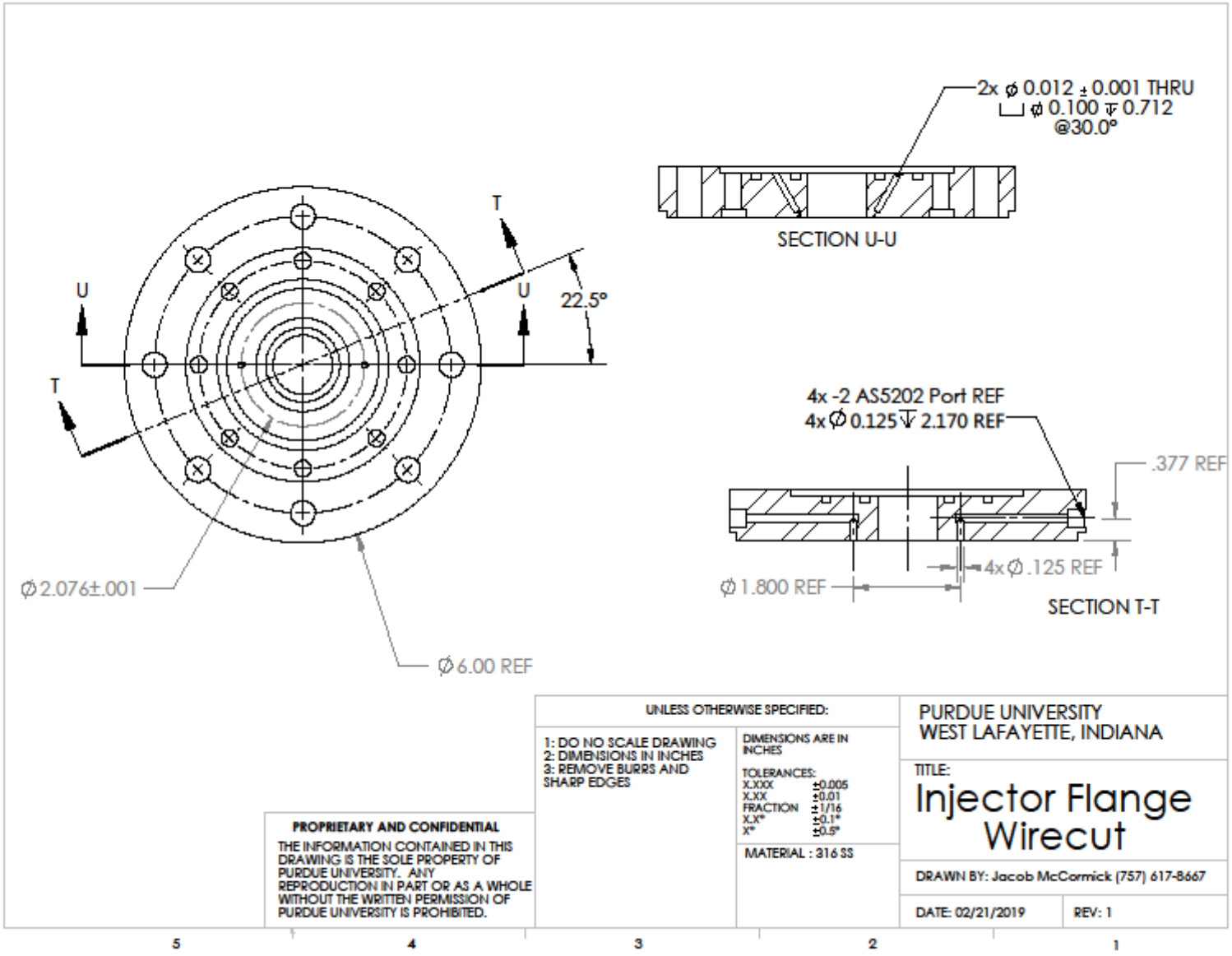
2x ⌀ 0.012 ± 0.001 THRU
⌴ ⌀ 0.100 ↧ 0.712
@30.0°
SECTION U-U
T
U
U
22.5°
T
⌀2.076±.001
⌀6.00 REF
4x -2 AS5202 Port REF
4x⌀ 0.125↧ 2.170 REF
.377 REF
4x⌀ .125 REF
⌀ 1.800 REF
SECTION T-T
UNLESS OTHERWISE SPECIFIED:
1: DO NO SCALE DRAWING
2: DIMENSIONS IN INCHES
3: REMOVE BURRS AND SHARP EDGES
DIMENSIONS ARE IN INCHES
TOLERANCES:
X.XXX ±0.005
X.XX ±0.01
FRACTION ±1/16
X.X° ±0.1°
X° ±0.5°
MATERIAL : 316 SS
PROPRIETARY AND CONFIDENTIAL
THE INFORMATION CONTAINED IN THIS DRAWING IS THE SOLE PROPERTY OF PURDUE UNIVERSITY. ANY REPRODUCTION IN PART OR AS A WHOLE WITHOUT THE WRITTEN PERMISSION OF PURDUE UNIVERSITY IS PROHIBITED.
PURDUE UNIVERSITY
WEST LAFAYETTE, INDIANA
TITLE:
Injector Flange Wirecut
DRAWN BY: Jacob McCormick (757) 617-8667
DATE: 02/21/2019
REV: 1
5
4
3
2
1

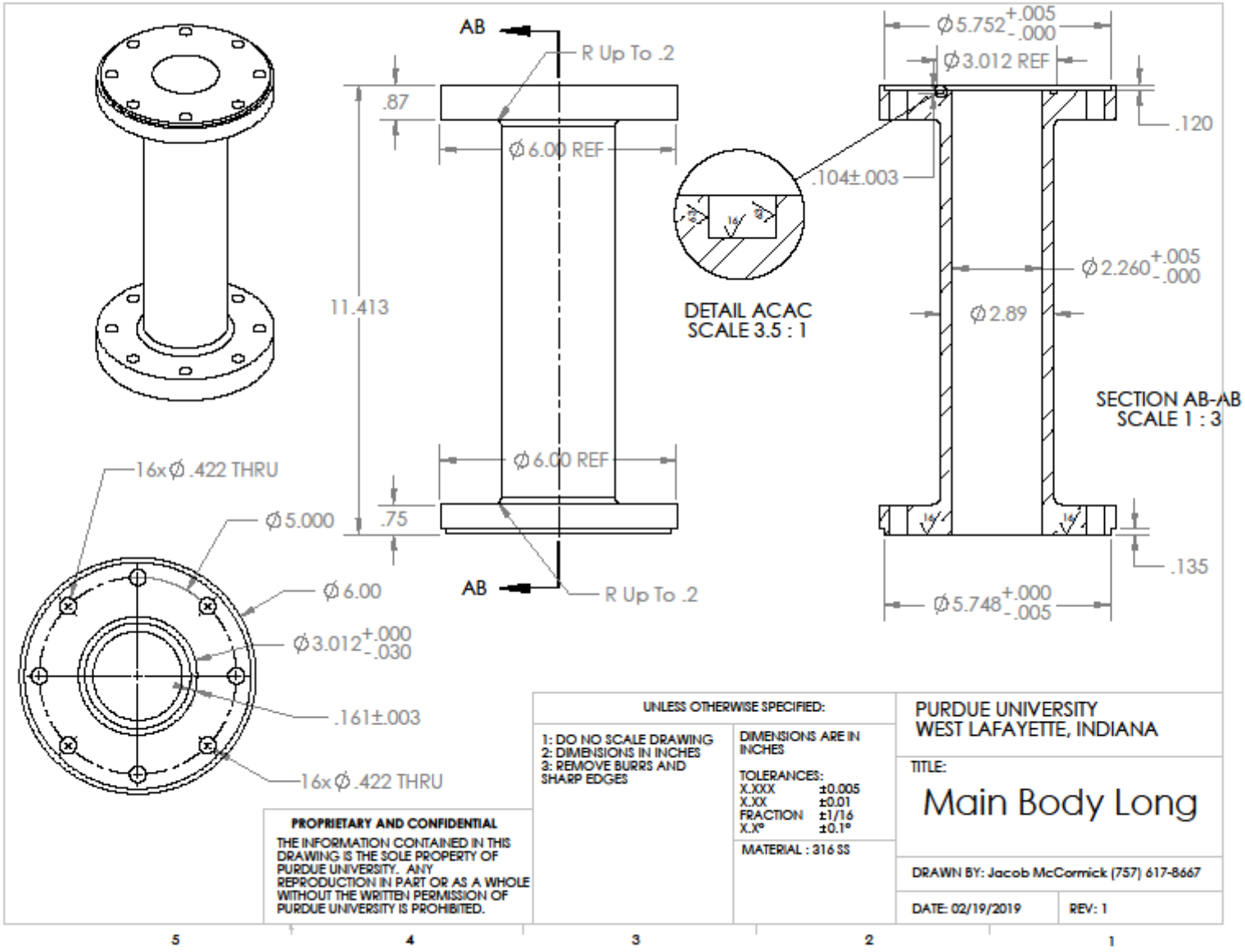
AB
R Up To .2
.87
Ø6.00 REF
11.413
Ø6.00 REF
.75
AB
R Up To .2
16xØ.422 THRU
Ø5.000
Ø6.00
Ø3.012 +.000 -.030
.161±.003
16xØ.422 THRU
Ø5.752 +.005 -.000
Ø3.012 REF
.120
.104±.003
Ø2.260 +.005 -.000
Ø2.89
.135
Ø5.748 +.000 -.005
DETAIL ACAC
SCALE 3.5 : 1
SECTION AB-AB
SCALE 1 : 3
UNLESS OTHERWISE SPECIFIED:
1: DO NO SCALE DRAWING
2: DIMENSIONS IN INCHES
3: REMOVE BURRS AND SHARP EDGES
DIMENSIONS ARE IN INCHES
TOLERANCES:
X.XXX ±0.005
X.XX ±0.01
FRACTION ±1/16
X.X° ±0.1°
MATERIAL : 316 SS
PROPRIETARY AND CONFIDENTIAL
THE INFORMATION CONTAINED IN THIS DRAWING IS THE SOLE PROPERTY OF PURDUE UNIVERSITY. ANY REPRODUCTION IN PART OR AS A WHOLE WITHOUT THE WRITTEN PERMISSION OF PURDUE UNIVERSITY IS PROHIBITED.
PURDUE UNIVERSITY
WEST LAFAYETTE, INDIANA
TITLE:
Main Body Long
DRAWN BY: Jacob McCormick (757) 617-8667
DATE: 02/19/2019
REV: 1
5
4
3
2
1

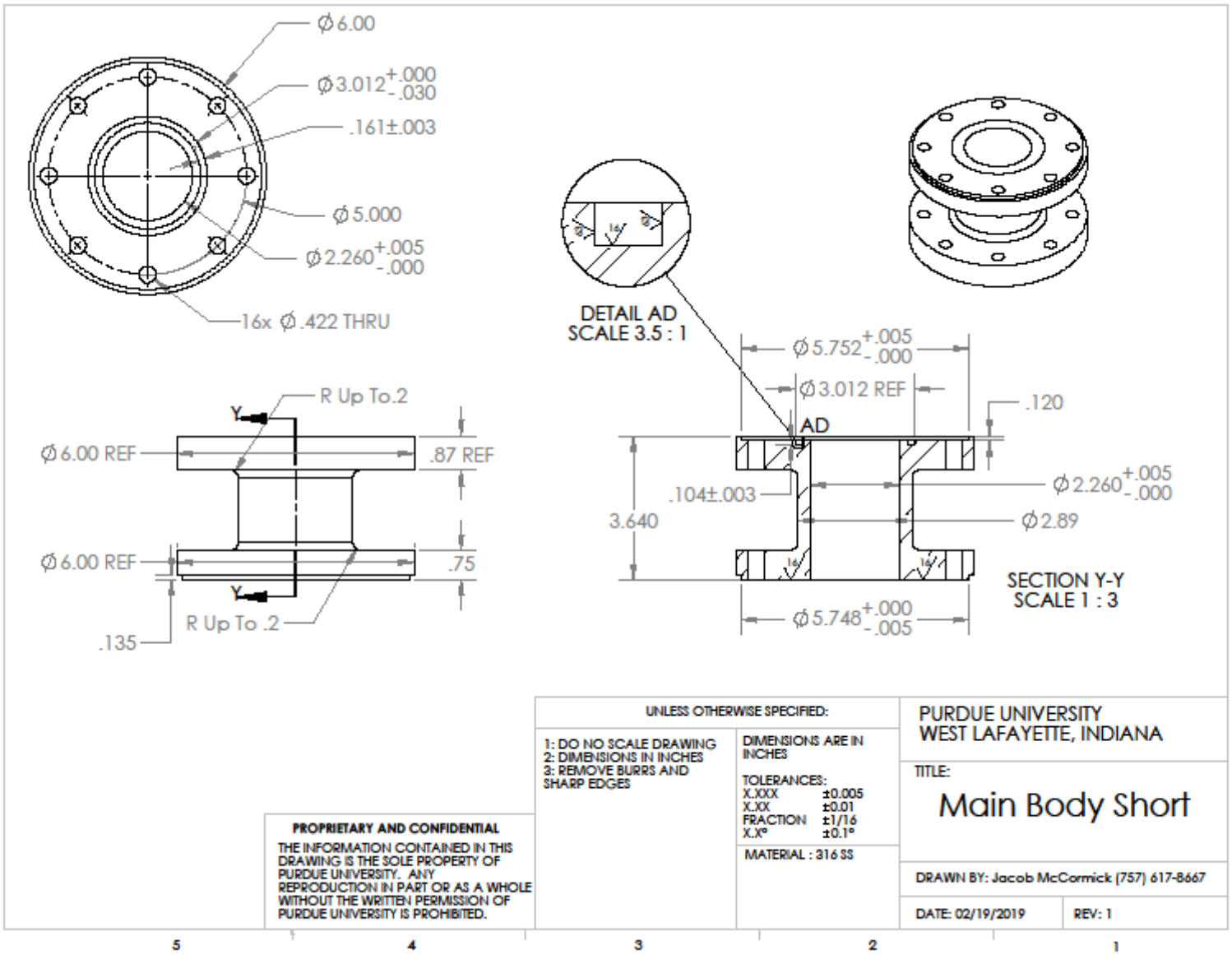
Ø6.00
Ø3.012 +.000 -.030
.161±.003
Ø5.000
Ø2.260 +.005 -.000
16x Ø.422 THRU
R Up To.2
Ø6.00 REF
.87 REF
Ø6.00 REF
.75
R Up To .2
.135
DETAIL AD
SCALE 3.5 : 1
Ø5.752 +.005 -.000
Ø3.012 REF
.120
AD
.104±.003
3.640
Ø2.260 +.005 -.000
Ø2.89
Ø5.748 +.000 -.005
SECTION Y-Y
SCALE 1 : 3
UNLESS OTHERWISE SPECIFIED:
1: DO NO SCALE DRAWING
2: DIMENSIONS IN INCHES
3: REMOVE BURRS AND SHARP EDGES
DIMENSIONS ARE IN INCHES
TOLERANCES:
X.XXX ±0.005
X.XX ±0.01
FRACTION ±1/16
X.X° ±0.1°
MATERIAL : 316 SS
PROPRIETARY AND CONFIDENTIAL
THE INFORMATION CONTAINED IN THIS DRAWING IS THE SOLE PROPERTY OF PURDUE UNIVERSITY. ANY REPRODUCTION IN PART OR AS A WHOLE WITHOUT THE WRITTEN PERMISSION OF PURDUE UNIVERSITY IS PROHIBITED.
PURDUE UNIVERSITY
WEST LAFAYETTE, INDIANA
TITLE:
Main Body Short
DRAWN BY: Jacob McCormick (757) 617-8667
DATE: 02/19/2019
REV: 1
5
4
3
2
1

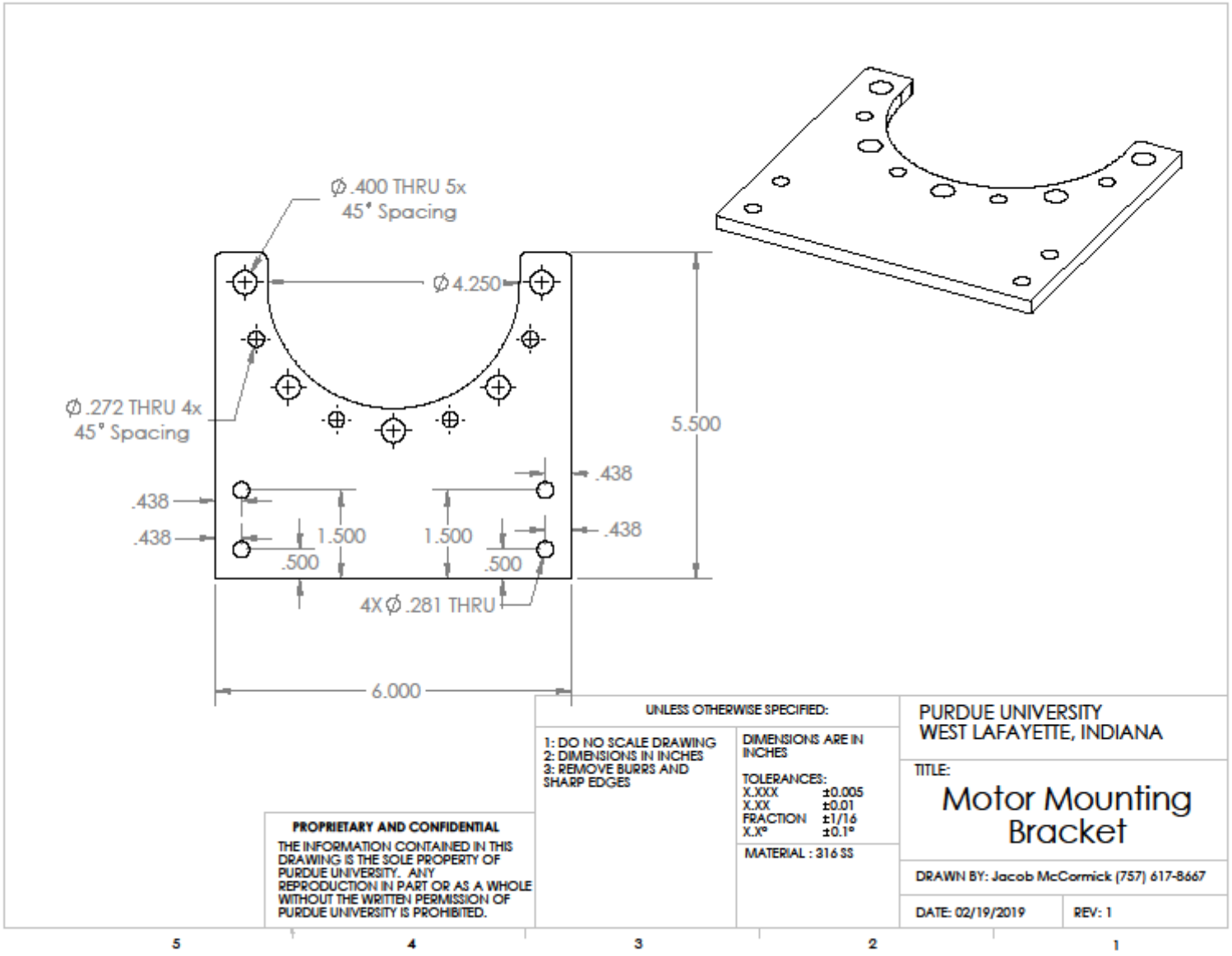
Ø.400 THRU 5x
45° Spacing
Ø4.250
Ø.272 THRU 4x
45° Spacing
5.500
.438
.438
.438
.438
1.500
1.500
.500
.500
4XØ.281 THRU
6.000
UNLESS OTHERWISE SPECIFIED:
1: DO NO SCALE DRAWING
2: DIMENSIONS IN INCHES
3: REMOVE BURRS AND SHARP EDGES
DIMENSIONS ARE IN INCHES
TOLERANCES:
X.XXX ±0.005
X.XX ±0.01
FRACTION ±1/16
X.X° ±0.1°
MATERIAL : 316 SS
PROPRIETARY AND CONFIDENTIAL
THE INFORMATION CONTAINED IN THIS DRAWING IS THE SOLE PROPERTY OF PURDUE UNIVERSITY. ANY REPRODUCTION IN PART OR AS A WHOLE WITHOUT THE WRITTEN PERMISSION OF PURDUE UNIVERSITY IS PROHIBITED.
PURDUE UNIVERSITY
WEST LAFAYETTE, INDIANA
TITLE:
Motor Mounting Bracket
DRAWN BY: Jacob McCormick (757) 617-8667
DATE: 02/19/2019
REV: 1
5
4
3
2
1

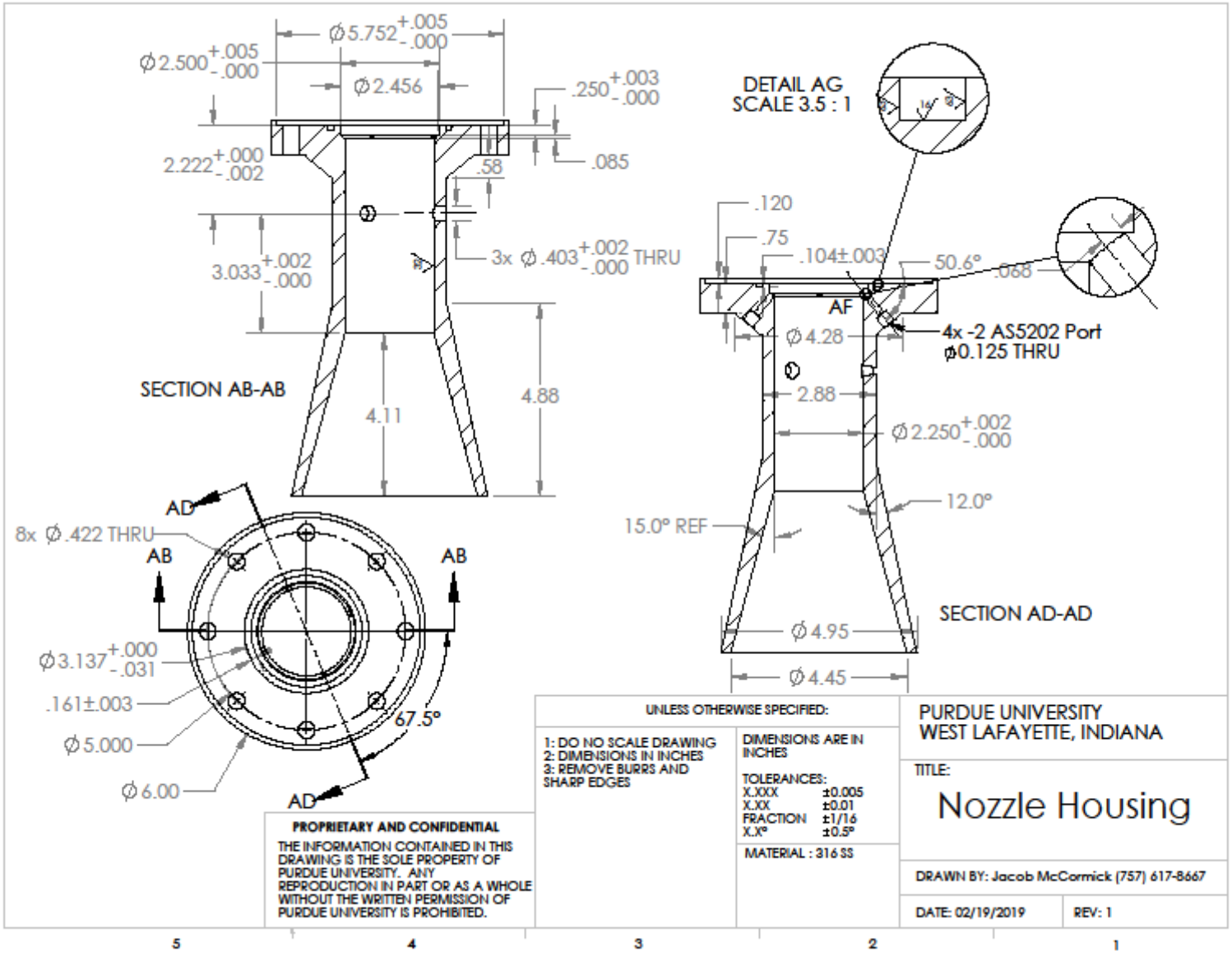
Ø5.752 +.005 -.000
Ø2.500 +.005 -.000
Ø2.456
.250 +.003 -.000
2.222 +.000 -.002
.58
.085
3.033 +.002 -.000
3x Ø.403 +.002 -.000 THRU
SECTION AB-AB
4.11
4.88
AD
8x Ø.422 THRU
AB
AB
Ø3.137 +.000 -.031
.161±.003
Ø5.000
Ø6.00
67.5°
AD
DETAIL AG
SCALE 3.5 : 1
.120
.75
.104±.003
50.6°
.068
AF
Ø4.28
4x -2 AS5202 Port
ø0.125 THRU
2.88
Ø2.250 +.002 -.000
12.0°
15.0° REF
SECTION AD-AD
Ø4.95
Ø4.45
UNLESS OTHERWISE SPECIFIED:
1: DO NO SCALE DRAWING
2: DIMENSIONS IN INCHES
3: REMOVE BURRS AND SHARP EDGES
DIMENSIONS ARE IN INCHES
TOLERANCES:
X.XXX ±0.005
X.XX ±0.01
FRACTION ±1/16
X.X° ±0.5°
MATERIAL : 316 SS
PROPRIETARY AND CONFIDENTIAL
THE INFORMATION CONTAINED IN THIS DRAWING IS THE SOLE PROPERTY OF PURDUE UNIVERSITY. ANY REPRODUCTION IN PART OR AS A WHOLE WITHOUT THE WRITTEN PERMISSION OF PURDUE UNIVERSITY IS PROHIBITED.
PURDUE UNIVERSITY
WEST LAFAYETTE, INDIANA
TITLE:
Nozzle Housing
DRAWN BY: Jacob McCormick (757) 617-8667
DATE: 02/19/2019
REV: 1
5
4
3
2
1

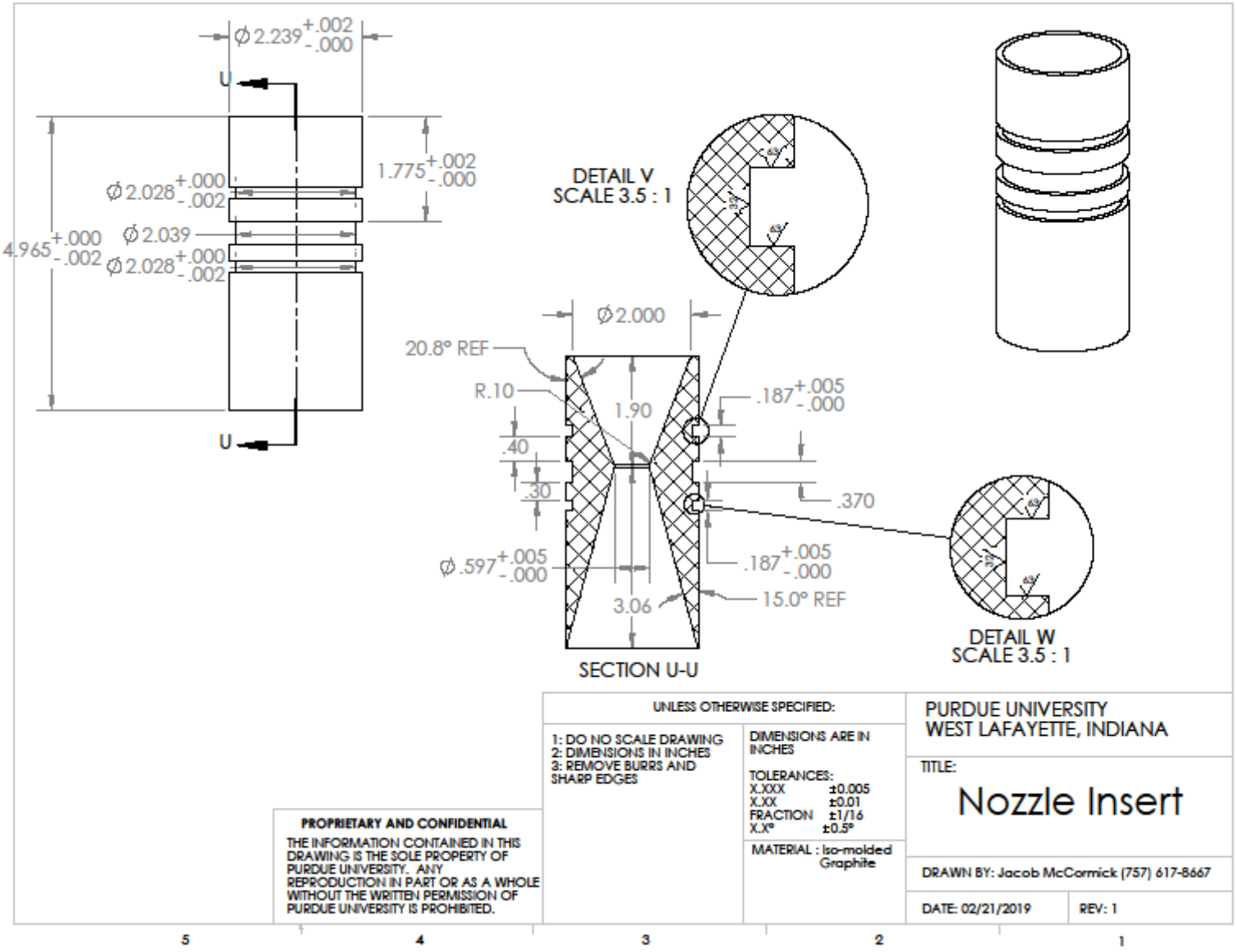
Ø2.239 +.002 -.000
U
1.775 +.002 -.000
Ø2.028 +.000 -.002
4.965 +.000 -.002
Ø2.039
Ø2.028 +.000 -.002
U
DETAIL V
SCALE 3.5 : 1
Ø2.000
20.8° REF
R.10
1.90
.187 +.005 -.000
.40
.30
.370
Ø.597 +.005 -.000
.187 +.005 -.000
3.06
15.0° REF
SECTION U-U
DETAIL W
SCALE 3.5 : 1
UNLESS OTHERWISE SPECIFIED:
1: DO NO SCALE DRAWING
2: DIMENSIONS IN INCHES
3: REMOVE BURRS AND SHARP EDGES
DIMENSIONS ARE IN INCHES
TOLERANCES:
X.XXX ±0.005
X.XX ±0.01
FRACTION ±1/16
X.X° ±0.5°
MATERIAL : Iso-molded Graphite
PROPRIETARY AND CONFIDENTIAL
THE INFORMATION CONTAINED IN THIS DRAWING IS THE SOLE PROPERTY OF PURDUE UNIVERSITY. ANY REPRODUCTION IN PART OR AS A WHOLE WITHOUT THE WRITTEN PERMISSION OF PURDUE UNIVERSITY IS PROHIBITED.
PURDUE UNIVERSITY
WEST LAFAYETTE, INDIANA
TITLE:
Nozzle Insert
DRAWN BY: Jacob McCormick (757) 617-8667
DATE: 02/21/2019
REV: 1
5
4
3
2
1